

AD-A056 782

TEXAS TECH UNIV LUBBOCK OPTICAL SCIENCES LAB
ELLIPSOMETRIC DETERMINATION OF PROPERTIES OF FILMS ON ROUGH SUR--ETC(U)
AUG 77 J D REICHERT, J S BROCK

F/G 14/2

UNCLASSIFIED

TTCSL-OLT-3

AFOSR-TR-78-1220

NL

1 OF 2
AD
A056782



AFOSR-TR- 78-1220

LEVEL II

①
SC

ELLIPSOMETRIC DETERMINATION
OF PROPERTIES OF FILMS ON ROUGH SURFACES
SUCH AS

ALUMINUM ALLOY AIRCRAFT SKIN

by

Dr. John D. Reichert

and

Janet Shotton Brock, M.S.E.E.

AD A 056782

AD No. ~~1~~
DDC FILE COPY

A Report to the
United States Air Force
on Work Performed Under
Grant #AFOSR-73-2451G

and

Grant #AFOSR 77-3278

DDC
RECEIVED
JUL 27 1978
E

Submitted by
John D. Reichert
Optics Sciences Laboratory
Department of Electrical Engineering
Texas Tech University
Lubbock, Texas 79409

August 1, 1977

Texas Tech University
Optical Sciences Laboratory
Report Number:
TTOSL-OLT-3

John D. Reichert
Dr. John D. Reichert
Principal Investigator

Approved for public release;
distribution unlimited.

78 07 26 045

①

AFOSR-TR-78-1220

ELLIPSOIDAL DETERMINATION

OF PROPERTIES OF FILMS FOR KODAK SAFETY FILMS

SUCH AS

ALUMINUM ALLOY AIRCRAFT SKIN
ALUMINUM ALLOY AIRCRAFT SKIN

Dr. John D. Roberts

James Griffin Brock, M.S.E.

287020A GA

DDC
JUL 27 1978
E

A Report to the
United States Air Force
on Work Performed Under
Grant FA-32-73-2416

Grant FA-32-73-2416

Department of Electrical Engineering
Texas Tech University
Lubbock, Texas 79409

June 1, 1977

DDC LIFE COPY
ON OA

Texas Tech University
Electrical Engineering Department
Lubbock, Texas 79409
Report Number
AFOSR-TR-78-1220

AIR FORCE OFFICE OF SCIENTIFIC RESEARCH (AFOSR)
NOTICE OF TRANSMITTAL TO DDC
This technical report has been reviewed and is
approved for public release IAW AFM 190-12 (7b).
Distribution is unlimited.
A. D. BLOSE
Technical Information Officer

UNCLASSIFIED

SECURITY CLASSIFICATION OF THIS PAGE (When Data Entered)

19 REPORT DOCUMENTATION PAGE		READ INSTRUCTIONS BEFORE COMPLETING FORM	
1. REPORT NUMBER AFOSR-TR- 78-1229	2. GOVT ACCESSION NO.	3. RECIPIENT'S CATALOG NUMBER	
4. TITLE (and Subtitle) Ellipsometric Determination of Properties of Films on Rough Surfaces Such as Aluminum Alloy Aircraft Skin		5. TYPE OF REPORT & PERIOD COVERED Interim report 1 Jan. 1976 to Aug. 1977	
6. AUTHOR(s) John D. Reichert Janet Shotton/Brock		7. PERFORMING ORG. REPORT NUMBER TTCSL-OLT-3V	
9. PERFORMING ORGANIZATION NAME AND ADDRESS Department of Electrical Engineering Texas Tech University Lubbock, Texas 79409		8. CONTRACT OR GRANT NUMBER(s) AFOSR-77-32789 AFOSR-73-24826	
11. CONTROLLING OFFICE NAME AND ADDRESS AFOSR/NP Bolling Air Force Base Washington, D.C. 20332		10. PROGRAM ELEMENT, PROJECT, TASK - AREA & WORK UNIT NUMBERS 2301/A1 61102F	
14. MONITORING AGENCY NAME & ADDRESS (if different from Controlling Office)		12. REPORT DATE 1 Aug 1977	
		13. NUMBER OF PAGES 137 (12) 140 P.	
		15. SECURITY CLASS. (of this report) UNCLASSIFIED	
		15a. DECLASSIFICATION/DOWNGRADING SCHEDULE	
16. DISTRIBUTION STATEMENT (of this Report) Approved for public release; distribution unlimited.			
17. DISTRIBUTION STATEMENT (of the abstract entered in Block 20, if different from Report)			
18. SUPPLEMENTARY NOTES			
19. KEY WORDS (Continue on reverse side if necessary and identify by block number) Oxide Layer Thickness, Ellipsometry of Rough Surfaces, ALCLAD Surface Oxide Layers, Oxide Layers on Pure Aluminum, Ellipsometry Theory			
20. ABSTRACT (Continue on reverse side if necessary and identify by block number) The properties of oxide layers on smooth and rough aluminum surfaces are considered in this study. Using ellipsometric techniques, the layer thickness and the four parameters describ- ing the complex indices of refraction for film and substrate are assigned effective values and interrelations are deduced. The organizing feature of the work is the use of data trajectories generated by determining the ellipsometric parameters ψ and Δ → next page			

DD FORM 1 JAN 73 1473 EDITION OF 1 NOV 65 IS OBSOLETE

UNCLASSIFIED

SECURITY CLASSIFICATION OF THIS PAGE (When Data Entered)

UNCLASSIFIED

SECURITY CLASSIFICATION OF THIS PAGE (When Data Entered)

over and over for samples that were heated between measurements. The heating caused increases in the oxide layer thickness, so that the data trajectories could be used along side theoretical thickness curves to determine appropriate effective media parameters. One of the more interesting results was the representation of rolling grain marks on alclad by an effective complex index of refraction. The effective index determined was dependent on the sample orientation.

UNCLASSIFIED

SECURITY CLASSIFICATION OF THIS PAGE (When Data Entered)

TABLE OF CONTENTS

ABSTRACT.	ii
LIST OF TABLES.	iii
LIST OF FIGURES	iv
I. INTRODUCTION.	1
II. THEORETICAL BASIS OF ELLIPSOMETRY	4
III. THE MECHANICS OF ELLIPSOMETRY	25
IV. AN ERROR ANALYSIS AND SENSITIVITY STUDY FOR ELLIPSOMETRIC PARAMETERS.	36
V. A STUDY OF OXIDE FILMS ON PURE ALUMINUM	65
VI. A STUDY OF OXIDE FILMS ON ALCLAD ALLOY.	107
LIST OF REFERENCES.	128
BIBLIOGRAPHY.	129

ACCESSION for	
NTS	White Section <input checked="" type="checkbox"/>
DOC	Buff Section <input type="checkbox"/>
UNANNOUNCED	<input type="checkbox"/>
JUSTIFICATION.....	
BY.....	
DISTRIBUTION/AVAILABILITY CODES	
Dist.	AVAIL. and/or SPECIAL
A	

78 07 26 045

ABSTRACT

The properties of oxide layers on smooth and rough aluminum surfaces are considered in this study. Using ellipsometric techniques, the layer thickness and the four parameters describing the complex indices of refraction for film and substrate are assigned effective values and interrelations are deduced. The organizing feature of the work is the use of data trajectories generated by determining the ellipsometric parameters ψ and Δ over and over for samples that were heated between measurements. The heating caused increases in the oxide layer thickness, so that the data trajectories could be used along side theoretical thickness curves to determine appropriate effective media parameters. One of the more interesting results was the representation of rolling grain marks on alclad by an effective complex index of refraction. The effective index determined was dependent on the sample orientation.

LIST OF TABLES

Table		Page
4.1	EFFECTS OF ALIGNMENT ERRORS FROM THE WAVE PLATE ANGLE ON ψ	44
4.2	EFFECTS OF ALIGNMENT ERRORS ON ψ DUE TO WAVE PLATE DELAY.	45
4.3	EFFECTS OF ALIGNMENT ERRORS ON Δ FROM THE WAVE PLATE ANGLE.	46
4.4	EFFECTS OF ALIGNMENT ERRORS ON Δ DUE TO WAVE PLATE DELAY.	47
5.1	RELATIONSHIP OF HEATING TEMPERATURE AND TIME AS RELATED TO THE BARRIER VOLTAGE	67
5.2	VALUES OF ψ AND Δ FOR THE FIVE SPOTS ON SAMPLE A . . .	69
5.3	SENSITIVITY OF THICKNESS TO Δ AND ψ	102
5.4	SENSITIVITY OF Δ TO K_s , n_s AND K_f	103
5.5	SENSITIVITY OF ψ TO K_s , n_s AND K_f	104
5.6	SENSITIVITY OF THICKNESS TO θ_i	105

LIST OF FIGURES

Figure		Page
2.1	The Bending of Light at the Interface of Two Media . .	7
2.2	Ray Plane Showing Incident, Reflected, and Transmitted Rays	9
2.3	Reflection of Light from Two Boundaries (Substrate with Film)	21
3.1	Schematic Representation of the Ellipsometer with Sample Inserted.	26
3.2	Schematic Representation of the Ellipsometer with no Sample for Reflection.	27
3.3	Relationship of R_s and R_p to the Angle A	33
4.1	Calibration Curves for the Polarizers.	39
4.2	The Two Pieces of the Compensator Showing a) the Direction of Movement for Adjustment of Thickness b) the Alignment Error in the Axis	41
4.3	Sensitivity Curve for Error in θ_i	50
4.4	The Two Configurations for Alignment of the Sample in the Ellipsometer Showing the Maximum Error Possible.	52
4.5	Curves of Constant n_s and Curves of Constant K_s for Bare Substrates.	55
4.6	A Thickness Curve: Variation in Δ and ψ Due to Changes in Film Thickness.	56
4.7	Variation in Thickness Curves as n_f Varies from 1.1 to 1.6	57
4.8	Variation in Thickness Curves as K_s Increases from 0.0 to 5.72.	59
4.9	Variation in Thickness Curve as n_f Varies from 1.1 to 1.6 for Large K_s	60
4.10	Variation in Thickness Curves for a Change in n_s . . .	61

4.11	Variation in Thickness Curves as K_f Varies from 0 to .2.	62
4.12	Enlarged View for the Changes in n_s and K_s for a Bare Substrate.	64
5.1	Oxidation Rate Δ Shifts vs. Log(time).	66
5.2	The Data Measured on Sample A at Spot 1 for Successive Heatings	71
5.3	The Data Measured on Sample A at Spot 2 for Successive Heatings	72
5.4	The Data Measured on Sample A at Spot 3 for Successive Heatings	73
5.5	The Data Measured on Sample A at Spot 4 for Successive Heatings	74
5.6	The Data Measured on Sample A at Spot 5 for Successive Heatings	75
5.7	The Data Measured on Sample B Compared with Data from Spot 1 on Sample A	76
5.8	Comparison of Data to Curves for $n_f = 1.6$ and 1.7 (No Extinction Coefficient).	77
5.9	Comparison of Data to Curves Where the Film Index has an Extinction Coefficient.	79
5.10	Comparison of Data to Curves Where the Film Extinction Coefficient Varies with Thickness.	80
5.11	Calculated Changes in n and K due to Surface Roughness of Glass	82
5.12	Comparison of Several Curves Demonstrating a Lack of Uniqueness for the Curve Fit	84
5.13	Comparison of the Values for the Substrate Index Found by Various Authors	85
5.14	Theoretical Film Thickness as a Function of Δ	89
5.15	Theoretical Curve with Best Fit for the Measured Data.	91
5.16	A Monotonic Function of t_c Used in the Theory Analysis	94

5.17	Error Analysis for Theory Relevance.	95
5.18	Sensitivity of Theory Curve to Changes in K_f	97
5.19	Sensitivity of Theory Curve to Changes in K_s	98
5.20	Sensitivity of Theory Curve to Changes in n_s	99
5.21	Sensitivity of Theory Curve to Changes in θ_i	101
6.1	Data from Alclad Sample 1.	110
6.2	Data from Alclad Sample 2 Taken at Sample Angles of Both 0° and 90° with Trajectories of Increasing Thickness.	111
6.3	Data from Alclad Sample 3 Taken at Sample Angles of Both 0° and 90° with Trajectories of Increasing Thickness.	112
6.4	Data from Alclad Sample 2 with Lines of Constant Thickness.	114
6.5	Data from Alclad Sample 3 with Lines of Constant Thickness.	115
6.6	Lines of Constant Thickness Derived from Variations in n_s Compared with Data from Sample 3 Spot a. . . .	116
6.7	Lines of Constant Thickness Derived from Variations in K_s Compared with Data from Sample 3 Spot a. . . .	118
6.8	Lines of Constant Thickness Derived from Variations of Both n_s and K_s Compared to Data from Sample 3 Spot a	119
6.9	Lines of Constant Thickness Derived from Variations in n_s where K_s and K_f are Functions of n_s Compared with Data from Sample 3.	121
6.10	Lines of Constant Thickness Derived from Variations in n_s where K_s and K_f are Functions of n_s Compared with Data from Sample 2.	122
6.11	Comparison of K_s and K_f with n_s	123
6.12	Apparent Values of n and K for Rough Surfaces Derived using Triangular, Square and Pyramid Models.	124

6.13	The Changes in Samples 2 and 3 Due to Changes in the Sample Angle	126
6.14	Data from Sample 4 at Various Sample Angles.	127

SECTION I

INTRODUCTION

When aluminum is exposed to air, oxidation occurs almost instantly. Thin films of aluminum oxide form on all surfaces of aluminum. When heated, the thickness of the oxide films increases.

Ellipsometry is a well established method of measuring properties of thin films on optically flat surfaces. The use of ellipsometry for rougher surfaces is unusual and there is no established method for determining the relevant optical properties of the film and substrate. These properties must be known in order to determine the film thickness.

A new method for determining these properties is the use of a data trajectory found by repeatedly heating and then measuring the values of ψ and Δ for a given sample. The thickness (and roughness) of an oxide film will grow with heat and a series of data points is generated, characterized by increasing (unknown) thickness. This method was first used by Cap. M. Lydon[1] at Texas Tech University in 1975. This trajectory can be used to relate the growth of the oxide film to the complex refractive indices of film and substrate:

$$\tilde{n}_f = n_f(1 + jK_f) \text{ and } \tilde{n}_s = n_s(1 + jK_s) \quad .$$

This relationship is very complicated and requires the use of a computer for the calculations.

The study of optically flat aluminum surfaces was undertaken in this work, using data trajectories as described above. In order to

interpret the data, a policy of using the data trajectories to define functional relationships between media parameters has been developed. It was found that the oxide roughness on nearly ideal aluminum surfaces can be modelled by taking the film extinction coefficient K_s to be a function of film thickness, t :

$$K_f = (0.01)^{\frac{t}{50}}$$

and by imposing a relation between the real and imaginary parts of the aluminum substrate index:

$$K_s = 7.175 - \frac{3}{2} n_s$$

This relation also interpolates all widely scattered values for the index of aluminum found in the literature. The actual thickness of the oxide film is the key to picking the correct values of n_s and K_s . As the data collected in this study was compared with work by others, a reasonable choice for the aluminum refractive index was selected:

$$\tilde{n}_s = 1.08(1 + j5.555)$$

Application of the trajectory idea to the rougher surface of alclad aluminum indicated that rough surfaces could also be modelled by variation of index parameters. It was found that substrate surface roughness could be modelled by increasing the value of n_s and requiring K_s to be a function of n_s :

$$K_s = 9.75 - 4.77n_s + 0.505n_s^2$$

Also, the effective value for K_f was found to be a function of both t and n_s when the substrate surface is rough:

$$K_f = (0.01) \frac{t}{50} n_s \quad .$$

The ideas employed in the present work, using data trajectories to determine effective parameter relationships, show great promise for work with thin films on both smooth and slightly rough surfaces. For example, it was possible to associate the present roughness criterion to the orientation of rolling grain marks on the alclad samples. This interesting check is described in Section VI.

In Section II the reflection coefficients and their relation to the film and substrate parameters n_f , K_f , n_s , K_s and t are derived. These are then related to the parameters ψ and Δ . The mechanics of the actual ellipsometric measurement of the values of ψ and Δ are discussed in Section III. In Section IV an analysis of errors in the ellipsometric measurements and a sensitivity study for the various parameters are given. The study of optically flat aluminum surfaces is described in Section V. Finally, the study of the oxide layers on alclad alloy is described in Section VI.

SECTION II

THEORETICAL BASIS OF ELLIPSOMETRY

Ellipsometry is a method of measuring the changes in light as it is reflected by a surface in order to determine the physical properties of that surface. To understand what changes as light reflects from a surface and how this is related to that surface, it is necessary to study some of the basic properties of light. This chapter gives a brief description of the laws governing the reflection and refraction of light.

In ellipsometry the light used is a plane wave of monochromatic light. The surface on which measurements are made must be smooth and flat with respect to the wavelength of light. It must be remembered that measurements are made with light at only one wavelength and the index of refraction can be different at other wavelengths.

Light is part of the electromagnetic spectrum and is governed by Maxwell's Equations which describe the electromagnetic field. These equations relate the electric vector, \vec{E} , the magnetic induction, \vec{B} , the electric displacement, \vec{D} , the magnetic vector, \vec{H} , and the electric current density, \vec{J} . Maxwell's Equations are:

$$\nabla \times \vec{H} - \frac{\partial \vec{D}}{\partial t} = \vec{J} \quad (2.1)$$

$$\nabla \times \vec{E} = - \frac{\partial \vec{B}}{\partial t} \quad (2.2)$$

$$\nabla \cdot \vec{D} = \rho \quad (2.3)$$

$$\nabla \cdot \vec{B} = 0 \quad (2.4)$$

These five basic quantities are further related by

$$\vec{J} = \sigma \vec{E} \quad (2.5)$$

$$\vec{D} = \epsilon \vec{E} \quad (2.6)$$

$$\vec{B} = \mu \vec{H} \quad (2.7)$$

Here σ is called the conductivity, ϵ is known as the permittivity, and μ is called the permeability. These three terms describe the properties of the media in which the electric field is propagating. When $\sigma = 0$ the media is non-conducting and the electric conduction current density, \vec{J} , vanishes. The electromagnetic components are not damped as the wave propagates through the media and the material appears transparent. The properties of light are easier to describe for nonabsorbing (non-conducting) media than for a conducting material. The laws of reflection and refraction will first be described for surfaces with $\sigma = 0$.

For a medium that is homogeneous and contains no charges or currents, $\vec{J} = 0$ and $\sigma = 0$, Maxwell's Equations can be used to derive two wave equations:

$$\nabla^2 \vec{E} - \epsilon\mu \frac{\partial^2 \vec{E}}{\partial t^2} = 0 \quad (2.8)$$

and

$$\nabla^2 \vec{H} - \epsilon\mu \frac{\partial^2 \vec{H}}{\partial t^2} = 0 \quad (2.9)$$

When the field is monochromatic with angular frequency ω , the time

derivative $\frac{\partial}{\partial t} = -i\omega$ for \vec{E} and \vec{H} of the form $\vec{E} = E_0 e^{-i\omega t}$. The solutions for the above wave equations are

$$\vec{E} = E_0 e^{i(kz' - \omega t)} \quad (2.10)$$

and

$$\vec{H} = H_0 e^{i(kz' - \omega t)} \quad (2.11)$$

where the propagation is in the \hat{z}' direction and $k = \sqrt{\epsilon\mu} \omega$.

When light falls upon a boundary between two media and is transmitted into the second media, the wavefront is continuous, although it has a kink at the boundary as shown in Fig. (2.1). The wave appears to be bent at the boundary. The velocity of propagation of the wave changes at the boundary and the amount of refraction or bend is related to the change in velocity. The ratio of the first velocity to the second is called the refractive index for refraction from the first media to the second.

$$n_{12} = \frac{v_1}{v_2} \quad (2.12)$$

An "absolute refractive index" can also be found, it is the ratio of the velocity of light in a vacuum to the velocity in the media,

$$n = \frac{c}{v} \quad (2.13)$$

If the absolute refractive indices of two media, n_1 and n_2 are known, then the refraction from the first media to the second can be found,

$$n_{12} = \frac{n_2}{n_1} = \frac{v_1}{v_2} \quad (2.14)$$

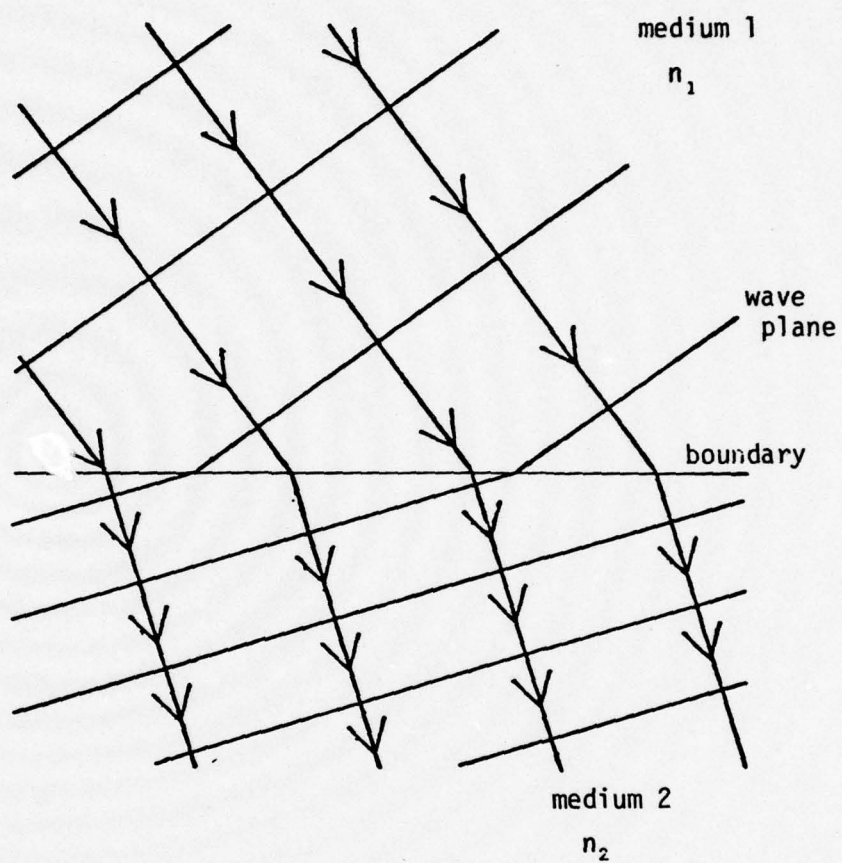


Fig. 2.1 The Bending of Light at the Interface of Two Media

The refractive index or the index of refraction, as it is often called, is defined to be

$$n = \sqrt{\frac{\epsilon\mu}{\epsilon_0\mu_0}} \quad (2.15)$$

where ϵ_0 and μ_0 are vacuum permittivity and permeability.

The laws of reflection and refraction can be derived from Maxwell's Equations, but they were discovered experimentally long before Maxwell's time. The incident beam is assumed to be a plane wave, the wavefronts being normal to the incident ray. The reflected and refracted rays lie in the plane formed by the incident ray and the normal to the surface at the point of incidence. This plane is shown in Fig. (2.2). The angle of incidence (θ_i), the angle of reflection (θ_r), and the angle of refraction (θ_t) are measured between the normal to the surface and the appropriate ray. For reflection:

$$\theta_i = \theta_r \quad (2.16)$$

For refraction:

$$n_1 \sin\theta_i = n_2 \sin\theta_t \quad (2.17)$$

This is often called Snell's law.

To fully describe reflected and refracted waves it is necessary to know more than the angle of propagation. The amplitude of these waves must also be found. Expressions describing the amplitudes of the reflected and refracted waves are found by imposing the boundary conditions. These conditions demand that the tangential components of \vec{E} and

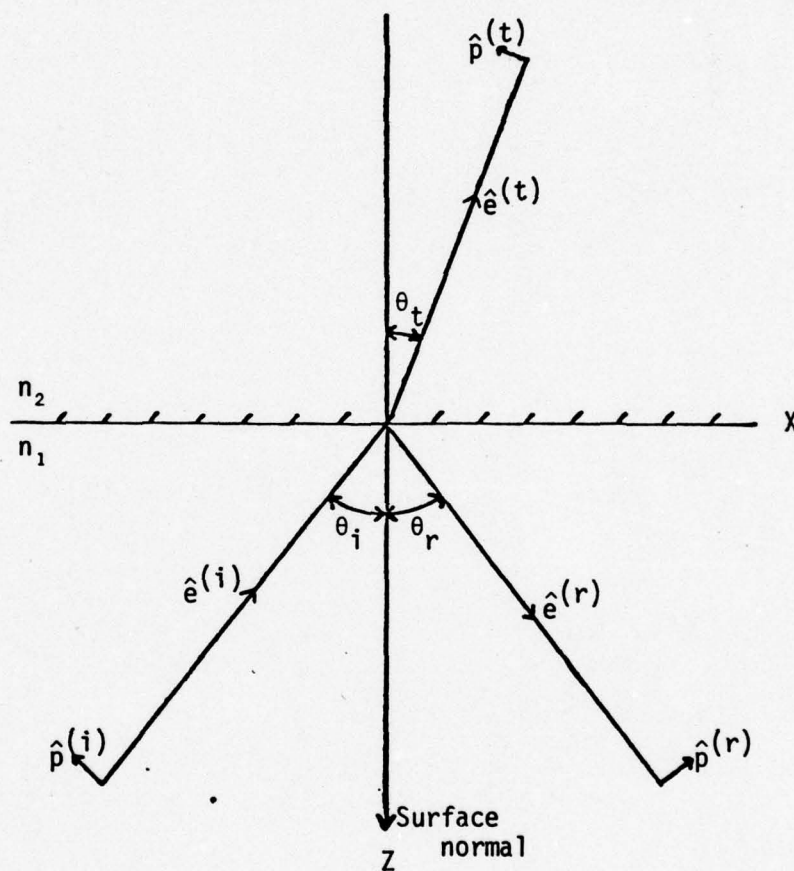


Fig. 2.2 Ray Plane Showing Incident, Reflected, and Transmitted Rays

\vec{H} must be continuous across the boundary.

For convenience in discussing the boundary conditions, the electric and magnetic fields will be described in terms of amplitudes $\vec{E}(t)$ and $\vec{H}(t)$, obtained by extracting the propagation factor $\exp(ikz')$:

$$\begin{aligned}\vec{E} &= \vec{E}(t)e^{ikz'} \\ \vec{H} &= \vec{H}(t)e^{ikz'}\end{aligned}\tag{2.18}$$

where z' measures distance in the direction of propagation. As shown in Fig. (2.2), the incident plane wave propagates in the direction of the unit vector $\hat{e}^{(i)}$. The unit vectors $\hat{e}^{(r)}$ and $\hat{e}^{(t)}$ represent the direction of propagation of the reflected wave and the transmitted wave, respectively.

The tangential field components can be described in terms of the coordinate system shown in Fig. (2.2). The z axis is normal to the boundary, the x axis is on the boundary and in the plane of incidence, and the y axis is on the boundary but normal to the plane of incidence. In order for the tangential components of \vec{E} and \vec{H} to be continuous, the following conditions must be satisfied:

$$\begin{aligned}E_x^{(i)} + E_x^{(r)} &= E_x^{(t)} \\ E_y^{(i)} + E_y^{(r)} &= E_y^{(t)} \\ H_x^{(i)} + H_x^{(r)} &= H_x^{(t)} \\ H_y^{(i)} + H_y^{(r)} &= H_y^{(t)}\end{aligned}\tag{2.19}$$

For the purposes of ellipsometry, the components shown above are conveniently replaced by related components, which will now be introduced. The y-components, perpendicular to the plane of incidence, will be called the s-components, a trivial change of name. The remaining components of the amplitudes of the three beams, however, will be described in terms of three unit vectors $\hat{p}^{(\alpha)}$ where α represents i, r or t:

$$\begin{aligned}\hat{p}^{(i)} &\equiv \hat{y} \times \hat{\epsilon}^{(i)} \equiv \hat{s} \times \hat{\epsilon}^{(i)} \\ \hat{p}^{(r)} &\equiv \hat{y} \times \hat{\epsilon}^{(r)} \equiv \hat{s} \times \hat{\epsilon}^{(r)} \\ \hat{p}^{(t)} &\equiv \hat{y} \times \hat{\epsilon}^{(t)} \equiv \hat{s} \times \hat{\epsilon}^{(t)}\end{aligned}\tag{2.20}$$

where $\hat{s} \equiv \hat{y}$.

Using these unit vectors, the electric field amplitudes of the three beams can be written:

$$\begin{aligned}\vec{E}^{(i)} &= A_s \hat{s} + A_p \hat{p}^{(i)} \\ \vec{E}^{(r)} &= R_s \hat{s} + R_p \hat{p}^{(r)} \\ \vec{E}^{(t)} &= T_s \hat{s} + T_p \hat{p}^{(t)}\end{aligned}\tag{2.21}$$

Now, in the x, y, z coordinate system the components of the three directions of propagation $\hat{\epsilon}$ and the three related vectors $\hat{\epsilon}_p^{(\alpha)}$ are:

$$\hat{\epsilon}^{(i)} = \begin{pmatrix} \sin\theta_i \\ 0 \\ -\cos\theta_i \end{pmatrix}_{x,y,z}, \quad \hat{p}^{(i)} = \begin{pmatrix} -\cos\theta_i \\ 0 \\ -\sin\theta_i \end{pmatrix}_{x,y,z}$$

$$\begin{aligned}
 \hat{\epsilon}^{(r)} &= \begin{pmatrix} \sin\theta_i \\ 0 \\ \cos\theta_i \end{pmatrix}_{x,y,z}, & \hat{p}^{(r)} &= \begin{pmatrix} \cos\theta_i \\ 0 \\ -\sin\theta_i \end{pmatrix}_{x,y,z} \\
 \hat{\epsilon}^{(t)} &= \begin{pmatrix} \sin\theta_t \\ 0 \\ -\cos\theta_t \end{pmatrix}_{x,y,z}, & \hat{p}^{(t)} &= \begin{pmatrix} -\cos\theta_t \\ 0 \\ -\sin\theta_t \end{pmatrix}_{x,y,z}
 \end{aligned} \tag{2.22}$$

Substituting Eqs. (2.22) into Eqs. (2.21), one obtains:

$$\begin{aligned}
 \vec{E}^{(i)} &= \begin{pmatrix} -A_p \cos\theta_i \\ A_s \\ -A_p \sin\theta_i \end{pmatrix}_{x,y,z} = \begin{pmatrix} E_x^{(i)} \\ E_y^{(i)} \\ E_z^{(i)} \end{pmatrix} \\
 \vec{E}^{(r)} &= \begin{pmatrix} R_p \cos\theta_i \\ R_s \\ -R_p \sin\theta_i \end{pmatrix}_{x,y,z} = \begin{pmatrix} E_x^{(r)} \\ E_y^{(r)} \\ E_z^{(r)} \end{pmatrix} \\
 \vec{E}^{(t)} &= \begin{pmatrix} -T_p \cos\theta_t \\ T_s \\ -T_p \sin\theta_t \end{pmatrix}_{x,y,z} = \begin{pmatrix} E_x^{(t)} \\ E_y^{(t)} \\ E_z^{(t)} \end{pmatrix}
 \end{aligned} \tag{2.23}$$

The magnetic fields $\vec{H}^{(i)}$, $\vec{H}^{(r)}$, and $\vec{H}^{(t)}$ may be obtained from the relation:

$$\vec{H}^{(\alpha)} = \sqrt{\frac{\epsilon}{\mu}} \hat{\epsilon}^{(\alpha)} \times \vec{E}^{(\alpha)} \tag{2.24}$$

where α represents i , r , or t . Using Eqs. (2.22) and (2.23) in Eq. (2.24) one obtains:

$$\begin{aligned}
 \vec{H}^{(i)} &= \sqrt{\frac{\epsilon_1}{\mu_1}} \begin{pmatrix} A_S \cos \theta_i \\ A_P \\ A_S \sin \theta_i \end{pmatrix}_{x,y,z} = \begin{pmatrix} H_x^{(i)} \\ H_y^{(i)} \\ H_z^{(i)} \end{pmatrix} \\
 \vec{H}^{(r)} &= \sqrt{\frac{\epsilon_1}{\mu_1}} \begin{pmatrix} -R_S \cos \theta_i \\ R_P \\ R_S \sin \theta_i \end{pmatrix}_{x,y,z} = \begin{pmatrix} H_x^{(r)} \\ H_y^{(r)} \\ H_z^{(r)} \end{pmatrix} \\
 \vec{H}^{(t)} &= \sqrt{\frac{\epsilon_2}{\mu_2}} \begin{pmatrix} T_S \cos \theta_t \\ T_P \\ T_S \sin \theta_t \end{pmatrix}_{x,y,z} = \begin{pmatrix} H_x^{(t)} \\ H_y^{(t)} \\ H_z^{(t)} \end{pmatrix} .
 \end{aligned} \tag{2.25}$$

The representations in Eqs. (2.23) and (2.25) may now be substituted into boundary conditions, Eq. (2.19) to obtain:

$$\begin{aligned}
 [-A_P + R_P] \cos \theta_i &= -T_P \cos \theta_t \\
 A_S + R_S &= T_S \\
 n_1 [A_S - R_S] \cos \theta_i &= n_2 T_S \cos \theta_t \\
 n_1 [A_P + R_P] &= n_2 T_P
 \end{aligned} \tag{2.26}$$

where the approximations

$$\mu_1 \approx \mu_2 \approx \mu_0$$

have been made, so that

$$\sqrt{\frac{\epsilon_1}{\mu_1}} / \sqrt{\frac{\epsilon_2}{\mu_2}} = \sqrt{\frac{\epsilon_1 \mu_0}{\epsilon_2 \mu_0}} = \sqrt{\frac{\epsilon_1 \mu_1}{\epsilon_2 \mu_2}} = \frac{n_1}{n_2} \quad (2.27)$$

From these Eqs. (2-27), it can be observed that the parallel and perpendicular components of the lightwaves are independent of each other. These four equations can be solved for the amplitude of the reflected and transmitted waves independently as a function of the incident wave amplitude for both the parallel and perpendicular cases:

$$\begin{aligned} t_p &\equiv \frac{T_p}{A_p} = \frac{2n_1 \cos \theta_i}{n_2 \cos \theta_i + n_1 \cos \theta_t} \\ t_s &\equiv \frac{T_s}{A_s} = \frac{2n_1 \cos \theta_i}{n_1 \cos \theta_i + n_2 \cos \theta_t} \\ r_p &\equiv \frac{R_p}{A_p} = \frac{n_2 \cos \theta_i - n_1 \cos \theta_t}{n_2 \cos \theta_i + n_1 \cos \theta_t} \\ r_s &\equiv \frac{R_s}{A_s} = \frac{n_1 \cos \theta_i - n_2 \cos \theta_t}{n_1 \cos \theta_i + n_2 \cos \theta_t} \end{aligned} \quad (2.28)$$

The above equations are called the Fresnel Equations and the quantities r_p , r_s , t_p , and t_s are called Fresnel reflection coefficients and Fresnel transmission coefficients.

When the conductivity σ is not zero these equations are changed slightly. The wave equation is changed to

$$\nabla^2 \vec{E} = \mu \epsilon \frac{\partial^2 \vec{E}}{\partial t^2} + \mu \sigma \frac{\partial \vec{E}}{\partial t} \quad (2.29)$$

The plane wave solution is

$$\vec{E} = \vec{E}_0 e^{i(\tilde{k} z' - \omega t)} \quad (2.30)$$

where

$$\tilde{k}^2 = \omega^2 \mu \left(\epsilon + i \frac{\sigma}{\omega} \right) \quad (2.31)$$

All of the previous equations are the same for a conducting medium if the dielectric constant ϵ is replaced by a complex term

$$\tilde{\epsilon} = \epsilon + i \frac{\sigma}{\omega} \quad (2.32)$$

In addition, the phase velocity, \tilde{v} , and the index of refraction, \tilde{n} , also become complex:

$$\tilde{v} \equiv \frac{\omega}{\tilde{k}} = \frac{1}{\sqrt{\mu \tilde{\epsilon}}} \quad (2.33)$$

and

$$\tilde{n} \equiv \frac{c}{\tilde{v}} = \sqrt{\frac{\mu \tilde{\epsilon}}{\mu_0 \epsilon_0}} = \sqrt{\frac{\mu \epsilon}{\mu_0 \epsilon_0} \left(1 + i \frac{\sigma}{\epsilon \omega} \right)} \quad (2.34)$$

The complex index of refraction can be divided into a real and imaginary part,

$$\tilde{n} \equiv n(1 + iK) \quad (2.35)$$

here K referred to as the extinction coefficient [2], [3]. The two real quantities, n and K , defined in Eq. (2.35) can be related to the media parameters by equating expressions for \tilde{n}^2 obtained from

Eq. (2.34) and Eq. (2.35):

$$\begin{aligned}\tilde{n}^2 &= \frac{\mu\epsilon}{\mu_0\epsilon_0} \left(1 + i\frac{\sigma}{\epsilon\omega}\right) \\ &= n^2(1 - K^2 + 2iK)\end{aligned}$$

Comparing real and imaginary parts, one finds

$$n^2(1 - K^2) = \frac{\mu\epsilon}{\mu_0\epsilon_0}$$

and

(2.36)

$$n^2K = \frac{\sigma\mu}{2\epsilon_0\mu_0\omega} = \frac{c^2\sigma\mu}{2\omega}$$

Solving Eqs. (2.36) for n and K , one finds:

$$K = \frac{\epsilon\omega}{\sigma} \left[\sqrt{1 + \left(\frac{\sigma}{\epsilon\omega}\right)^2} - 1 \right] \approx \frac{\sigma}{2\epsilon\omega}$$

(2.37)

$$n = c \sqrt{\frac{\sigma\mu}{2\omega K}} \approx c \sqrt{\mu\epsilon}$$

where the approximate forms are useful when $K \ll 1$; i.e., when $(\sigma/\epsilon\omega) \ll 1$.

Using the notation introduced above, the complex propagation constant in Eq. (2.30) can be expressed in the form:

$$\tilde{k} = \frac{\omega}{\tilde{v}} = \frac{\omega}{c} \tilde{n} = \frac{\omega}{c} n(1 + iK)$$

(2.38)

Thus, the plane wave solution of Eq. (2.30) can be written:

$$\vec{E} = \vec{E}_0 e^{-\frac{\omega}{c} n K z} e^{i\left(\frac{\omega}{c} n z - \omega t\right)}$$

(2.39)

The first exponential term in this expression is of the form $e^{-\frac{\alpha}{2}z}$ where the power damping constant is given by

$$\alpha = \frac{2\omega}{c}nK = \frac{4\pi}{\lambda_0}nK \quad , \quad (2.40)$$

with λ_0 being the vacuum wavelength of the light. For metals with large conductivity, K is large, so that the field is damped so strongly that it can penetrate only a fraction of a wavelength into the material.

It should be mentioned that the expression for K given in Eq. (2.37) has a severe defect in that the derivation has presumed that $(\alpha/\epsilon\omega) \geq 0$. If one defines this ratio to be γ :

$$\gamma \equiv \frac{\alpha}{\epsilon\omega} \quad ,$$

then, according to Eq. (2.37),

$$K = \frac{\sqrt{1 + \gamma^2} - 1}{\gamma}$$

so that

$$0 \leq K \leq 1 \quad \text{for all } \gamma \geq 0 \quad . \quad (2.41)$$

Nevertheless, many metals which are good conductors must be described by values of K that are considerably larger than one, say K approximately three or five. This point is discussed at some length in Born and Wolf[4]. It is actually necessary to consider ϵ to be negative. This unpleasant feature arises because the media parameters actually depend on frequency. In other words, Maxwell's

Equations are not truly linear in the fields so that the Fourier decomposition shown in Eq. (2.30) is not strictly appropriate. The results shown in Sections V and VI of this study, in fact, demonstrate values of K considerably larger than one.

The effects of a complex index of refraction on the reflection and refraction of light at a boundary, are such that the basic formulas all have been exactly the same form. One need only interpret the various parameters as being complex. The law of refraction, or Snell's Law becomes

$$\tilde{n}_2 \sin \theta_t = n_1 \sin \theta_i \quad (2.42)$$

for the case in which light travels from a media such as air ($\sigma = 0$) to some media where the index of refraction is complex ($\sigma \neq 0$). Since \tilde{n}_2 is complex, the angle, θ_t , must also be complex and will henceforth be denoted as $\tilde{\theta}_t$. The Fresnel Equations are also effected by a complex index of refraction as well as by the complex angle. Looking first at the reflection coefficients,

$$\tilde{r}_p = \frac{\tilde{n}_2 \cos \theta_i - n_1 \cos \tilde{\theta}_t}{\tilde{n}_2 \cos \theta_i + n_1 \cos \tilde{\theta}_t} \quad (2.43)$$

$$\tilde{r}_s = \frac{n_1 \cos \theta_i - \tilde{n}_2 \cos \tilde{\theta}_t}{n_1 \cos \theta_i + \tilde{n}_2 \cos \tilde{\theta}_t} \quad (2.44)$$

Since \tilde{n}_2 and $\tilde{\theta}_t$ are now complex, the reflection coefficients \tilde{r}_p and \tilde{r}_s are also complex. The transmission coefficients also become complex,

$$\tilde{t}_p = \frac{2 n_1 \cos \theta_i}{\tilde{n}_2 \cos \theta_i + n_1 \cos \tilde{\theta}_t} \quad (2.45)$$

$$\tilde{t}_s = \frac{2 \tilde{n}_1 \cos \theta_i}{\tilde{n}_1 \cos \theta_i + \tilde{n}_2 \cos \theta_t} \quad (2.46)$$

The complex values of the reflection and transmission coefficients mean that the ratio of transmitted or reflected light amplitude to the incident light amplitude is complex. This means that a phase change occurs when light is transmitted or reflected from a boundary where one or both of the media is complex. Now that it is clear that the effects of conductivity ($\sigma \neq 0$) can be accounted for by simply understanding the indices and coefficients to be complex, the notation will be simplified by dropping the wavy bar over complex quantities; e.g., $\tilde{r}_p \equiv r_p$.

A full description of all properties of the light reflected by and transmitted through a media interface would require determination of all four of the complex Fresnel coefficients. This, however, is more information than can be obtained from ellipsometry alone. The ellipsometry procedure described in the next section is able to determine only the complex number which is the ratio of the complex reflection coefficients r_p and r_s :

$$\frac{r_p}{r_s} \equiv \frac{R_p A_s}{R_s A_p} = (\tan \psi) e^{i\Delta} \quad (2.47)$$

With an ellipsometer, the angles ψ and Δ can be determined rather easily.

The behavior of light when it reflects from a surface with a thin film can also be predicted. The boundaries at both surfaces, air-film and film-substrate, are involved in this case. The change in light due

to reflection can again be described in terms of angles ψ and Δ . It should be noted that it is the total reflected light which is compared to the incident light. The quantities ψ and Δ can again be described in terms of reflection coefficients, but the coefficients come from two boundaries and the terms are more complicated.

For this case some light is reflected off the film, but some light is transmitted through the film and reflected from the third media and transmitted back through the film as illustrated in Fig. (2.3). The reflected light may be considered to be made up of a series of separate beams. The first, reflected at the first boundary, is designated as R_1 and is simply found:

$$R_1 = A r_{01} \quad . \quad (2.48)$$

The rest of the beams are transmitted through the film and reflected at the next interface. The second beam is the first one transmitted at the thin film - air interface and is designated R_2 . The other beams are reflected between the two interfaces until they are transmitted through the thin film - air interface. These successive beams, designated as R_3, R_4, R_5, \dots , have a smaller and smaller intensity depending on the reflection coefficients:

$$R_2 = A t_{01} r_{12} t_{10} e^{-i2\delta} \quad (2.49)$$

$$R_3 = A t_{01} r_{12}^2 r_{10} t_{10} e^{-i4\delta} \quad . \quad (2.50)$$

The light beams transmitted through the thin film are delayed in phase

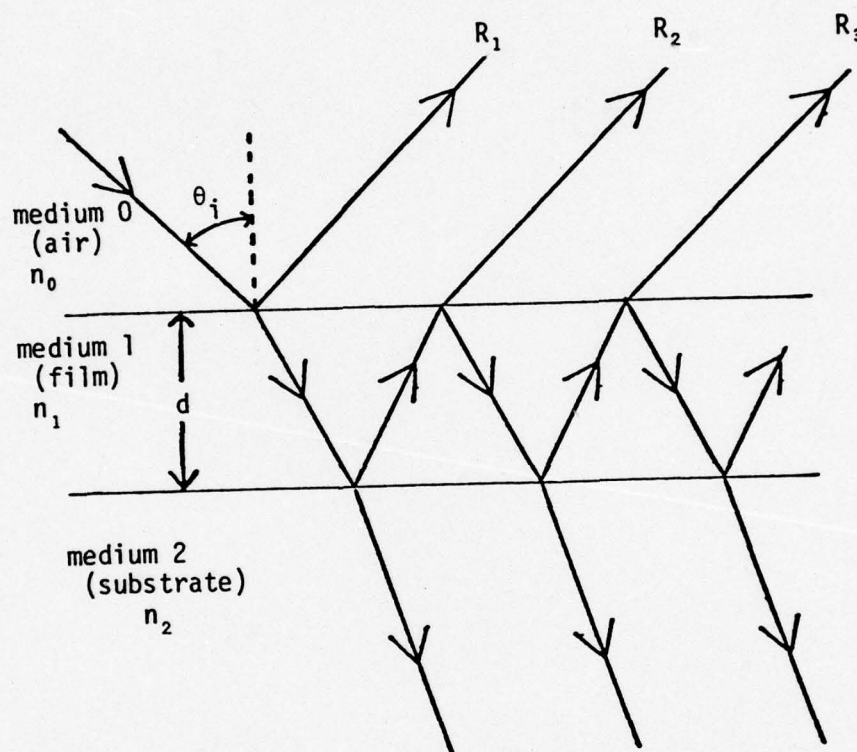


Fig. 2.3 Reflection of Light from Two Boundaries
(Substrate with Film)

by an amount 2δ for each pass back and forth through the thin film because of the extra time needed to travel the extra distance. This phase delay is easily determined to be:

$$2\delta = \frac{4\pi d}{\lambda_0} \sqrt{n_1^2 - \sin^2 \theta_i} \quad (2.51)$$

where d is the film thickness. The reflection and transmission coefficients, r and t , above can represent either the parallel or the perpendicular components. The subscripts on r and t describe the boundary the light beam hits, for example, t_{10} , is the transmission coefficient for light going from medium 1 to medium 0.

The total amplitude for all reflected light is

$$R = R_1 + R_2 + R_3 + R_4 + \dots \quad (2.52)$$

Using the pattern developed in Eqs. (2.49) and (2.50), one can write

$$\frac{R}{A} = r_{01} + \frac{t_{01}t_{10}}{r_{10}} \sum_{\ell=1}^{\infty} [r_{12}r_{10}e^{-2i\delta}]^{\ell} \quad (2.53)$$

This sum is just a geometric series so that it is trivial to obtain a closed form. Also, certain simplifications are possible. From the explicit expressions shown in Eq. (2.28), one can deduce that

$$r_{10} = -r_{01}$$

and

$$t_{01}t_{10} = (1 - r_{01}^2) \quad (2.54)$$

Using Eqs. (2.54) and performing the sum in Eq. (2.53), one obtains:

$$\frac{R}{A} = \frac{r_{01} + r_{12} e^{-2i\delta}}{1 + r_{01}r_{12} e^{-2i\delta}} \quad (2.55)$$

For the separate parallel and perpendicular components of the light, one has:

$$r_s = \frac{R_s}{A_s} = \frac{r_{01}^s + r_{12}^s e^{-i2\delta}}{1 + r_{10}^s r_{12}^s e^{-i2\delta}} \quad (2.56)$$

$$r_p = \frac{R_p}{A_p} = \frac{r_{01}^p + r_{12}^p e^{-i2\delta}}{1 + r_{10}^p r_{12}^p e^{-i2\delta}},$$

so that Eq. (2.47) becomes:

$$\tan \psi e^{+i\Delta} = \frac{r_{01}^p + r_{12}^p e^{-i2\delta}}{1 + r_{10}^p r_{12}^p e^{-i2\delta}} \cdot \frac{1 + r_{10}^s r_{12}^s e^{-i2\delta}}{r_{10}^s + r_{12}^s e^{-i2\delta}} \quad (2.57)$$

Eq. (2.57) is the desired connection between the parameters ψ and Δ , determined with the ellipsometer, and the media parameters

$n_0 \equiv 1$ = index of refraction of air,

$$\tilde{n}_f \equiv n_f (1 + iK_f), \quad (2.58)$$

$$\tilde{n}_s \equiv n_s (1 + iK_s),$$

and

$d \equiv$ film thickness

characterizing the film and substrate. Since these media parameters

enter Eq. (2.57) through expressions of the form given in Eq. (2.28), it is clear that the relationship between ψ and Δ and the media parameters is arithmetically rather complicated. Nevertheless, if only two of the media parameters are unknown, then measurement of ψ and Δ for a given angle, θ_i , permits computation of the two unknowns. This computation is accomplished by digital computer.

There exists a vast collection of literature on the subject of ellipsometry. The Bibliography attached presents a useful sampling of this previous work. This literature deals not only with the relationship of the index parameters n_s , K_s , n_f , K_f and t to the quantities ψ and Δ , but also with the alignment and use of the instrument itself. The next section relates the values of ψ and Δ to the actual method by which these parameters are obtained.

SECTION III

THE MECHANICS OF ELLIPSOMETRY

The ellipsometer essentially consists of two polarizers and a quarter wave plate. Light is supplied by a HeNe laser and a power meter is used as a detector.

The light from the laser passes through a collimator to a polarizer then through the quarter wave plate to the sample. After reflecting off the sample the light wave passes through the second polarizer to the detector. Fig. (3.1) gives a schematic representation of the ellipsometer in the plane of incidence. The collimator arm with its polarizer and quarter wave plate is stationary. The telescope arm with its polarizer can be rotated about a center axis. A table on which the sample is to be placed is centered at this axis.

The angle of the telescope arm can be read directly from a scale. This angle is measured from the collimator arm as 0° , so that, when light shines straight through from the collimator into the telescope arm, as in Fig. (3.2), the angle is 180° .

The angle of incidence, θ_i , can be found using this angle reading for a sample centered on the table. The sample table can be tilted to adjust the sample so the plane of incidence and the plane formed from the two arms of the ellipsometer are the same.

The polarizers on both the collimator and telescope arms are mounted on a circle calibrated to $.01^\circ$. They are set to read 0° when the electric vector of the light beam is horizontal (in the plane of

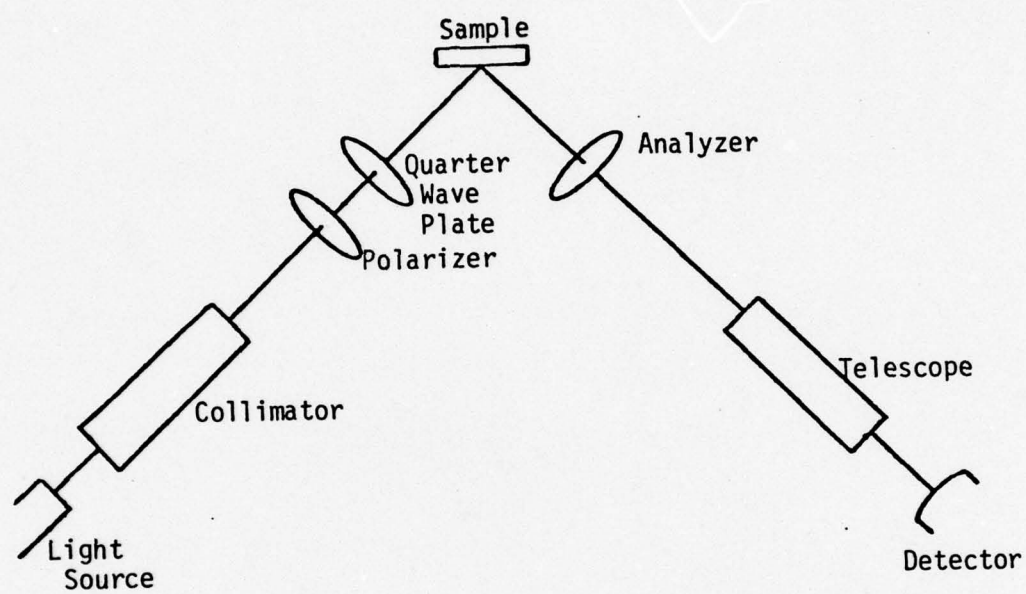


Fig. 3.1 Schematic Representation of the Ellipsometer with Sample Inserted

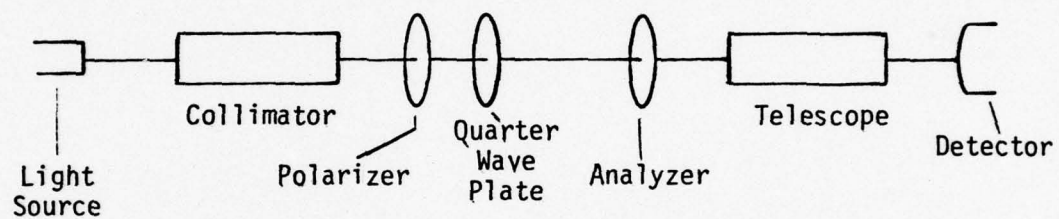


Fig. 3.2 Schematic Representation of the Ellipsometer with no Sample for Reflection

incidence). A quarter wave plate is essentially a flat transparent window with two axes, in the plane of the window at approximately 90° to each other, called the fast axis and the slow axis. For light passing through it, the quarter wave plate provides a phase delay of 90° for the portion of the light polarized along the slow axis with respect to the portion of the light polarized along the fast axis. The direction of polarization of light is considered to be the direction of the electric field vector.

The ellipsometer is used by adjusting the two polarizers so that light to the detector is a minimum. This is done by adjusting the combination of the polarizer and quarter wave plate in the collimating arm so that a delay between the parallel and perpendicular components is created which is just opposite that caused from the reflection of light from the sample. The light reflected from the sample is then linearly polarized and by placing the second polarizer at an angle of 90° the light can be extinguished.

It is useful to determine the relationship between the amplitudes A_p and A_s , defined in Section II, and the angle P of the polarizer. The quarter wave plate is set with the fast axis at an angle of $\alpha = 45^\circ$ with respect to the (horizontal) ray plane. To be specific, a unit vector along the fast axis and one along the slow axis are defined:

$$\begin{aligned}\hat{e}_{\text{fast}} &\equiv \frac{1}{\sqrt{2}} [\hat{s} + \hat{p}^{(i)}] \\ \hat{e}_{\text{slow}} &\equiv \frac{1}{\sqrt{2}} [\hat{s} - \hat{p}^{(i)}] \end{aligned} \quad (3.1)$$

The polarizer may be set at some arbitrary angle P with respect to the ray plane. A unit vector identifying the direction of polarization of light from the polarizer, can be defined:

$$\hat{e}_{pol} \equiv (\cos P) \hat{p}^{(i)} + (\sin P) \hat{s} \quad (3.2)$$

The input light comes out linearly polarized at angle P (polarized parallel to \hat{e}_{pol}) when it passes through the polarizer. If the magnitude of the amplitude of the electric vector is E_0 , then the parallel and perpendicular components, with respect to the ray plane, after passing through the polarizer are (in the notation of Section II):

$$\begin{aligned} E_p &= E_0 \cos P e^{-i\omega t} \\ E_s &= E_0 \sin P e^{-i\omega t} \end{aligned} \quad (3.3)$$

The light then passes through the quarter wave plate and the components along the fast and slow axes become:

$$\begin{aligned} E_{fast} &= E_0 [\cos P \cos 45^\circ + \sin P \sin 45^\circ] e^{-i\omega t} \\ E_{slow} &= E_0 [\cos P \cos 135^\circ + \sin P \cos 45^\circ] e^{-i(\omega t - \beta)} \end{aligned} \quad (3.4)$$

where β is the phase delay from the slow axis with respect to the fast axis. From these components the parallel and perpendicular components can be projected:

$$\vec{E}^{(i)} = A_s \hat{s} + A_p \hat{p}^{(i)}$$

where

$$\begin{aligned} A_s &= \frac{E_0}{2} [(\cos P + \sin P) + (\sin P - \cos P) e^{i\beta}] e^{-i\omega t} \\ A_p &= \frac{E_0}{2} [(\cos P + \sin P) - (\sin P - \cos P) e^{i\beta}] e^{-i\omega t} \end{aligned} \quad (3.5)$$

If the wave plate is adjusted to be a quarter wave plate for the wavelength of the laser source, then the delay β is 90° and these equations can be simplified to:

$$\begin{aligned} A_s &= \frac{1}{\sqrt{2}} E_0 e^{-i(\omega t - P + 45^\circ)} \\ A_p &= \frac{1}{\sqrt{2}} E_0 e^{-i(\omega t + P - 45^\circ)} \end{aligned} \quad (3.6)$$

Eqs. (3.6) give the desired relationship between A_s and A_p and the angle P of the polarizer.

The angles ψ and Δ introduced in Eq. (2.47) are defined:

$$(\tan \psi) e^{i\Delta} = \frac{R_p A_s}{R_s A_p} \quad (3.7)$$

In order to experimentally determine ψ and Δ , the following strategy can be employed. One can vary the angle P of the polarizer until linearly polarized light is reflected from the sample. This condition can be detected when there exists an angle A of the analyzer (the second polarizer) which will completely block the light reflected from the sample.

Thus, when the detector is "nulled" to the lowest attainable reading, then the light reflected from the sample is linearly polarized.

Under these conditions there are only two possibilities for the phase of R_p/R_s :

$$\textcircled{A} \text{ Phase } \left\{ \frac{R_p}{R_s} \right\} = 0, \text{ in which case one can take} \quad (3.8)$$

$$\tan\psi = \frac{R_p}{R_s} \text{ and } \Delta = \frac{A_s}{A_p} \text{ Phase } \left\{ \frac{A_s}{A_p} \right\}$$

or

$$\textcircled{B} \text{ Phase } \left\{ \frac{R_p}{R_s} \right\} = \pm 180^\circ, \text{ in which case one can take} \quad (3.9)$$

$$\tan\psi = -\frac{R_p}{R_s} \text{ and } \Delta = -180^\circ + \text{Phase } \left\{ \frac{A_s}{A_p} \right\}.$$

The expressions for $\tan\psi$ shown above are permitted because $|A_s/A_p| = 1$ as shown in Eq. (3.6). Also from Eq. (3.6), one finds

$$\text{Phase } \left\{ \frac{A_s}{A_p} \right\} = -2P + 90^\circ \quad (3.10)$$

Using Eq. (3.10) in Eqs. (3.8) and (3.9) the two cases may be expressed

$$\textcircled{A} \frac{R_p}{R_s} \geq 0, \tan\psi = \left| \frac{R_p}{R_s} \right|, \text{ and } \Delta = -2P + 90^\circ \quad (3.11)$$

or

$$\textcircled{B} \frac{R_p}{R_s} \leq 0, \tan\psi = \left| \frac{R_p}{R_s} \right|, \text{ and } \Delta = -2P - 90^\circ \quad (3.12)$$

Since the angle A of the analyzer is set at right angles to the plane of polarization of the light reflected from the sample, it is easy to

find the connection between A and ψ as illustrated in Fig. (3.3):

$$\begin{aligned} R_p &= \sqrt{R_p^2 + R_s^2} \cos(A + 90^\circ) \\ R_s &= \sqrt{R_p^2 + R_s^2} \sin(A + 90^\circ) \end{aligned} \quad (3.13)$$

so that, from either Eq. (3.11) or Eq. (3.12),

$$\tan\psi = \left| \frac{\cos(A + 90^\circ)}{\sin(A + 90^\circ)} \right| = \left| -\frac{\sin A}{\cos A} \right| = \left| -\tan A \right| \quad (3.14)$$

Furthermore,

$$\left\{ \frac{R_p}{R_s} = -\tan A \right\} \Rightarrow \begin{cases} \text{Case (A) pertains if } \tan A < 0 \\ \text{Case (B) pertains if } \tan A > 0 \end{cases} \quad (3.15)$$

Solutions of Eq. (3.14) for ψ can be restricted so that

$$\psi \in [0, 90^\circ] \quad (3.16)$$

with the following correspondences:

$$\begin{aligned} A \in [0, 90^\circ] &\Rightarrow \text{Case (B) and } \psi = A \\ A \in [90^\circ, 180^\circ] &\Rightarrow \text{Case (A) and } \psi = \pi - A \\ A \in [-90^\circ, 0] &\Rightarrow \text{Case (A) and } \psi = -A \\ A \in [-180^\circ, -90^\circ] &\Rightarrow \text{Case (B) and } \psi = \pi + A \end{aligned} \quad (3.17)$$

Without restriction, multiples of 360° can be added to or subtracted from the measured angle A to bring it into one of the ranges considered in Eqs. (3-17). Similarly, it is clear from Eq. (3.7) that Δ need only be determined mod 360° . Thus multiples of 360° can be added to and

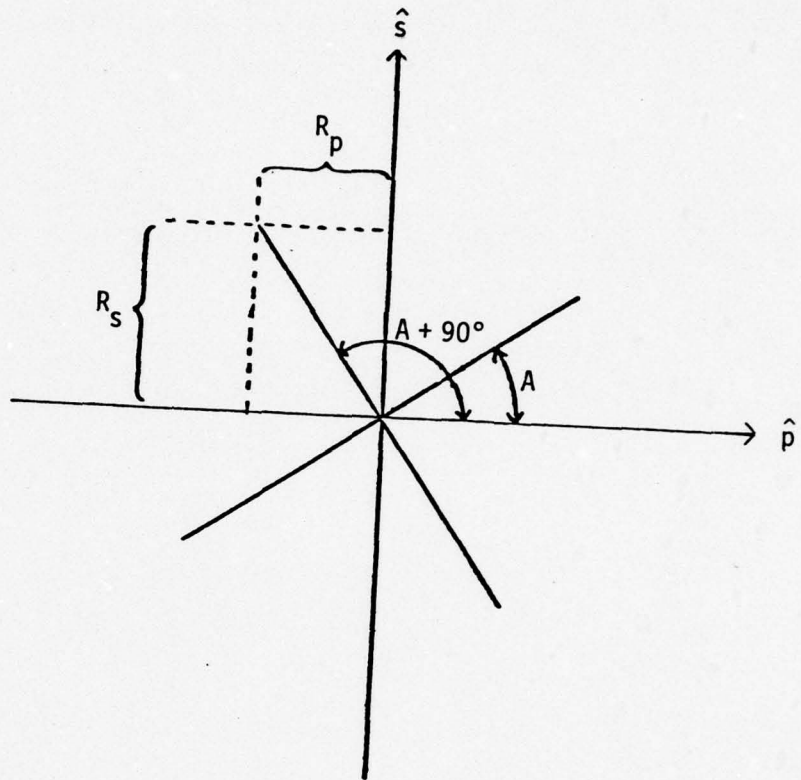


Fig. 3.3 Relationship of R_s and R_p to the Angle A

subtracted from the angles Δ determined in Eqs. (3.11) and (3.12).

Thus, the angle Δ may be taken to lie in the range

$$\Delta \in [0, 360^\circ] \quad . \quad (3.18)$$

The two cases encountered above arise because extinction by the analyzer can be achieved for two different angles P and P' , corresponding to

$$[-2P + 90^\circ] = \Delta \quad , \text{ Case (A)}$$

and

$$[-2P + 90^\circ] = \Delta + \pi \quad , \text{ Case (B)} \quad . \quad (3.19)$$

It is important to note that when a sample is placed in the ellipsometer, there are two different sets of angles (P_1, A_1) and (P_2, A_2) that can be determined by the measurement procedure. Either A_1 or A_2 will have a negative tangent (Case (A)) and the other will have a positive tangent (Case (B)). The test shown in Eq. (3.15) is used to identify which angle set is Case (A) and which is Case (B). The angles ψ and Δ obtained from Eq. (3.14) and the appropriate choice of Eq. (3.11) or Eq. (3.12) are exactly the same

$$\begin{aligned} \psi_{(A)} &= \psi_{(B)} \\ \Delta_{(A)} &= \Delta_{(B)} \end{aligned} \quad (3.20)$$

in the absence of experimental errors. The use of both angle sets

(P_1, A_1) and (P_2, A_2) allows, therefore, an experimental cross check. Both sets were measured and used in the experimental work described in the following sections. In the next section an error analysis and sensitivity study for ellipsometric data are described.

SECTION IV

AN ERROR ANALYSIS AND SENSITIVITY STUDY FOR ELLIPSOMETRIC PARAMETERS

When using the ellipsometric measurements of ψ and Δ to examine a film or substrate, it is important to have some idea of how much error ψ and Δ contain. Also, since both the real and imaginary part of the refractive index for both the substrate and film, as well as the film thickness (denoted by t in this and the following sections) are dependent upon ψ and Δ , it is useful to know how much error in these quantities will result from errors in ψ and Δ .

To examine the errors in ψ and Δ , the equipment used in making the measurements must be examined. A Gaertner L-119 ellipsometer was used for the measurements made for this study. This instrument has two arms, the collimator and the telescope, both with verticle circles holding polarizers which can be read to an accuracy of 0.01° and with a clamp and tangent screw for setting. Mounted on a third circle is a Soleil Babinet Compensator which can be adjusted for use as a quarter wave plate. Centered between the two arms of the ellipsometer is a sample table which can be rotated and adjusted in height. The collimator arm is fixed and the telescope arm rotates on the same axis as the sample table. The two arms have height and level adjustments for alignment. The angle, $2\theta_i$, between the two arms can be read from a dial to 20 seconds of arc.

A prototype detector from Newport Research Corporation was used in making the measurements. This instrument is sensitive to light intensities ranging from 10^{-7} to 10^{-1} watts. The light source was a He-Ne

laser operating at a wavelength of $6328\overset{\circ}{\text{\AA}}$. This laser was made by C. W. Radiation, model S-203H, and has a maximum output of 10^{-3} watts.

The alignment of the arms was made so that light through the collimator could pass straight through (no reflection) into the telescope arm and out a pinhole exit. A high quality mirror surface was then used to insure that the alignment was also correct for reflection into the telescope arm for all values of θ_i , the mirror surface first being tested to insure that it was perpendicular by reflecting the light beam back on itself from both sides of the mirror.

The alignment of the polarizers was done next. When light shines at the Brewster angle on a piece of optically flat glass of index n , the reflected light is perpendicular to the plane of incidence. At this angle, described by $\theta_i = \theta_B$:

$$\tan\theta_B = n, \quad (4.1)$$

the reflected and transmitted waves are at right angles to each other and the reflected wave does not receive any energy for oscillations in the plane of incidence. By using this property of the Brewster angle, the analyzer, fixed on the telescope arm, will extinguish the light when it is oriented horizontally ($A = 0$). The alignment of the analyzer can be accomplished by adjusting the calibrated circle to read $A = 0.00$ when the light is extinguished. The polarizer on the collimator arm can now be adjusted using the aligned analyzer to make adjustments. For this adjustment the arms of the ellipsometer are placed so the light shines straight through and there is no reflection.

The polarizer angle, P , is set equal to 0.00° when the analyzer angle, A , is set to 90.0° and the light is extinguished.

Once the angles of the analyzer and polarizer are set, the amount of error in the alignment can be determined. First, without any sample to reflect the light, the angle A is set and the angle P found which extinguishes the light to the detector. The error, ϵ , between the setting of the two polarizers can be defined by the relation:

$$P = A + 90^\circ + \epsilon \quad (4.2)$$

For the alignment of the ellipsometer used, this error was determined to be $\epsilon = 0.03^\circ$. This relation is plotted as Curve 1 in Fig. (4.1).

A mirror surface was then used to reflect the light to the analyzer. The angle A was set at various angles in the neighborhood of 0.0° and for each value of A the angle P was found which extinguished the light. For P equal to exactly 90° and for A equal to exactly 0° , the error due to any phase change upon reflection would be zero because there would be no horizontal component. At angles close to these values ($\pm 0.2^\circ$) the amplitude of the horizontal component is still very small (0.35%) compared to the vertical component and, therefore, any phase change would be negligible. The data from these measurements is also plotted on Fig. (4.1). Curve 2 on this figure is a straight line least squares fit to this data. The intersection of the two curves locates the readings of A and P which actually correspond to 0.0° and 90.0° , respectively. The corrections for A and P so determined were:

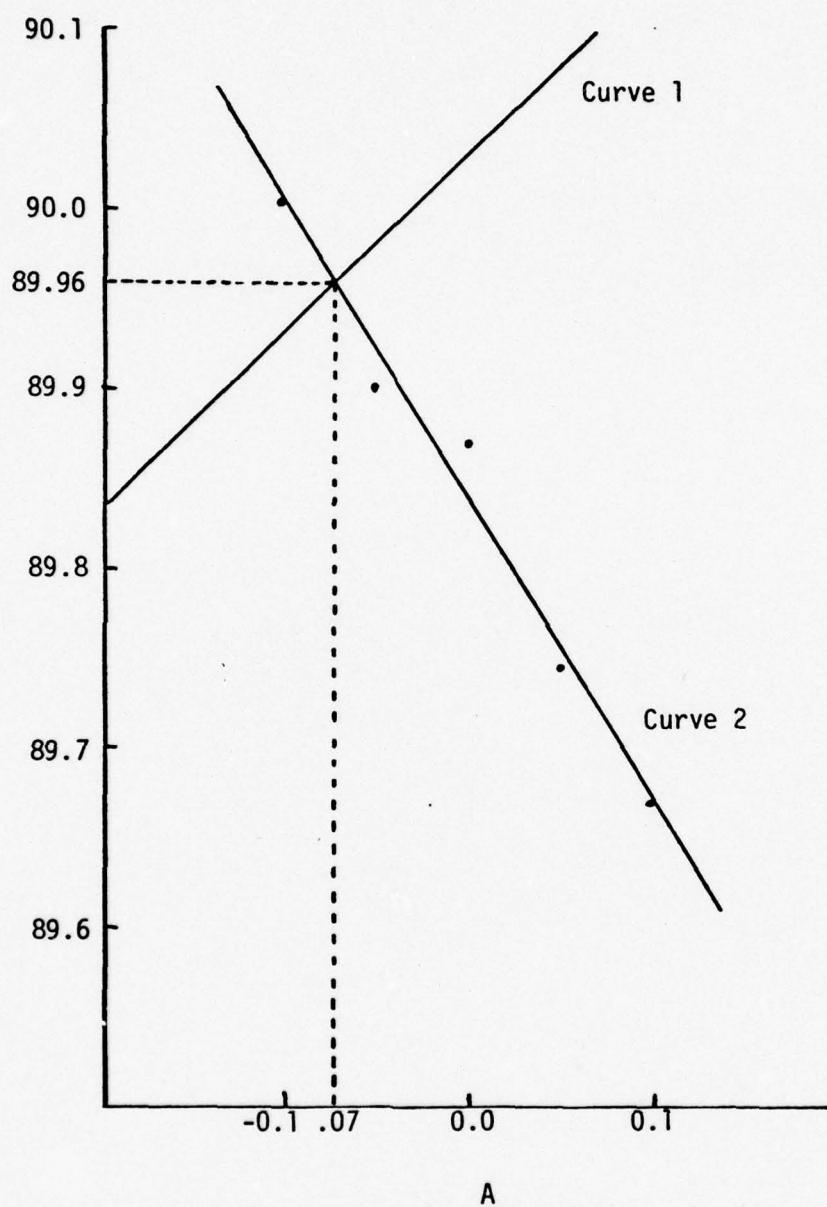


Fig. 4.1 Calibration Curves for the Polarizers

$$\begin{aligned}
 A_c &= A + \Delta A, & \Delta A &= -0.07^\circ \\
 P_c &= P + \Delta P, & \Delta P &= -.04^\circ
 \end{aligned}
 \tag{4.3}$$

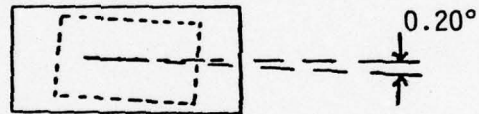
The corrected angles are used in calculating ψ and Δ and all further references to A and P will refer to the corrected angles, A_c and P_c .

After the polarizers were both aligned, the quarter wave plate was inserted and aligned. The quarter wave plate used is a Soliel Babinet Compensator. This compensator can be varied in thickness so it can be used as a quarter wave plate over a wide range of frequencies. The quartz used as the retarder in the wave plate is actually in two pieces. The outer edges are parallel but the cut between the two pieces is diagonal. The thickness of the quartz can be varied by sliding the two pieces of quartz along each other. Fig. (4.2a) shows the alignment of the quartz pieces. To adjust the wave plate in the ellipsometer, the fast axis of the compensator was first set to an angle of $\alpha = 45.0^\circ$. To do this, the analyzer was set to 45.00° and the polarizer was set to 135.00° . With the fast axis of the compensator at an angle of approximately 45° , the angle was adjusted for the light to the detector to be at a minimum. At this point the fast axis scale was set to read 45.00° .

With the angle scale set for the quarter wave plate, the thickness or phase delay, β , was tuned for a delay of 90° . Leaving the fast axis at 45° , the polarizer was set at 0.00° and the analyzer at 90.00° , the light to the detector was then minimized by changing the thickness. The thickness of the quartz was varied over a wide range, giving six



a.



b.

Fig. 4.2 The Two Pieces of the Compensator Showing
a) the Direction of Movement for Adjustment
of Thickness
b) the Alignment Error in the Axis

readings for which the light was at a minimum. At these points the amounts of delay due to the thickness is an odd multiple of 180° . The dial which adjusts the quartz thickness is calibrated in dimensionless steps of 0.01 and the spacing between the minimum readings is 6.24. Assuming the dial to be linear, the reading for a delay of $\pm 90^\circ$ could be calculated by adding 1.56 to any of the readings taken. An error of 0.07 on the dial would cause an error of 1.0° in the delay.

The accuracy of the alignment of the compensator can be checked in several ways. With the thickness set for a 90° delay and the fast axis set at 45° , if the polarizer is set at 0.00° the light passing through the analyzer to the detector should be at the same intensity for all settings of the angle A. In this case the light leaving the wave plate is circularly polarized. The alignment of the fast axis can also be checked by setting both the polarizer and the compensator to 45.00° , setting the analyzer to 135.00° and changing the thickness of the quartz. If all three elements are aligned there should be no change in the nulled intensity of the light to the detector. For this particular compensator, however, the two pieces of quartz were slightly misaligned. The fast axis of the two pieces formed an angle of approximately 0.20° , see Fig. (4.2b). This could be shown by leaving the compensator at 45.0° , setting the polarizer at 135.00° , and adjusting the analyzer to minimize the light to the detector. The angle A was at 45.09° and the amount of error was $+0.09^\circ$ from the theoretical angle of 45.00° . Angle A was then reset to 45.00° and the angle P was adjusted so that a minimum intensity was detected. The angle measured was 134.89° so

that the amount of error was -0.11° . The conclusion was that the first piece of the compensator is at an angle of 44.89° and the second piece is at an angle of 45.09° giving the difference between the two pieces as 0.20° .

To find the amount of error this will cause in the calculations of ψ and Δ , some theoretical calculations were made. A computer program written by F. L. McCracken[5] from the National Bureau of Standards was used in calculations for error analysis as well as in determining ψ and Δ from measurements of the angles A and P. Theoretical values of A and P were determined for a film index of ($n_f = 1.766$, $K_f = 0$) and a substrate index of ($n_s = 1.21$ and $K_s = 5.72$), and film thickness varying from 0 to 600\AA in increments of 100\AA . Using these values for A and P, the values of ψ and Δ were calculated for compensator angles, α , of 44.95° , 45.0° and 45.05° . To check the errors in ψ and Δ due to an error in the delay of the wave plate of 0.5° , calculations were also done using a compensator angle of 45.0° but using the values of 89.5° , 90.0° , and 90.5° for β . The results of these calculations are shown in Tables (4.1) through (4.4). Since two sets, (P_1 , A_1) and (P_2 , A_2), can be found for each ψ and Δ , both sets were used. The averages of the two values obtained for ψ and Δ were also calculated and denoted by the subscript 'avg'. A computer sensitivity study showed that ψ_{avg} , corresponding to errors in α by either $+0.05^\circ$ or -0.05° , agreed with the value of ψ obtained with no error in α . These results are shown in Table (4.1) and illustrate the value of using ψ_{avg} . For an error in β of $\pm 0.5^\circ$ the average was only a little worse giving an error in the

TABLE 4.1
EFFECTS OF ALIGNMENT ERRORS FROM THE WAVE PLATE ANGLE ON ψ

Thickness $\frac{\circ}{A}$	$\alpha = 45.05^\circ$				$\alpha = 44.05^\circ$				$\alpha = 45^\circ$	
	ψ_1	ψ_2	ψ_{avg}	ψ_1	ψ_2	ψ_{avg}	ψ_{base}			
0	41.912	41.786	41.849	41.836	41.862	41.849	41.849			41.849
100	42.229	42.175	42.202	42.175	42.229	42.202	42.202			42.202
200	42.597	42.565	42.581	42.565	42.597	42.581	42.581			42.581
300	42.987	42.975	42.981	42.975	42.987	42.981	42.981			42.981
400	43.407	43.411	43.409	43.411	43.407	43.409	43.409			43.409
500	43.909	43.923	43.916	43.923	43.909	43.916	43.916			43.916
600	44.629	44.645	44.637	44.645	44.629	44.637	44.637			44.637

TABLE 4.2
EFFECTS OF ALIGNMENT ERRORS ON ψ DUE TO WAVE PLATE DELAY

Thickness \AA	$\psi = 90.5^\circ$				$\psi = 89.5^\circ$				$\psi = 90^\circ$
	ψ_1	ψ_2	ψ_{avg}	ψ_1	ψ_2	ψ_{avg}	ψ_1	ψ_2	ψ_{base}
0	41.716	42.033	41.874	42.033	41.716	41.874	41.874	41.874	41.874
100	41.994	42.410	42.203	42.410	41.994	42.203	42.203	42.203	42.202
200	42.345	42.817	42.582	42.817	42.345	42.582	42.582	42.582	42.581
300	42.733	43.229	42.982	43.229	42.733	42.982	42.982	42.982	42.981
400	43.160	43.658	43.410	43.658	43.160	43.410	43.410	43.410	43.409
500	43.669	43.163	43.917	44.163	43.669	43.917	43.917	43.917	43.916
600	44.390	44.884	44.638	44.884	44.390	44.638	44.638	44.638	44.637

TABLE 4.3
EFFECTS OF ALIGNMENT ERRORS ON Δ FROM THE WAVE PLATE ANGLE

Thickness Å	$\theta = 45.05^\circ$			$\theta = 44.95^\circ$			$\theta = 45^\circ$
	Δ_1	Δ_2	Δ_{avg}	Δ_1	Δ_2	Δ_{avg}	
0	140.466	140.466	140.466	140.266	140.266	140.266	140.366
100	123.440	123.440	123.440	123.240	123.240	123.240	123.343
200	108.760	108.760	108.760	108.560	108.560	108.560	108.663
300	96.710	96.710	96.710	96.510	96.510	96.510	96.610
400	87.548	87.548	87.548	87.348	87.348	87.348	87.449
500	81.820	81.820	81.820	81.620	81.620	81.620	81.719
600	80.820	80.820	80.820	80.620	80.620	80.620	80.714

TABLE 4.4
EFFECTS OF ALIGNMENT ERRORS ON Δ DUE TO WAVE PLATE DELAY

Thickness Δ	$\beta = 90.5^\circ$				$\beta = 89.5^\circ$				$\beta = 90^\circ$	
	Δ_1	Δ_1	Δ_{avg}	Δ_1	Δ_2	Δ_{avg}	Δ_1	Δ_2	Δ_{avg}	Δ_{base}
0	140.367	140.367	140.367	140.367	140.367	140.367	140.367	140.367	140.367	140.366
100	123.341	123.341	123.341	123.341	123.341	123.341	123.341	123.341	123.341	123.343
200	108.661	108.661	108.661	108.661	108.661	108.661	108.661	108.661	108.661	108.663
300	96.610	96.610	96.610	96.610	96.610	96.610	96.610	96.610	96.610	96.610
400	87.448	87.448	87.448	87.448	87.448	87.448	87.448	87.448	87.448	87.449
500	87.720	81.720	81.720	81.720	81.720	81.720	81.720	81.720	81.720	81.719
600	80.720	80.720	80.720	80.720	80.720	80.720	80.720	80.720	80.720	80.714

third decimal place as shown in Table (4.2).

For Δ , however, the errors were more pronounced. An error in α of $\pm 0.05^\circ$ gives an error of $\pm 0.1^\circ$ for Δ_{avg} , and an error of $\pm .5^\circ$ in β gives an error of up to $.006^\circ$ for Δ_{avg} . These results are illustrated in Tables (4.3) and (4.4).

The slight misalignment of the quartz pieces in the compensator, mentioned above, produced the ambiguity: $\alpha = 44.89^\circ$, but also $\alpha = 45.09^\circ$. The angle 44.89° was used in the computer code for analysis of the data. Additional checks showed that the 0.20° discrepancy would produce negligible errors in ψ_{avg} .

The errors produced in ψ and Δ by errors in A and P can be expressed simply since

$$\psi = A' \text{ or } \pi + A'$$

for Case (B)

$$\Delta = -2P' - 90^\circ$$

and

$$\psi = -A \text{ or } \pi - A$$

for Case (A)

$$\Delta = -2P + 90^\circ$$

If the amount of error in the angle A is ϵ , then the error in ψ would be ϵ if a single value of A were used. But if two values of A were found, say, one corresponding to A between 0° and 90° , and the other for A between -90° and 0° then the error is reduced because some sources of error give cancelling effects. For example, an error in the

zero position of the scale for A will cancel

$$\psi_{\text{avg}} = \frac{(A' + \epsilon) + |-A + \epsilon|}{2} = A'.$$

Unfortunately, an error in the zero position of the scale for P does not average out for errors in Δ_{avg} . If the error in P is δ , the amount of error in Δ can be calculated by

$$\Delta_{\text{avg}} = \frac{\{-2(P' + \delta) - 90^\circ\} + \{-2(P + \delta) + 90^\circ\}}{2}$$

$$\Delta_{\text{avg}} = \frac{\Delta - 2\delta + \Delta' - 2\delta}{2} = \Delta - 2\delta.$$

The error in Δ and in Δ_{avg} is double that in the measurement of P or P'.

Another and more critical source of error arises from the method in which the sample is aligned in the ellipsometer. Although the calculations determining the values of ψ and Δ from angles A and P do not depend on the angle of incidence, the use of ψ and Δ in determining the values of the film thickness or the index of refraction is dependant on this angle. A small angle of incidence error can cause large errors in ψ and Δ . The placement of the sample is critical because an error of 5mm from the center of the table can create an error of 0.5° in the angle of incidence, θ_i . Fig. (4.3) shows the values of ψ and Δ for a film with thickness varying from 0\AA to 200\AA . The film index is again taken to be ($n_f = 1.76$, $K = 0$) and the substrate index is $\tilde{n}_s = 1.21(1 + j5.72)$.

Because this source of error was recognized as the quantity which would most likely limit the resolution of the ellipsometer, a systematic

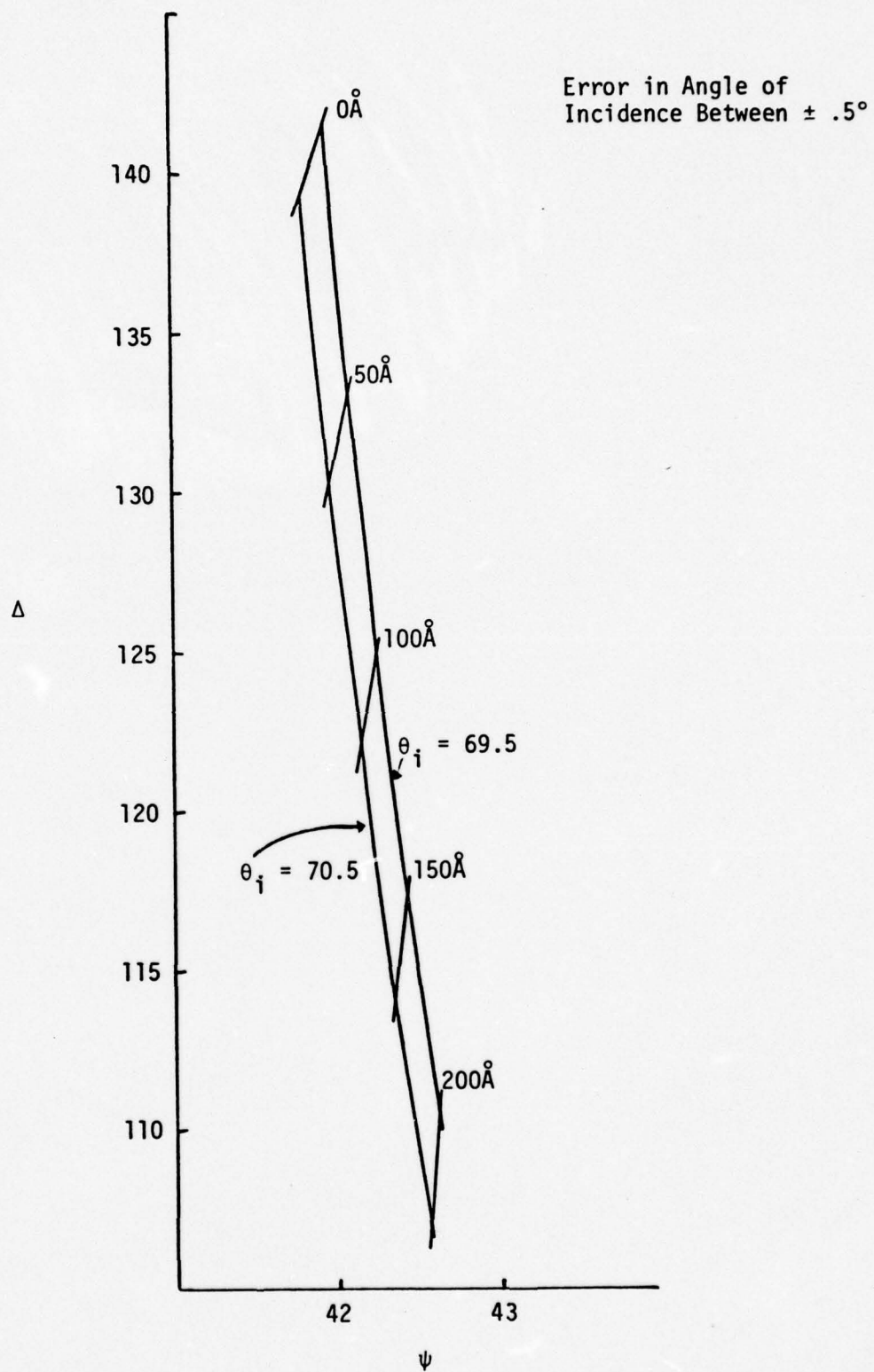


Fig. 4.3 Sensitivity Curve for Error in θ_i

procedure for aligning each sample was used. Pinholes on each end of the telescope tube were carefully aligned. If a sample were carefully placed at the center of the sample table, the reading on the scale for $(2\theta_i)$ would be accurate to ± 20 sec of arc. The light would then pass through the center of the pinholes. For a misaligned sample, the light would not pass straight through the telescope tube, but would be inclined by an amount $\delta\theta$ as indicated in Fig. (4.4). The maximum angle of error can be defined by the diameter of the pinhole (.2cm) and the length of the telescope tube (28cm).

$$\delta\theta_{\max} = \tan^{-1} \left(\frac{.2\text{cm}}{28\text{cm}} \right) = 0.4^\circ$$

The error in the angle of incidence is half this value giving a possible error of $\pm 0.2^\circ$. The alignment of a sample was always checked in two configurations as shown in Fig. (4.4). This procedure served as a partial double check on the pinhole alignment, also, because the check in two configurations would be impossible if the pinholes are not well aligned.

An added benefit from using this method to align the sample, is that the sample tilt is also checked. The sample cannot pass this test if it leans forward or backward more than 0.2° . This tilt can cause an error in ψ for the two sets of measurements, but for ψ_{avg} the error is negligible. The tilt angle also causes an error of less than $.01^\circ$ in Δ_{avg} .

Another source of error, that due to the transmission properties of the wave plate, has also been examined. A transmission difference

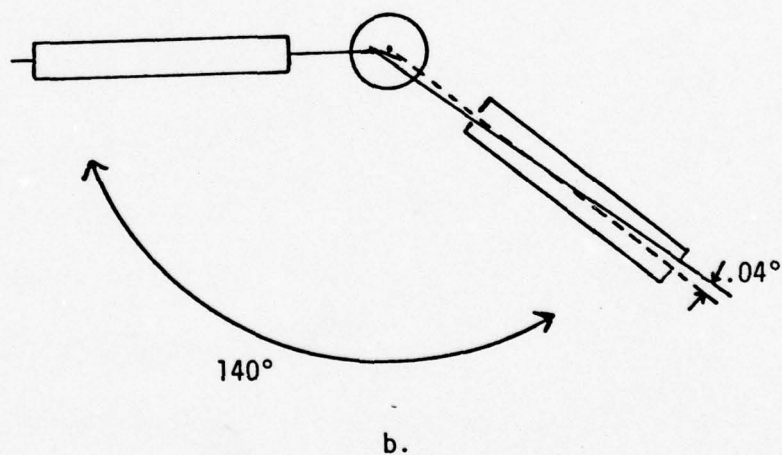
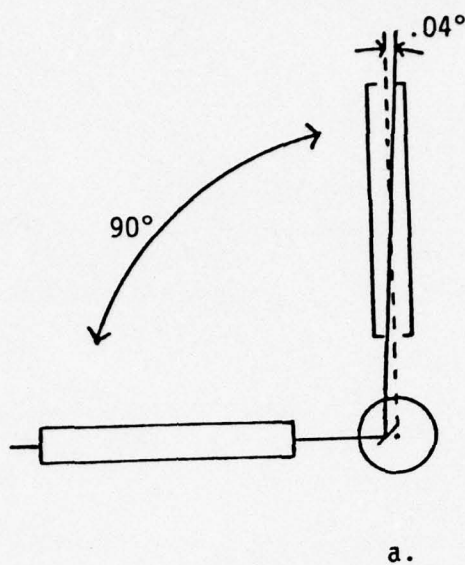


Fig. 4.4 The Two Configurations for Alignment of the Sample in the Ellipsometer Showing the Maximum Error Possible

of 5% between the fast and slow axes would cause large discrepancies in Δ (about 5°) between the two sets of measurements at each point. The average of these two measurements gives a very small error of 0.03° in Δ_{avg} . The error in ψ_{avg} is also about 0.03° . Since the maximum discrepancy in the sets of measurements actually taken was 0.66° for Δ_{avg} and $.57^\circ$ for ψ_{avg} , any error due to the transmission properties of the wave plate would have to be negligible.

The conclusion drawn from this study of errors is that the error in the angle of incidence has the largest effect. The angle of incidence is correct to the accuracy of $\pm 0.2^\circ$ and the effect of this error on values of ψ or Δ must be examined for the particular set of values given for the film and substrate properties to determine expected error bounds.

The precision of the measurements can be estimated by examining the data. Two sets of measurements, (P_1, A_1) and (P_2, A_2) , were used to obtain the values of Δ_{avg} and ψ_{avg} . At each point on the sample, the numbers Δ_1 , Δ_2 , and Δ_{avg} were determined. The maximum discrepancy in Δ was 0.66° and the average discrepancy was 0.21° . Thus the average precision of the procedure for Δ was $\pm 0.11^\circ$ to $\pm 0.33^\circ$. The maximum discrepancy in ψ was 0.57° and the average discrepancy was 0.18° . Thus the average precision of the procedure for ψ was $\pm 0.09^\circ$ to $\pm 0.29^\circ$.

Once some idea is formed concerning the amount of error in ψ and Δ , it is necessary to relate this error to the error produced in the index of refraction and in the film thickness. This is done by use of curves of constant index and thickness plotted against the values of ψ and Δ .

The simplest case to study is that of a bare substrate, since there are only two media parameters determined by ψ and Δ . These two variables are the real part, n_s and the imaginary part, K_s , of the index of refraction, where

$$\tilde{n} = n_s (1 + iK_s) \quad .$$

Fig. (4.5) shows curves of constant n_s and K_s on a ψ and Δ plot. It should be noted that for $K_s = 0$, there is no phase change upon reflection and Δ has a value of 0. As the imaginary part of the index increases the phase between the reflected parallel and perpendicular components increases and, thus, the value of Δ increases.

Fig. (4.6) shows the theoretical values of ψ and Δ for a film of $n_f = 1.6$, $K_f = 0$ on a substrate of $n_s = 1.21$ with no absorption. The thickness varies from 0 to 2700\AA . At a thickness of 2381\AA the curve closes and starts repeating, this happens because the film thickness produces in a phase shift of 360° at this point. For a film with no absorption the amplitude and phase would be the same at the surface for a phase shift of any number of complete cycles. The thickness of any film to cause a full 360° phase shift can be calculated as:

$$t_c = \frac{\lambda_0}{2n \cos \{\arcsin (\sin \theta_i / n)\}} = \frac{\lambda_0}{2 \sqrt{n_1^2 - \sin^2 \theta_i}} \quad .$$

This thickness is a function of the wavelength of the light λ_0 , the film index n , and the angle of incidence θ_i .

Fig. (4.7) shows a family of curves generated by varying the film thickness, t . These curves are for the film index, n_f , varying from

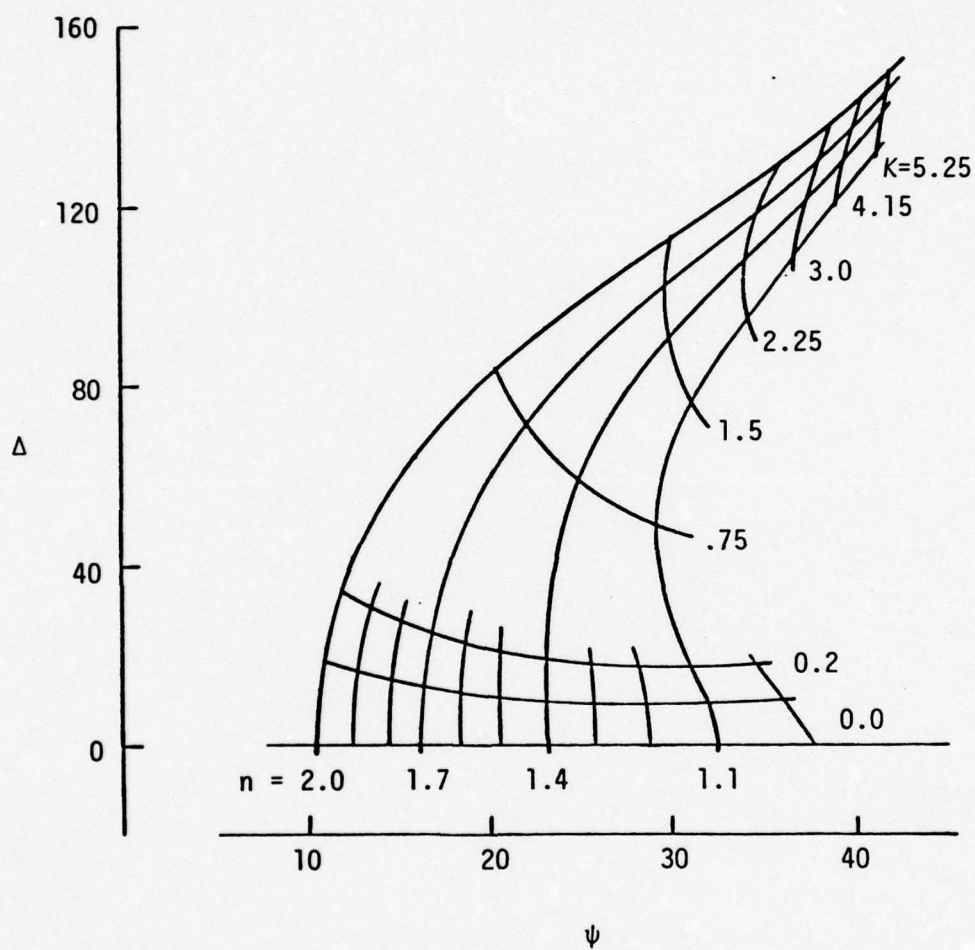


Fig. 4.5 Curves of Constant n_s and Curves of Constant K_s for bare Substrates

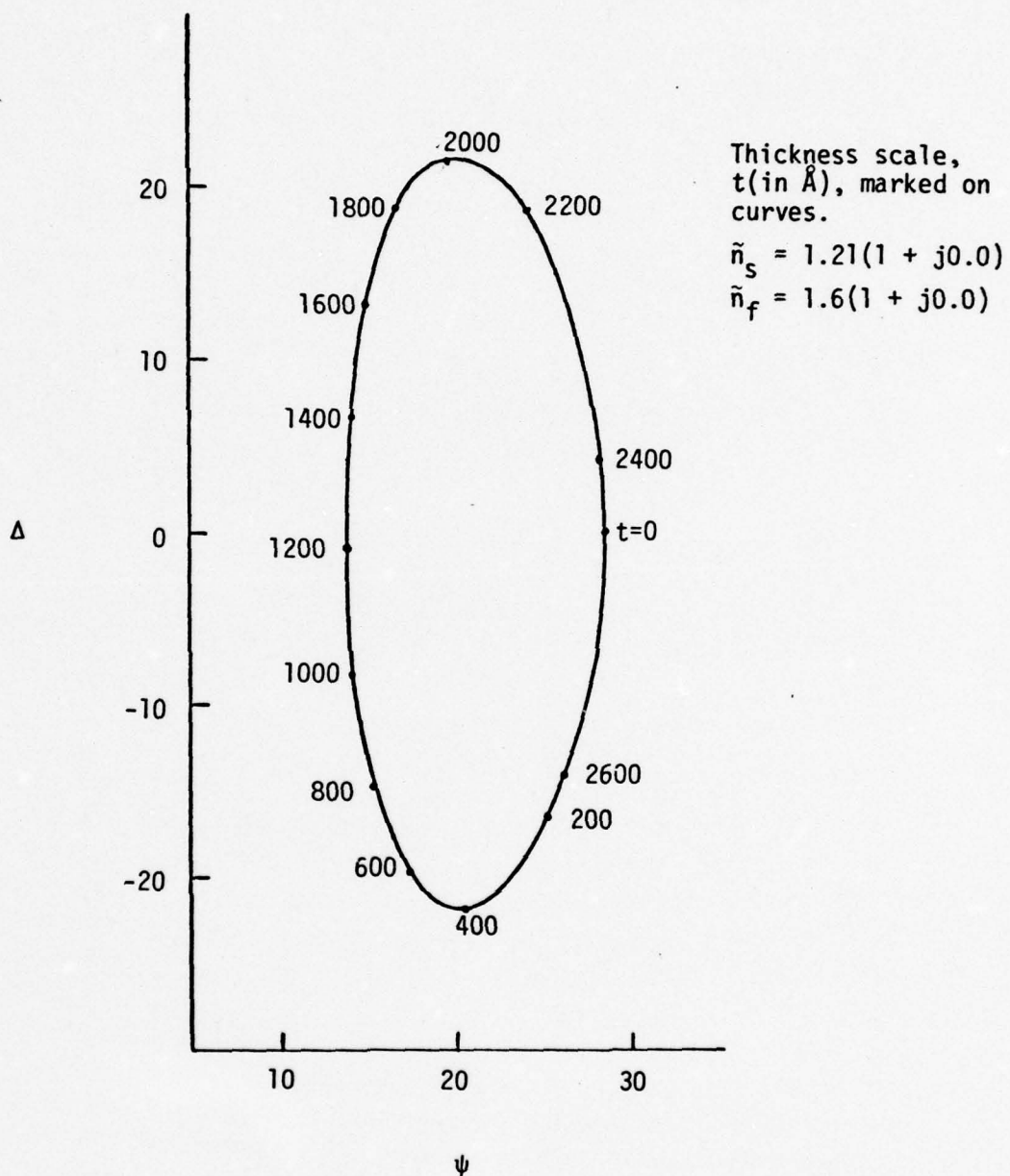


Fig. 4.6 A Thickness Curve: Variation in Δ and ψ
 Due to Changes in Film Thickness

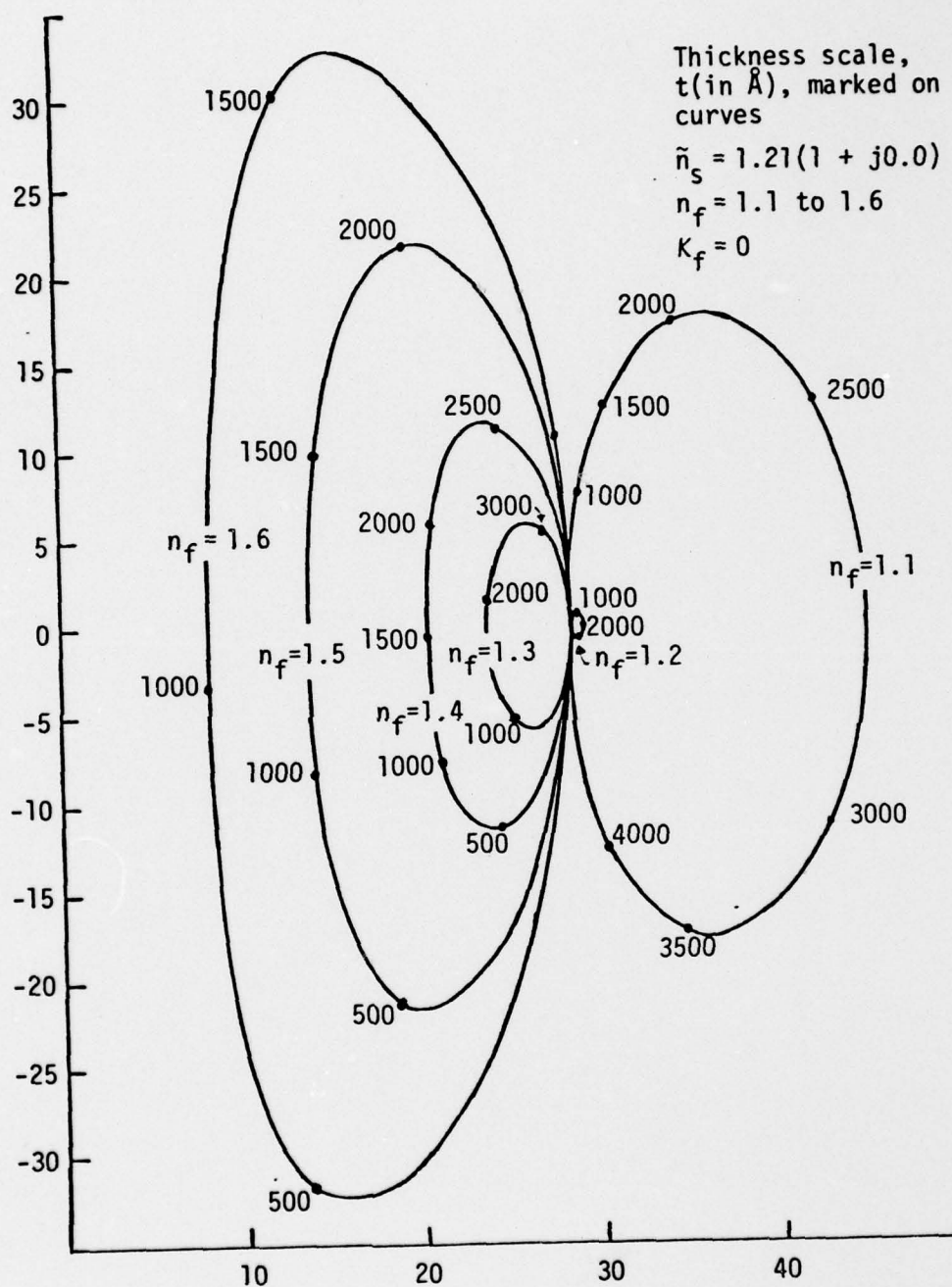


Fig. 4.7 Variation in Thickness Curves
as n_f Varies from 1.1 to 1.6

1.1 to 1.8. The substrate is the same as in the previous figure. It can be noted that as the film index approaches the substrate index the curve formed becomes smaller and at the point where $n_f = n_s$ only a single point is found. This point can be compared to a point with the same ψ and Δ in Fig. (4.5), and it can be noted that this is the value for a bare substrate with that index.

Using a film index of $n_f = 1.766$ and the real part of the substrate index to be $n_s = 1.21$, the imaginary part of the substrate K_s was increased from 0.0 to 5.72. Fig. (4.8) shows thickness curves corresponding to this range of K_s . All of the thickness curves are cyclic. The zero thickness trajectory as a function of K_s is traced by the dotted curve.

Since the material used in this study has a substrate of aluminum, Fig. (4.9) shows a family of curves with the film index changing from 1.1 to 1.8 on a substrate of $n_s = 1.21$ and $K_s = 5.72$, values similar to aluminum.

Fig. (4.10) shows the change in the curves. As the real part of the substrate index, n_s , is varied from 1.0 to 2.0. The imaginary part of the substrate index, $K_s = 5.72$, and the film index, $n_f = 1.766$, are constant. Using Figs. (4.8) and (4.10), it can be seen that a small error in the values assumed for real and imaginary part of the substrate index will not cause a large shift in the values determined for the film index and thickness.

When the film over the substrate becomes absorptive, the curves are no longer cyclic. Fig. (4.11) shows the curves formed by varying

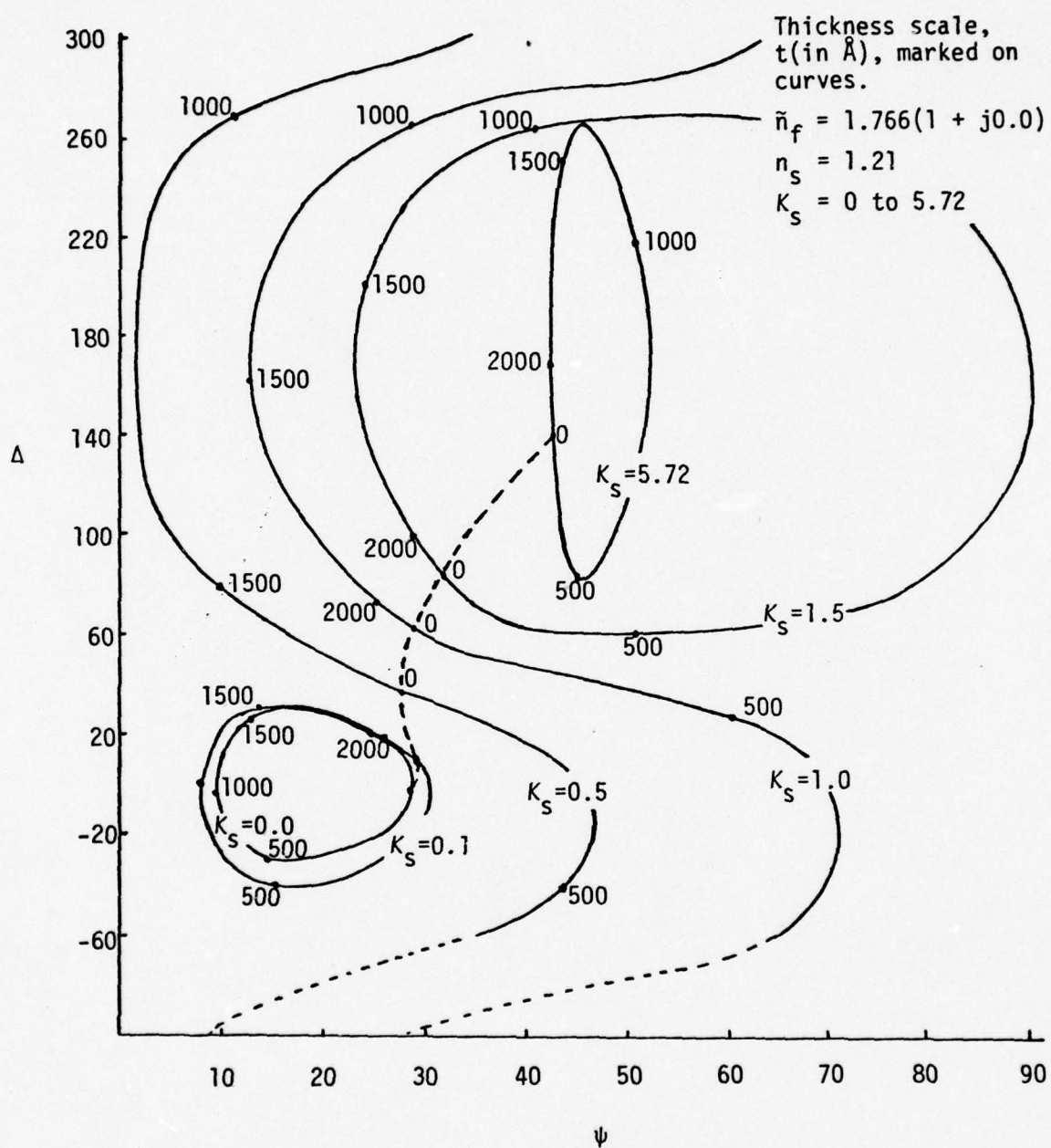


Fig. 4.8 Variation in Thickness Curves as K_s Increases from 0.0 to 5.72.

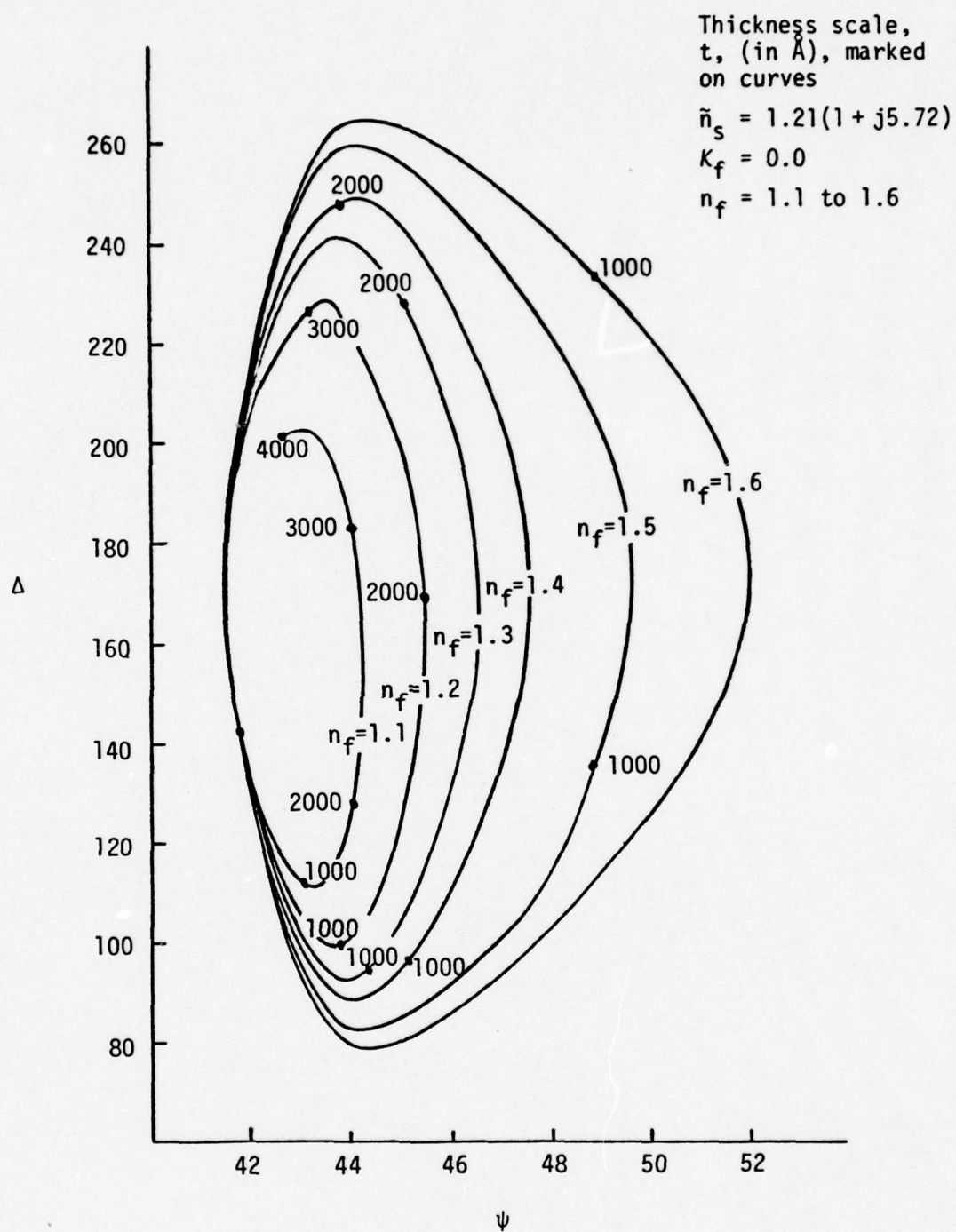


Fig. 4.9 Variation in Thickness Curve as n_f Varies from 1.1 to 1.6 for Large K_s

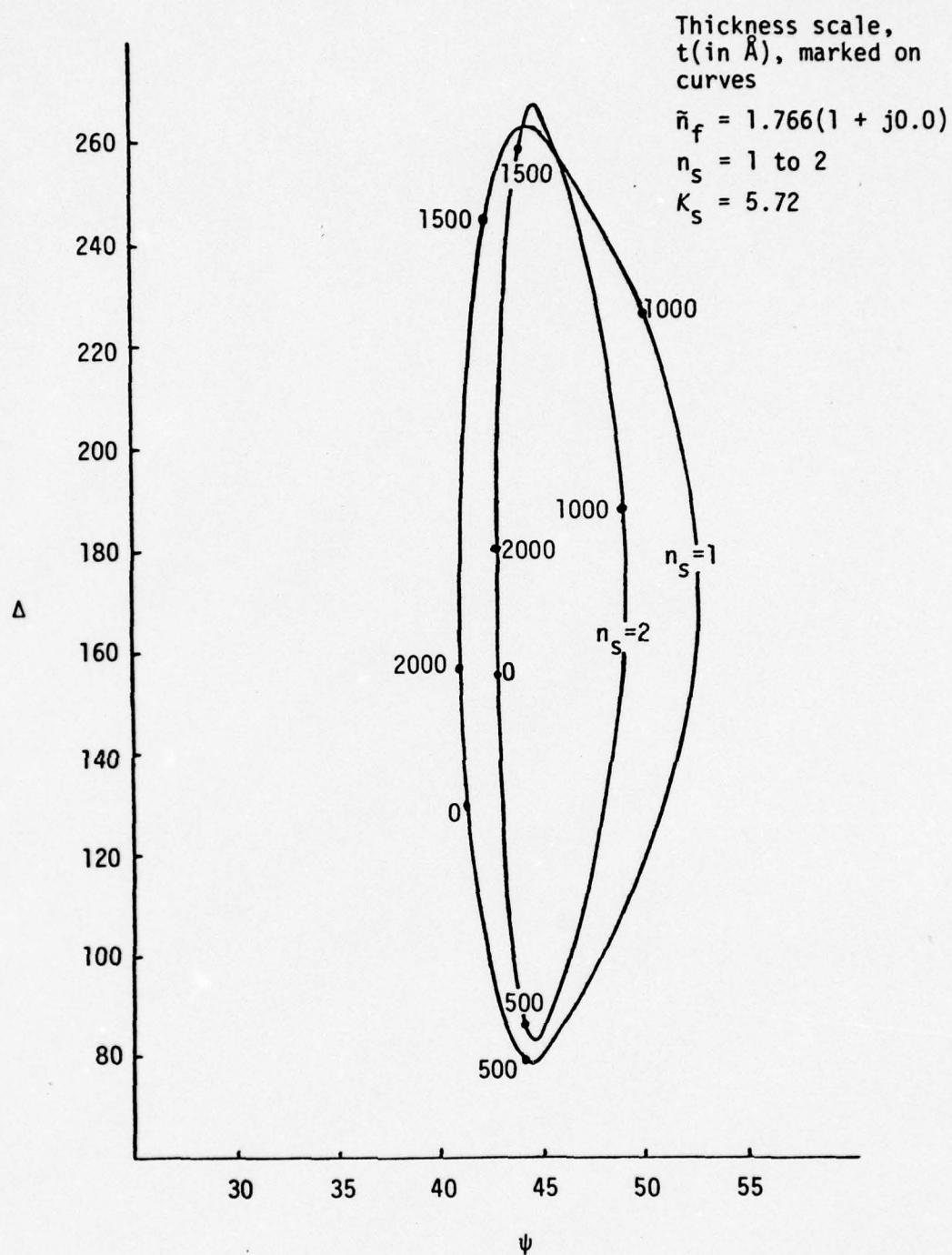


Fig. 4.10 Variation in Thickness Curves for a Change in n_s

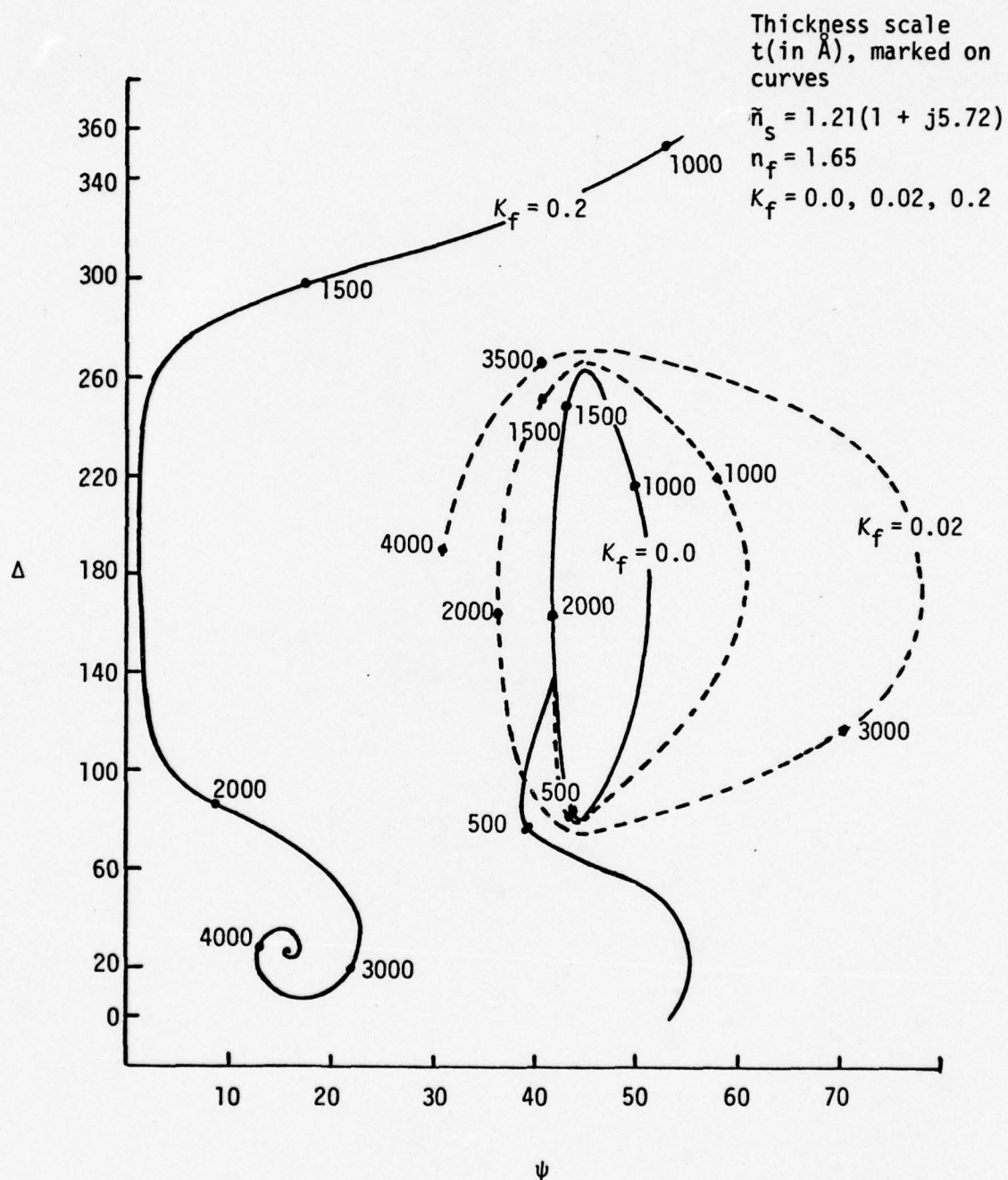


Fig. 4.11 Variation in Thickness Curves as K_f Varies from 0 to .2

the thickness of the film on a substrate of aluminum. The real part of the film, $n_f = 1.76$, is constant, but the imaginary part, K_f , is considered for the three values: 0.0, 0.02, and 0.2. The curve formed with $K_f = 0.2$ is shown as the thickness gets large. As this happens, enough light is absorbed that the reflected light sees only the film and the values of ψ and Δ approach those for a substrate with the index of the film. This point can be compared with the substrate value in the enlarged view in Fig. (4.12).

Since the curves formed from a smaller imaginary value, $K_f = 0.02$, do not change as fast as for $K_f = 0.2$, they were not plotted for larger values of the thickness. At a much thicker film, these curves also approach the ψ and Δ values of a substrate with the index of the film.

Now that the various sources of error and parameter sensitivities have been explored, the general description of the research tool used in this study is complete. In the next section, the use of ellipsometry for the study of oxide films on pure aluminum will be described. Because such films have certain unpleasant properties, certain strategies must be developed in order to gain useful results from ellipsometry. The strategies of the method are generalized even more in Section VI in an attempt to use ellipsometry to study oxide layers on Alclad.

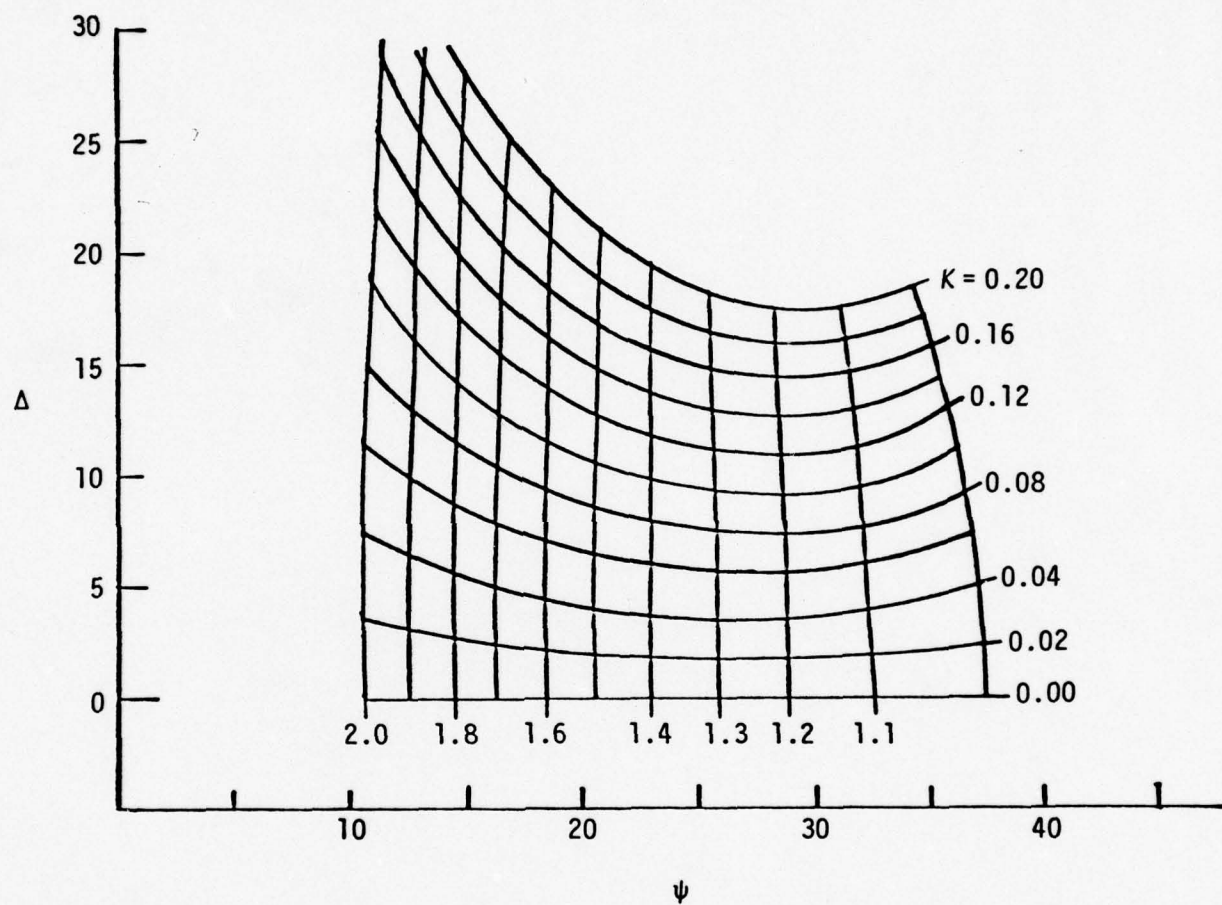


Fig. 4.12 Enlarged View for the Changes in n_s and K_s for a Bare Substrate

SECTION V

A STUDY OF OXIDE FILMS ON PURE ALUMINUM

In order to attempt to develop a method for measuring the thickness of oxide films on the rough surfaces of alclad materials, oxide films were studied first on optically flat surfaces of pure aluminum. Samples of optically flat fused silica covered with an evaporated film of 99.999% pure aluminum were used for this study. In air an oxide film grows very fast on a bare aluminum surface. R. W. Fane and W. E. J. Neal[6] have monitored changes of Δ over a period of 100 hours. The results are given in Fig. 5.1 and show a linear relationship between the change in Δ and the log of time. A change in the value of Δ by 100 minutes corresponds approximately to a 12\AA change in thickness. They also determined that the final thickness of the oxide film was between 40 and 55\AA depending on the initial state of oxidation, time of exposure, and humidity.

J. H. Halford, F. K. Chin, and J. E. Norman[7] state that this oxide layer grows slowly in a vacuum, but accelerates when exposed to air. They estimate the asymptotic thickness to lie between 40 and 50\AA . Exposure of the oxide layer to O_2 or moist O_2 accelerates the growth.

M. J. Digman [8] studied the oxide growth at the elevated temperatures of 250° , 350° and 450°C . The films were heated and at intervals the barrier voltage was measured. The barrier voltage is proportional to the oxide thickness. Table 5.1 shows the results. The lowest temperature, 250°C , produced a small change over a 600 hour

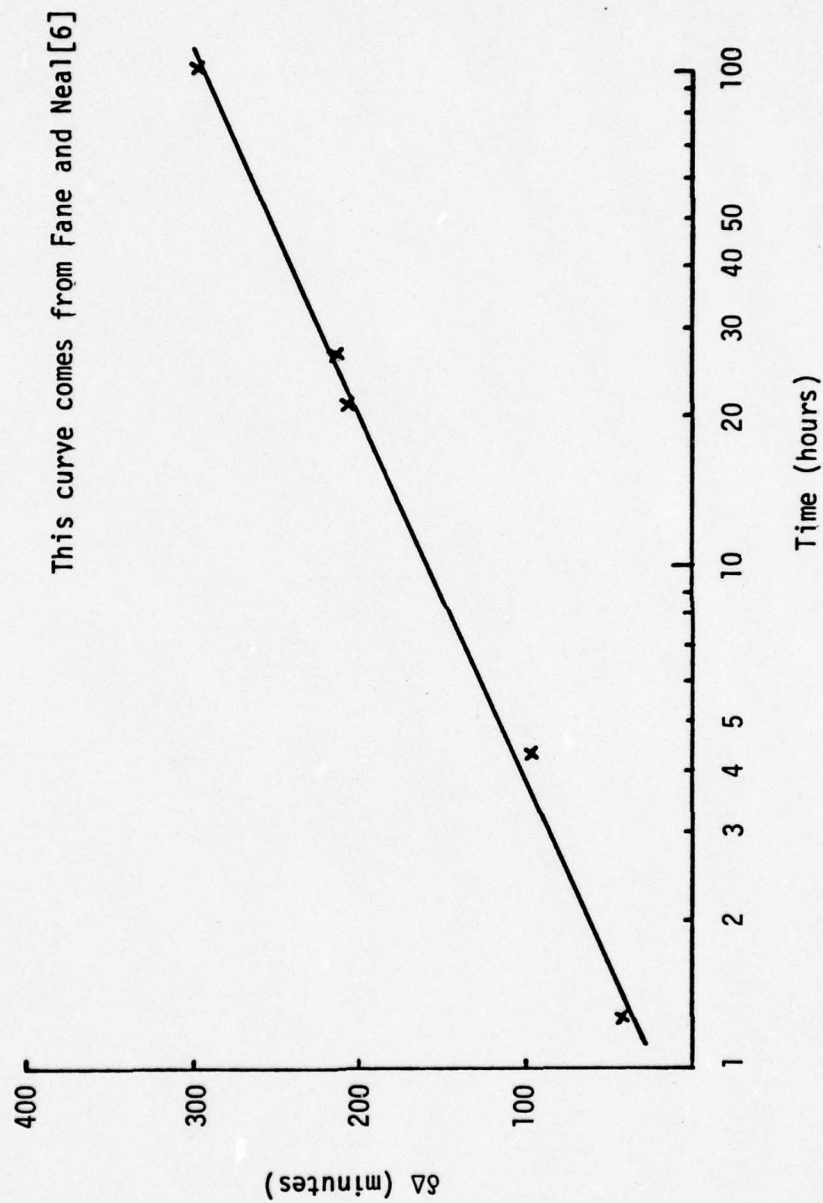


Fig. 5.1 Oxidation Rate Δ Shifts vs. Log(time)

TABLE 5.1
RELATIONSHIP OF HEATING TEMPERATURE AND TIME
AS RELATED TO THE BARRIER VOLTAGE

Oxidation Temp.	Time, Hr (per cent)	Barrier Voltage
450°C	0.0667	1.78
	0.25	2.20
	1.0	2.47
	4	3.29
	16	3.66
	24	2.89
350°C	1.0	1.70
	4	2.04
	16	.234
	64	2.83
	256	3.36
250°C	1.0	1.33
	5	1.62
	24	1.75
	120	2.02
	600	2.37

This data was taken from Dignam[8]

period, while for the higher temperatures the change over smaller periods was greater. At 450°C after 24 hours there is a sudden decrease in the barrier voltage. This is due to a change in the oxide structure. Films formed on aluminum below 500°C are either amorphous material or material composed of extremely small crystals. At higher temperatures gamma alumina crystallites are formed. No evidence of the crystallites were found for oxidation periods up to 256 hours at 350°C. Digman also studied samples anodically oxidized and annealed at 450°C and found them to have the same conduction properties as the samples with the oxide grown in the 250° to 450°C range. He concluded that the film structures were apparently the same. The oxide film formed on aluminum is transparent and has a refractive index of 1.65.

In this study the samples were heated in an oven to 350°C and kept at this temperature for a period of time of, typically, two hours. The samples were allowed to cool overnight before the surface was examined with an ellipsometer.

The first sample studied, Sample A, had a 10KÅ layer of aluminum. Five different points on the sample were marked so that measurements could be made at the same spot each time. These five spots were numbered 1, 2, 3, 4, 5 for reference purposes. The sample was heated 16 times and Table 5.2 shows the measurements made prior to the first heating and after each successive heating. The number of hours shown in Column 1 is the total number of hours at 350°C, but excludes the heat up and cool down time. For each spot on the sample this data was plotted, showing that the consecutive measurements generate a Δ vs. ψ

TABLE 5.2
VALUES OF ψ AND Δ FOR THE FIVE SPOTS ON SAMPLE A

Hours at 350°	Point 1		Point 2		Point 3		Point 4		Point 5	
	Δ	ψ	Δ	ψ	Δ	ψ	Δ	ψ	Δ	ψ
0	126.16	41.69	124.88	41.83	126.10	41.69	126.44	41.75	126.51	41.58
2	125.73	41.74	123.18	41.80	124.13	41.61	125.79	41.73	126.02	41.72
4	122.09	41.71	119.53	41.70	119.32	41.59	121.48	41.79	123.05	41.75
6	121.91	41.66	119.25	41.55	119.00	41.73	119.95	41.70	122.50	41.71
8	120.97	41.74	117.89	41.69	117.69	41.69	119.66	41.67	120.26	41.65
10	119.96	41.68	116.97	41.66	116.74	41.44	119.01	41.66	119.98	41.70
12	118.36	41.63	114.86	41.53	115.11	41.62	117.84	41.60	119.18	41.67
14	115.58	41.66	113.51	41.58	113.31	41.64	114.64	41.62	117.36	41.73
16	116.34	41.56	112.57	41.61	112.13	41.58	114.56	41.58	115.70	41.53
18	114.39	41.60	110.59	41.58	109.78	41.45	111.77	41.59	113.43	41.58
21	108.40	41.53	103.36	41.54	105.68	41.54	104.47	41.44	107.18	41.55
24.5	105.45	41.50	100.86	41.37	102.24	41.29	101.49	41.34	104.22	41.50
27.5	105.47	41.39	99.47	41.34	99.81	41.24	99.61	41.21	102.22	41.43
30	103.39	41.41	98.16	41.16	98.02	41.14	98.46	41.11	101.40	41.37
34	101.00	41.47	95.50	41.18	97.29	41.28	97.40	41.18	99.01	41.34
37.5	98.75	41.31	95.19	41.09	95.29	41.08	96.59	41.08	98.39	41.31
41.5	92.33	41.23	89.55	40.06	90.09	41.13	91.47	41.38	94.72	43.55

curve. These data, shown in Figs. (5.2) - (5.6), all follow approximately the same trajectory.

Another sample, Sample B, with a 500\AA film of aluminum was also tested. This sample also was vacuum deposited, but was covered with a layer of collodion to prevent oxidation of the aluminum. After removing the collodion, measurements were taken with the ellipsometer. The sample was then heated twice with measurements being taken after each heating at two distinct spots, a and b, on the sample. Fig. (5.7) shows these data in relation to those taken at Point 1 on Sample A (from Fig. (5.2)).

A study was then undertaken in an attempt to relate the values of ψ and Δ on these curves to the index of refraction of both the substrate and film and to the film thickness. Fig. (4.9) in Section IV shows curves for a substrate index in the range of aluminum for varying thickness and film index. Fig. (5.8) shows an enlarged view for the same substrate index, but with film thickness between 0 and 350\AA . The combined data for the five spots on Sample A and the two spots on Sample B are shown on the figure. The change in the film index between 1.6 and 1.7 has a negligible effect on the curve fit. Comparison of the curve to the measured data shows that the measurements lie farther and farther to the left as the thickness increases. An effort was made to fit a curve to the data by assuming that the film had an effective index that was complex. The assignment of such a complex index can be motivated as follows. Since a rough surface scatters some of the light, the light detected from the reflection is reduced

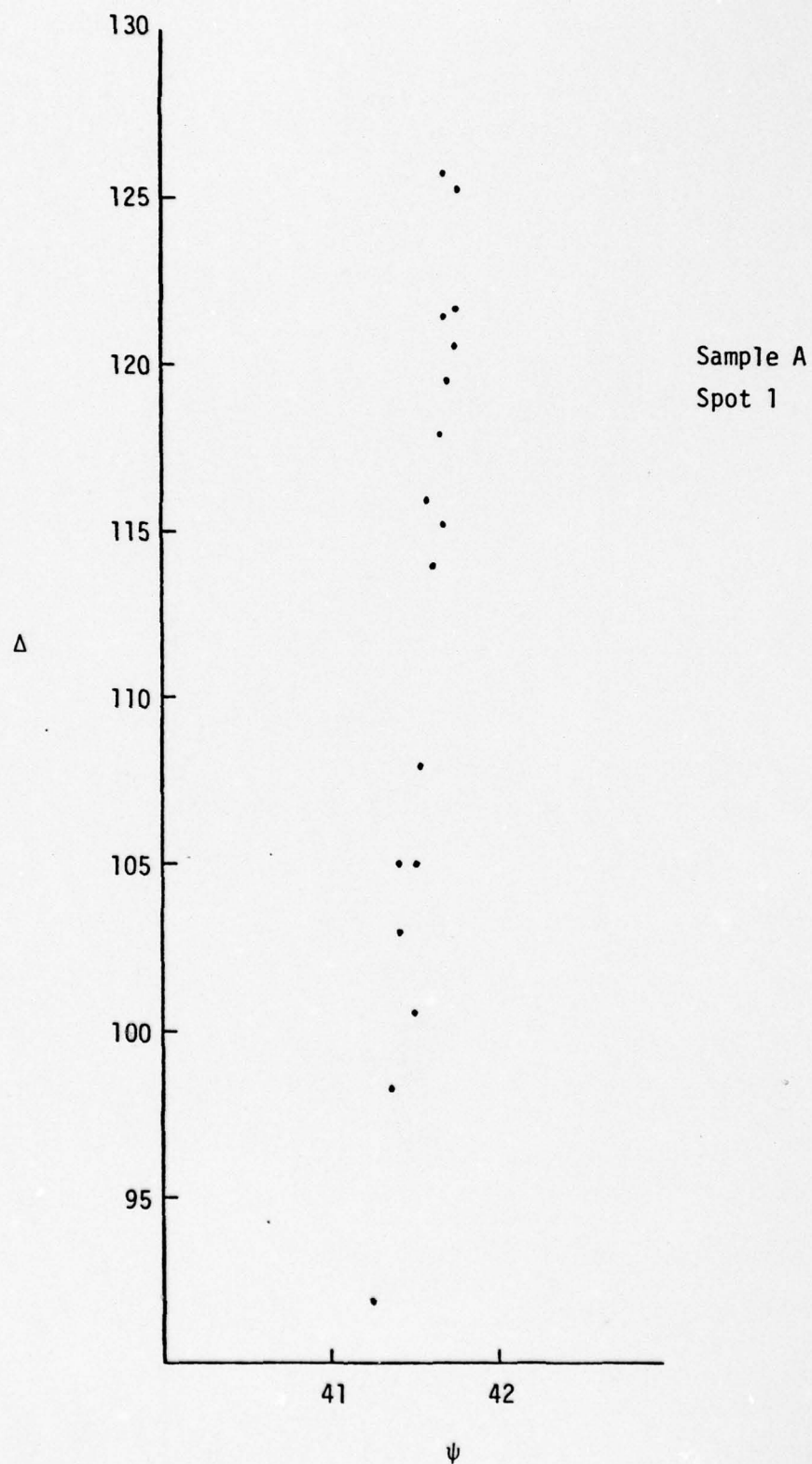


Fig. 5.2 The Data Measured on Sample A at Spot 1 for Successive Heatings

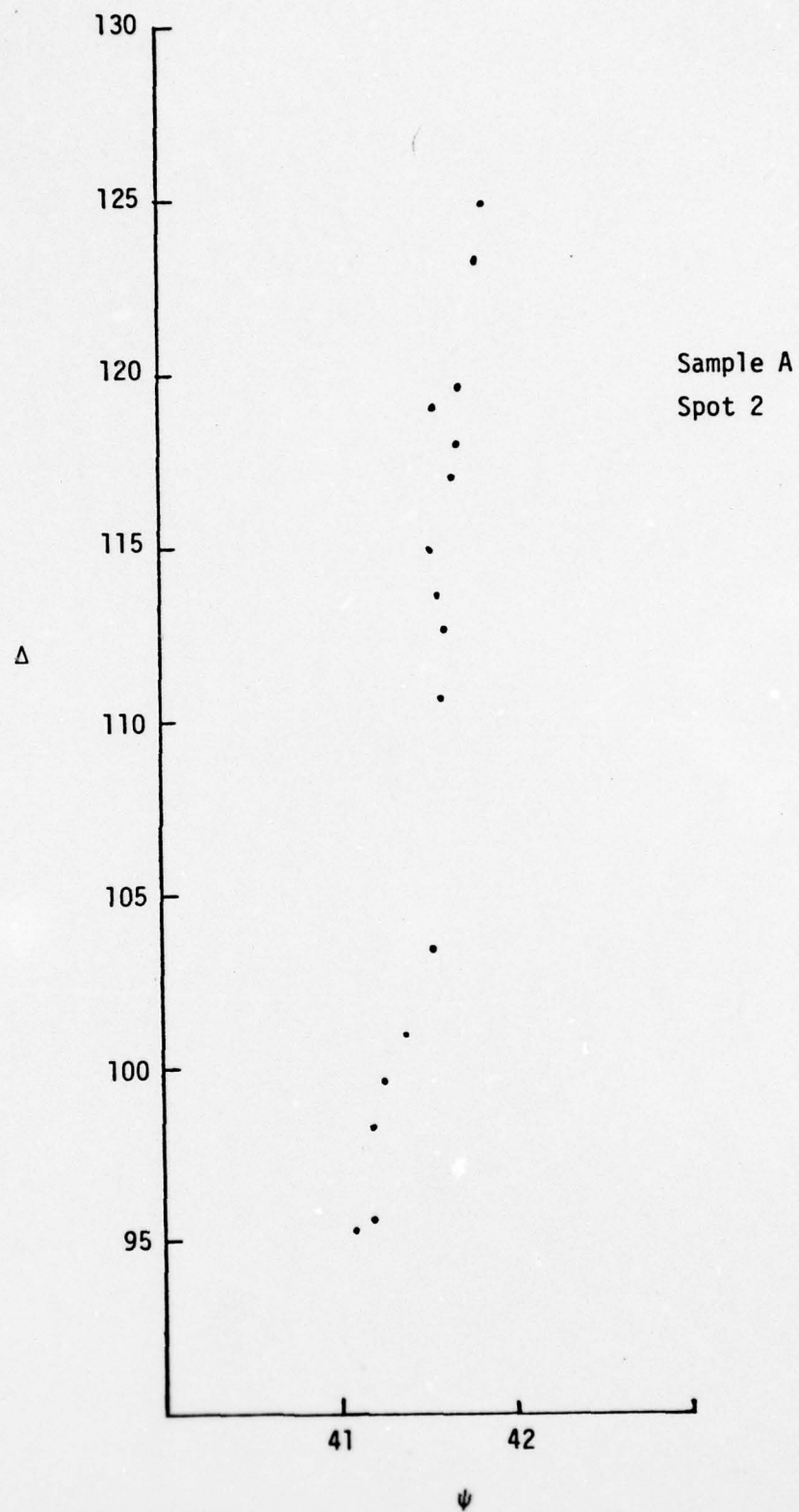


Fig. 5.3 The Data Measured on Sample A at Spot 2 for Successive Heatings

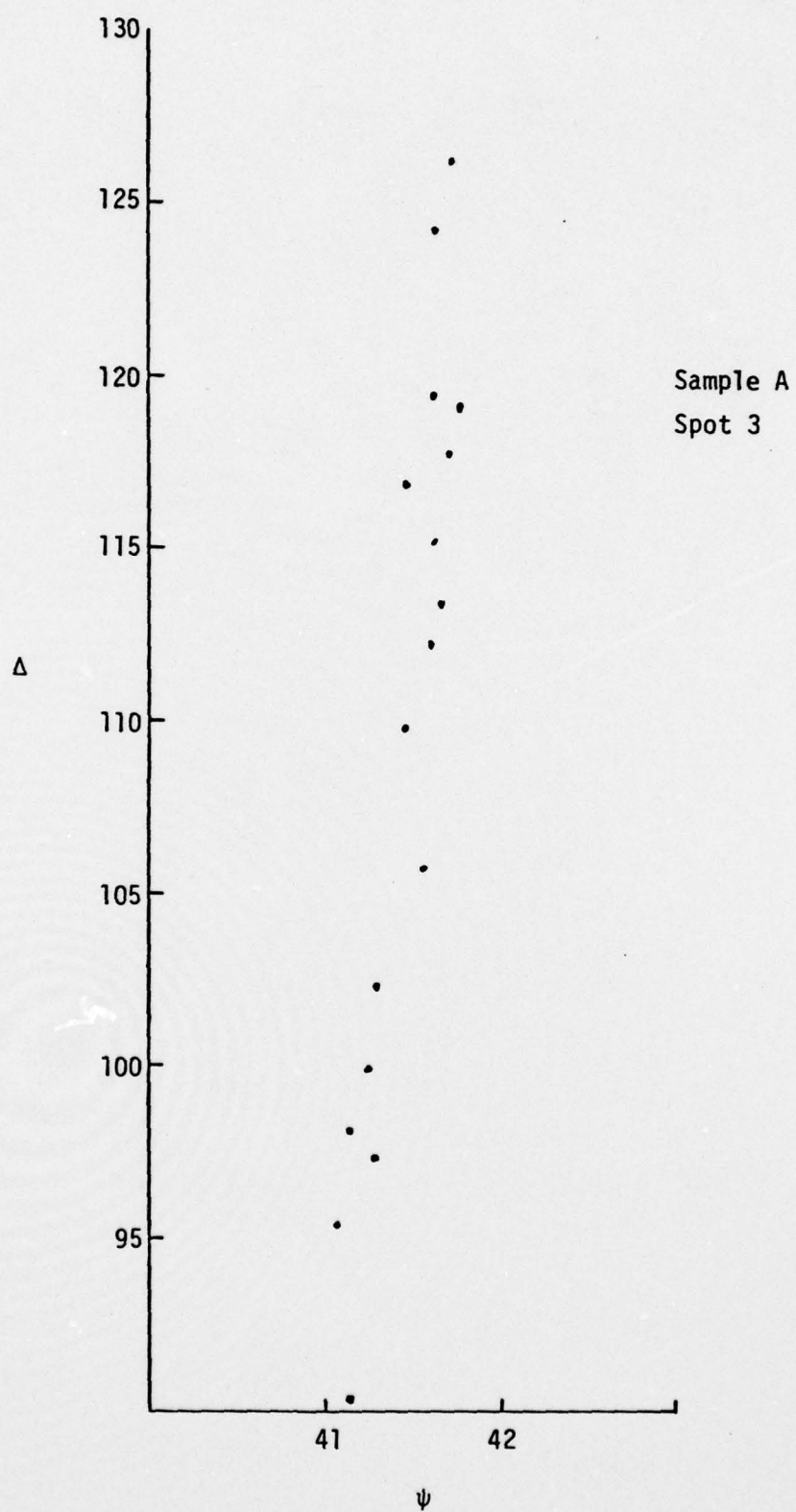


Fig. 5.4 The Data Measured on Sample A Spot 3 for Successive Heatings

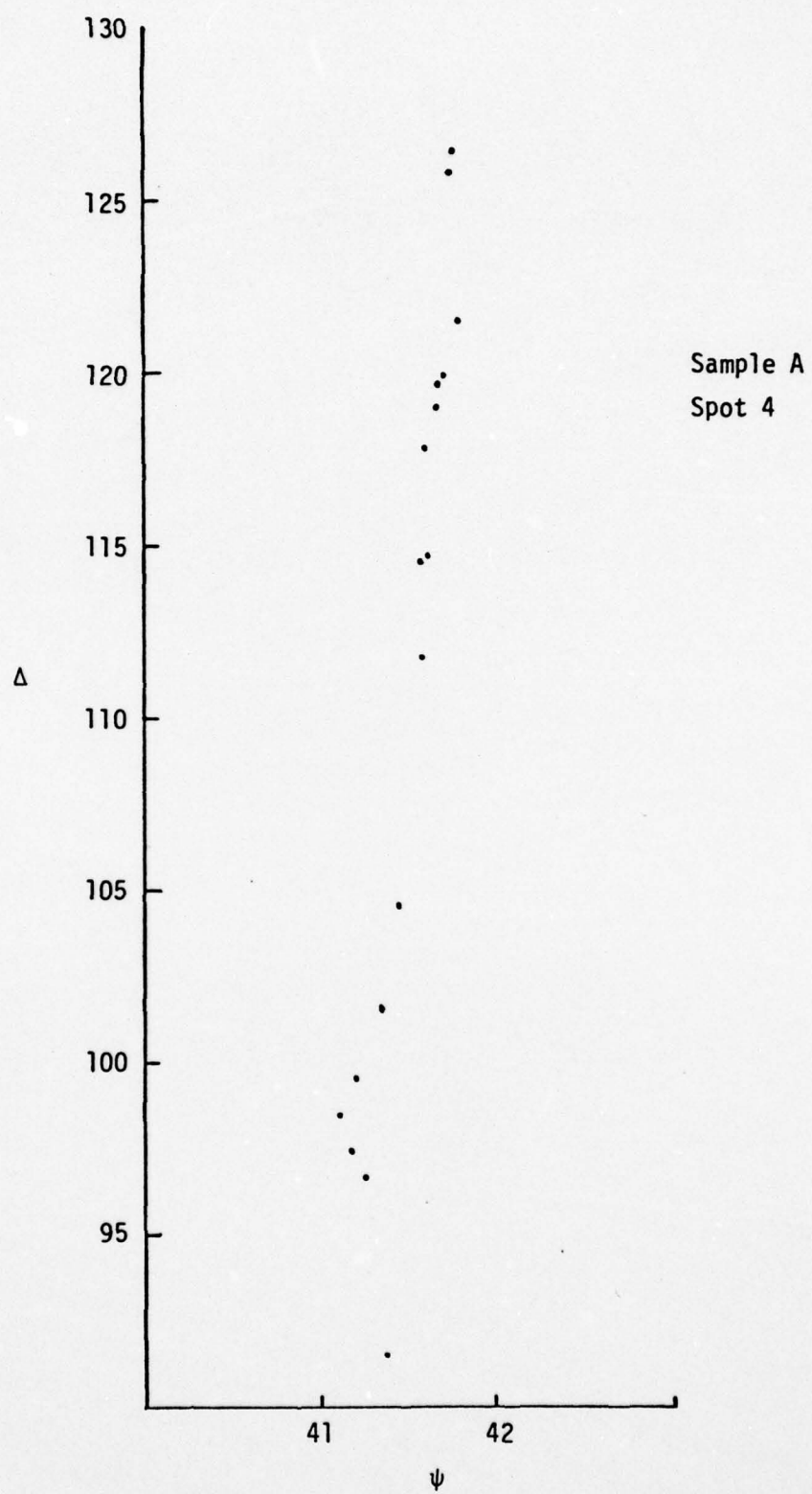


Fig. 5.5 The Data Measured on Sample A at Spot 4 for Successive Heatings

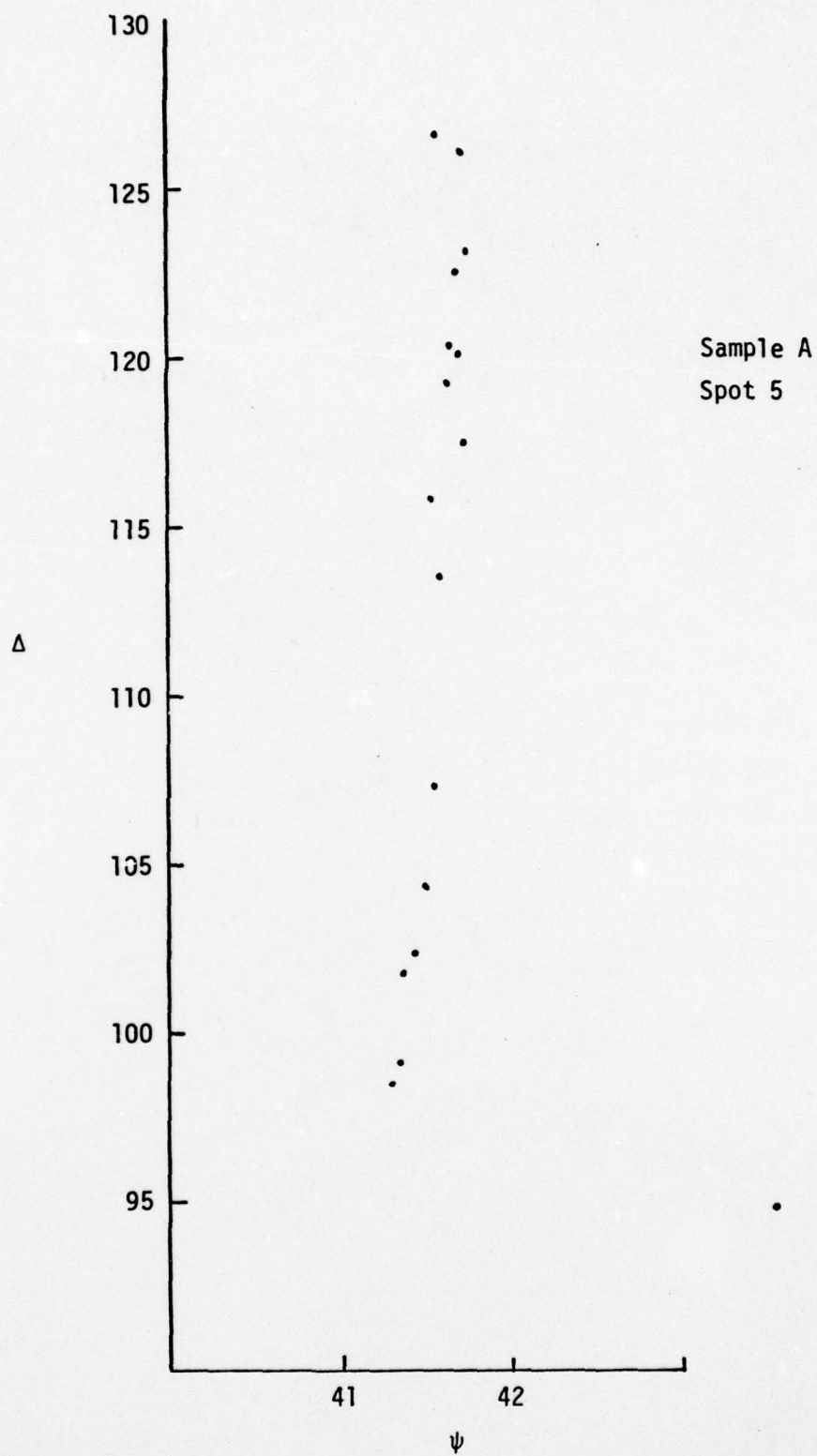


Fig. 5.6 The Data Measured on Sample A at Spot 5 for Successive Heatings

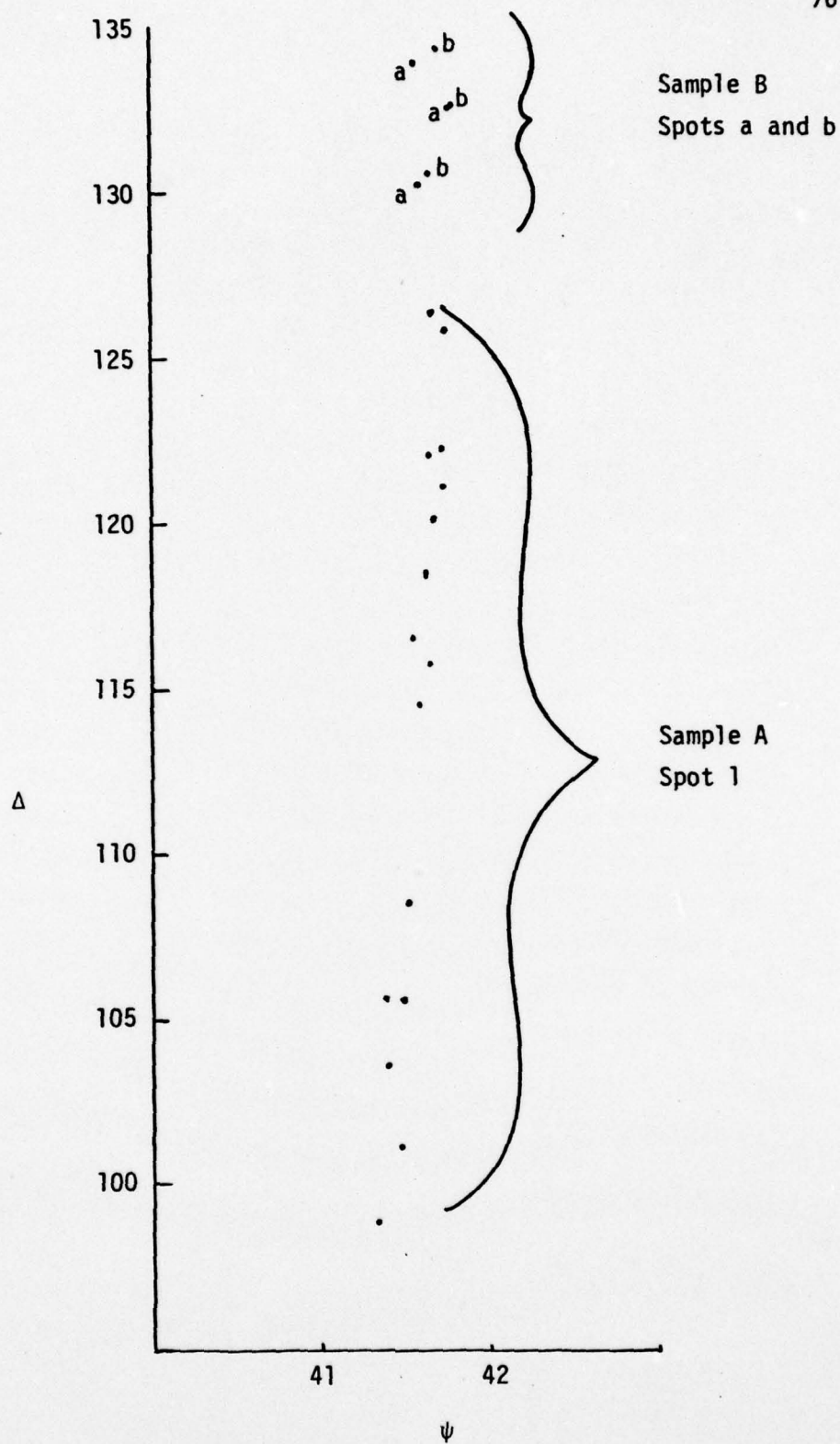


Fig. 5.7 The Data Measured on Sample B Compared with Data from Spot 1 on Sample A

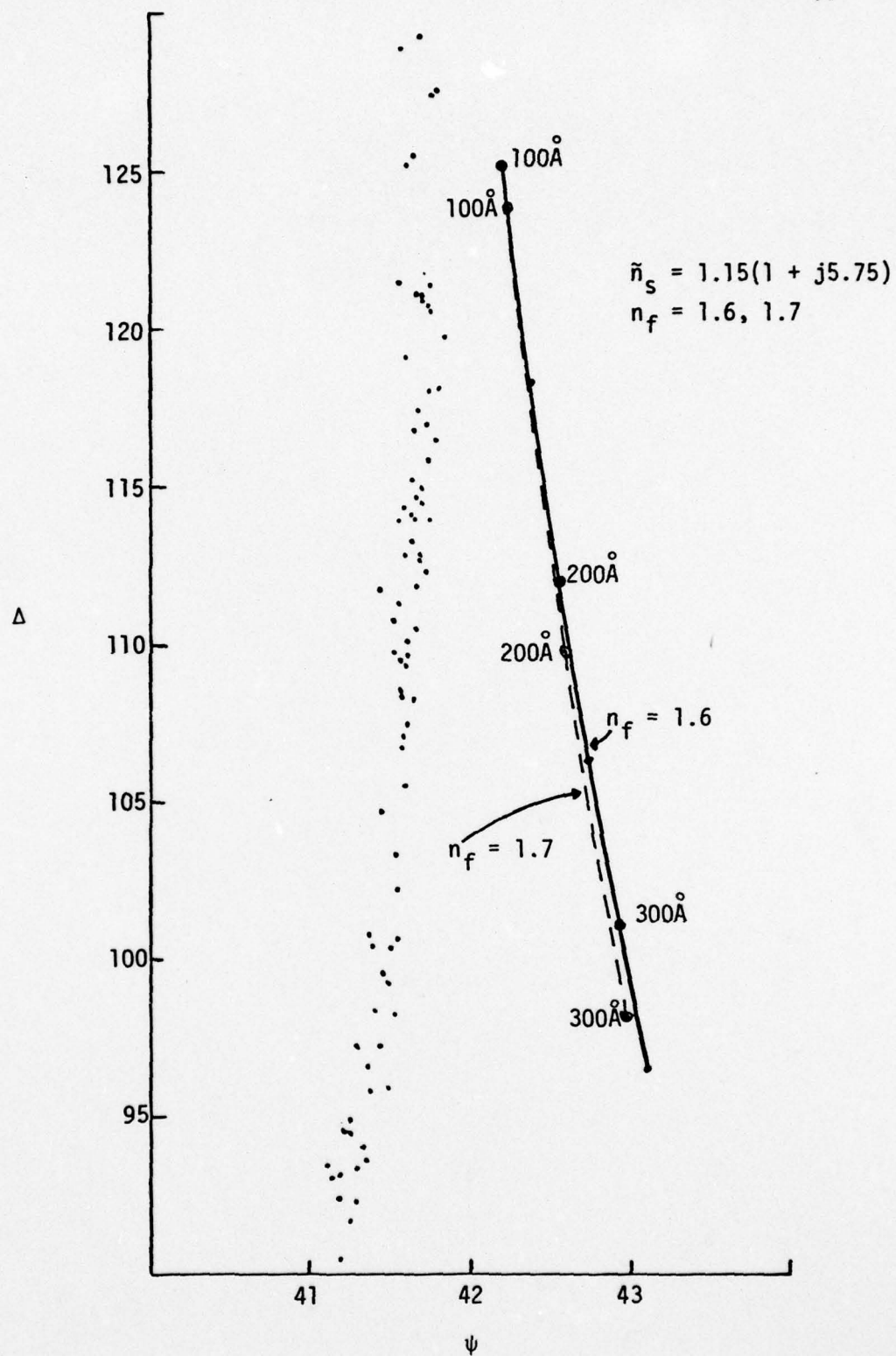


Fig. 5.8 Comparison of Data to Curves for $n_f = 1.6$ and 1.7 (No Extinction Coefficient)

by the loss. The extinction coefficient, K_f , is a term accounting for light absorbed in the material and, therefore, not reflected. Thus, it may be reasonable to treat scattering losses effectively as absorption losses. Fig. (5.9) shows a curve superimposed over the data, using a film index of $\tilde{n}_f = 1.65 (1 + j0.06)$. The substrate index for this curve was $1.15 (1 + j5.75)$. This curve fits the data much better, but the data and the curve tend to bow in opposite directions. An effort to make a better match involved making the imaginary part of the film index directly related to the film thickness. Fig. (5.10) shows two curves using the model

$$K_f = (0.01) \frac{t}{50} \quad (5.1)$$

where t is the oxide film thickness in \AA . The substrate indices for these two curves are $1.15 (1 + j5.45)$, as in Fig. (5.9), for one and $1.65 (1 + j4.75)$ for the other. For the $1.15 (1 + j5.45)$ case the standard deviation of the sample data was evaluated for the fixed value $K_f = 0.06$, used in Fig. (5.9), and for the K_f model of Eq. (5.1) shown in Fig. (5.10). The deviation was 3.39 for the curve employing $K_f = 0.06$ and was 2.07 for the curve based on the K_f -thickness model of Eq. (5.1). The arbitrary unit of these standard deviations was 1/20 of an inch. These calculations show that the curve in which the absorption term, K_s , varies matches the data much better.

C. A. Fenstermaker and F. L. McCrackin[9] have constructed theoretical models for errors in ellipsometric measurements due to surface roughness. They modelled surfaces as square ridges, triangular ridges, and pyramids of equal height and width. The size of this

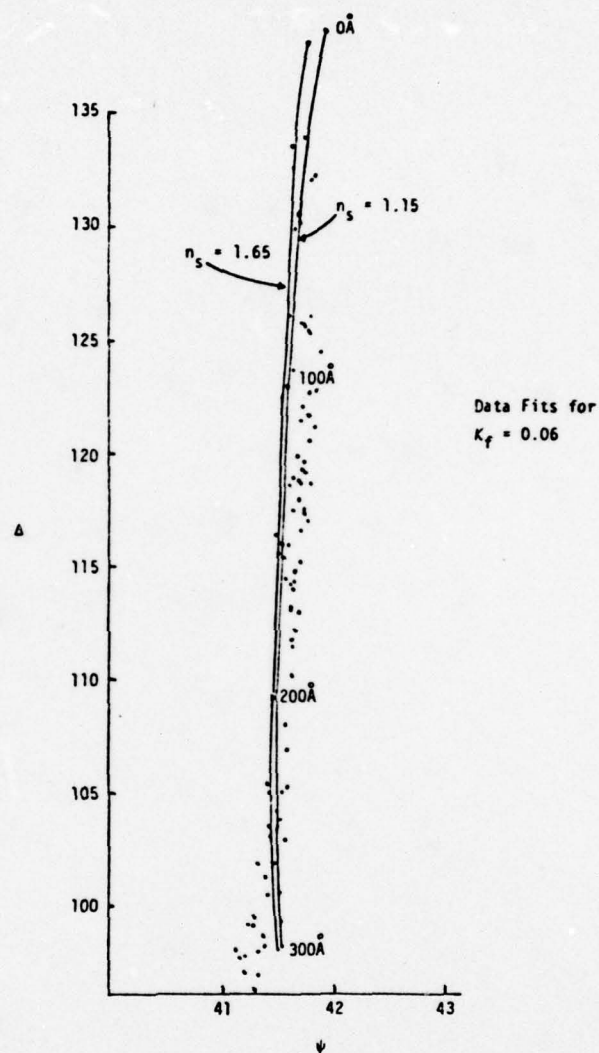


Fig. 5.9 Comparison of Data to Curves Where the Film Index has an Extinction Coefficient

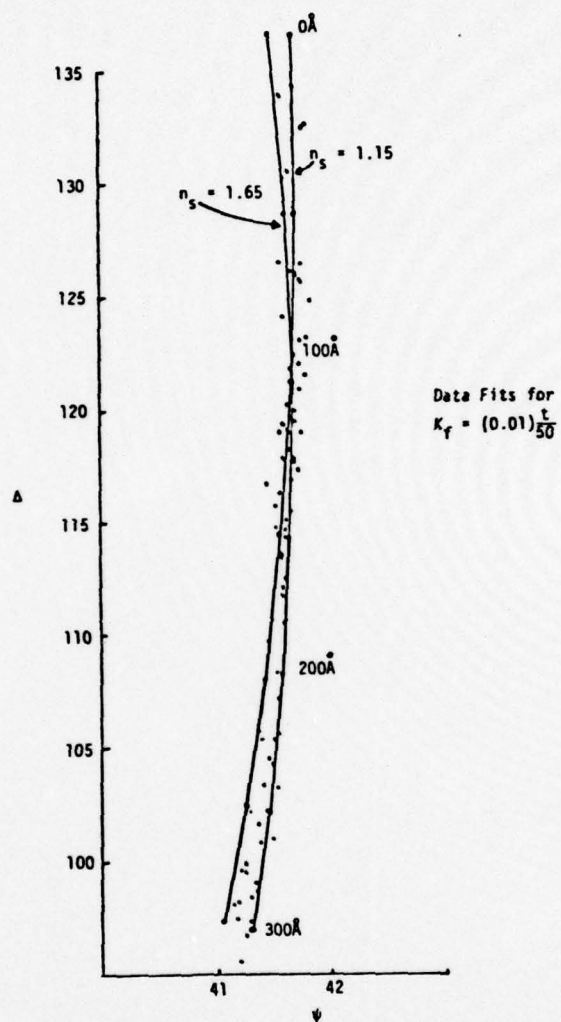


Fig. 5.10 Comparison of Data to Curves Where the Film Extinction Coefficient Varies with Thickness

roughness was varied from 0 to 500Å. The model was applied to several materials with the true, complex, indices of refraction as given below:

<u>Material</u>	<u>n</u>	<u>K</u>
glass	1.50	0.0
silicon	4.05	0.0068
chrome	3.00	1.4
mercury	1.485	3.061
gold	0.35	7.0
silver	0.18	19.0

Since the true index of glass has no absorption, it is assumed that this most nearly resembles the aluminum oxide. Therefore, it is these results which would be interesting for this case. Fig. (5.11) shows the calculated changes in n and K for glass due to surface roughness obtained by Fenstermaker and McCrackin. The apparent value for the real part of the index changes very little, but the apparent value of K increases significantly with surface roughness.

Since the aluminum oxide layer would tend to grow unevenly, one might expect the surface to become rougher as the thickness increases. The results of Fenstermaker and McCrackin do show an increase in K_f as the film thickness increases. Fig. (5.10) confirms, for this case, that the roughness (as measured by t) appears to increase the effective value of the extinction coefficient, K_f .

As the two curves in Fig. (5.10) illustrate, various pairs (n_s , K_s) can be used to achieve a good fit to the data, using the

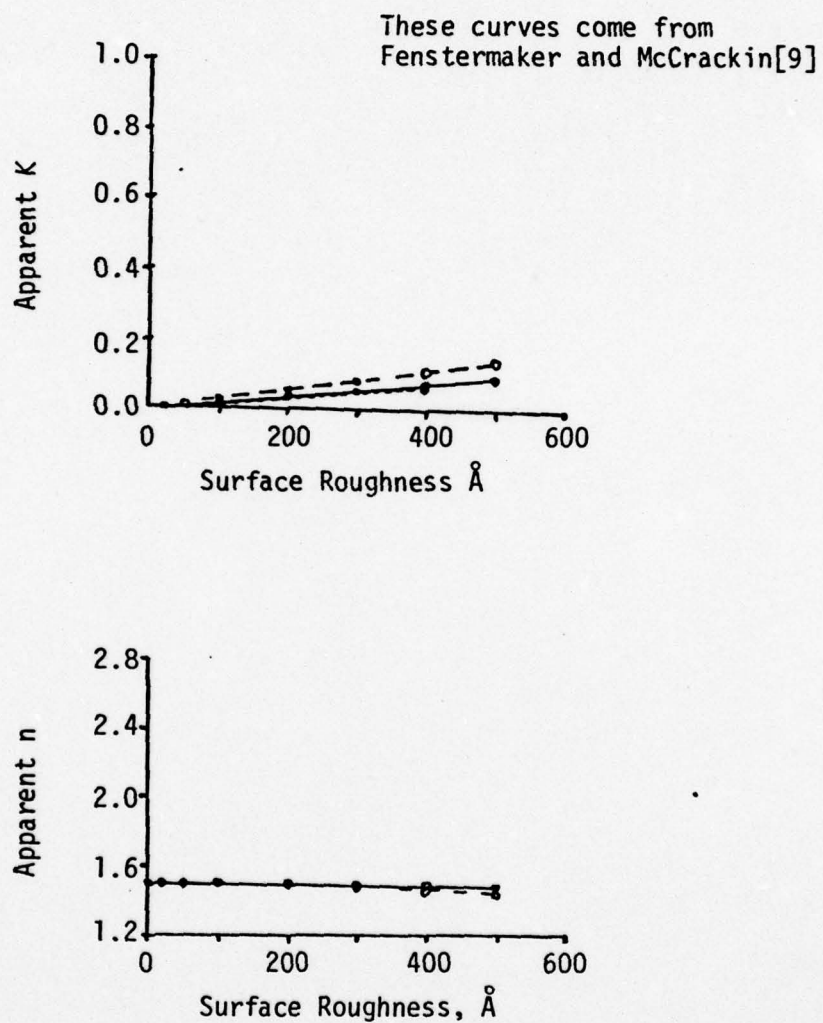


Fig. 5.11 Calculated Changes in n and K Due to Surface Roughness of Glass

K-thickness model of Eq. (5.1). Curves resulting from other suitable index choices are shown in Fig. (5.12). This lack of uniqueness could be resolved if the actual film thickness were known. As shown in Fig. (5.12), the thickness scales, t , on the curves for different (n_s, K_s) are pairs are quite different.

Previous determinations of the substrate refractive index for pure aluminum with thin films show a wide range of variation.[6,7,10,11] Some of the values found for the substrate refractive index in the last twenty-five years are shown in Fig. (5.13).[†] In this figure the real part n_s is shown plotted against the extinction coefficient K_s . The curve marked A in Fig. (5.13) gives the locus of index values which fit the data of the present study when the fixed value $K_f = 0.06$ is used, as in Fig. (5.9). The curve marked B in Fig. (5.13), on the other hand, gives the locus of index values which fit the data when the model of Eq. (5.1) is used, as in Figs. (5.10) and (5.12). Curve B is specified by the linear relation

$$K_s = 7.175 - \frac{3}{2}n_s \quad . \quad (5.2)$$

It may be seen that Curve B provides a nice fit to the widely scattered determinations by other workers. That Curve B gives a good fit to this data has two important consequences. First, this fit gives

[†]The point marked F on the figure is only an estimate made for 6328Å light, based on the work of Fane and Neal[6] done at a wavelength of 5490Å. The estimate was made using the trend of the data with λ determined by Hass and Waylonis.[11]

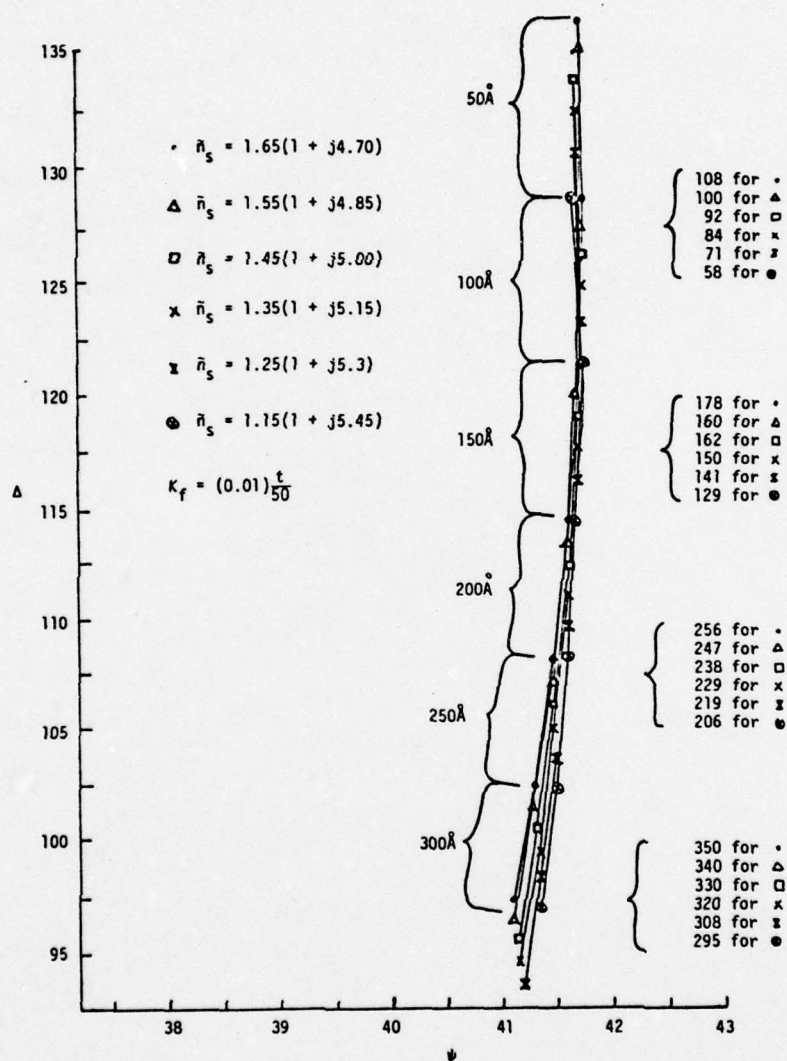


Fig. 5.12 Comparison of Several Curves Demonstrating a Lack of Uniqueness for the Curve Fit

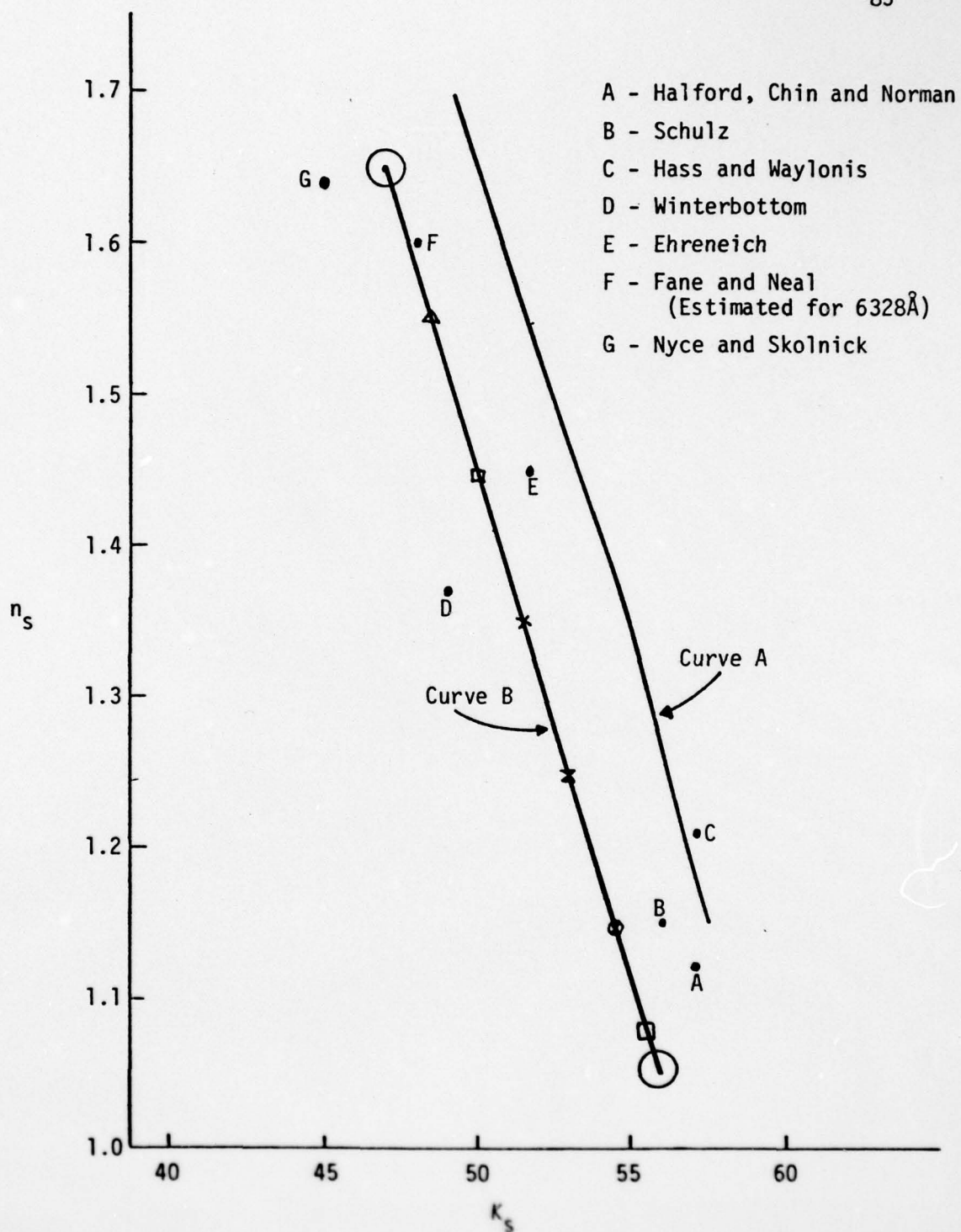


Fig. 5.13 Comparison of the Values for the Substrate Index Found by Various Authors

AD-A056 782

TEXAS TECH UNIV LUBBOCK OPTICAL SCIENCES LAB
ELLIPSO-METRIC DETERMINATION OF PROPERTIES OF FILMS ON ROUGH SUR--ETC(U)
AUG 77 J D REICHERT, J S BROCK

F/G 14/2

AFOSR-77-3278

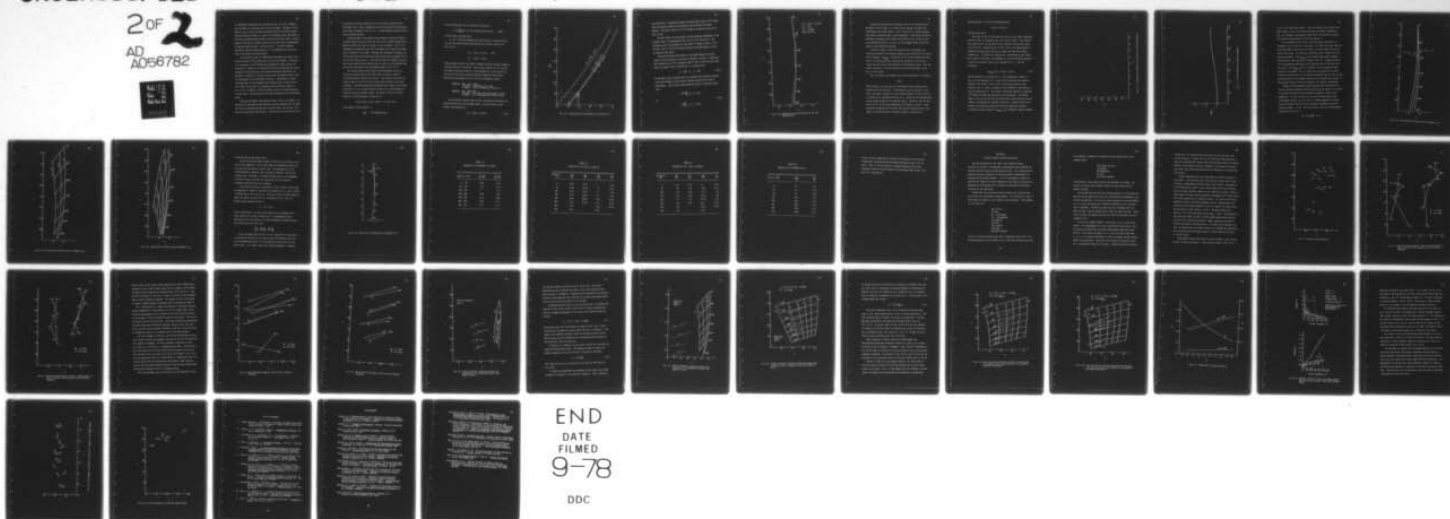
UNCLASSIFIED

TTCSL-OLT-3

AFOSR-TR-78-1220

NL

2 OF 2
AD
A056782



END
DATE
FILMED
9-78
DDC

an independent indication that the model of Eq. (5.1) may, indeed be very suitable for the oxide films on pure aluminum. Secondly, Curve B offers a way of reconciling the scattered results of previous workers. The missing piece of data, at least in the present study, that makes it difficult to determine which point on Curve B should be taken, is knowledge of the actual thickness of any of the oxide layers corresponding to the data shown in Figs. (5.9) and (5.10). It may be supposed, therefore, that this same parameter, t , is responsible for the variation in the results of other workers.

In the present study, no independent measurement was made of the actual thickness of the oxide layer on any of the samples. Therefore, it is necessary to use thickness data obtained by other workers for calibration. Because it is extremely difficult to determine the actual thickness of the oxide layer on aluminum substrates and because the thickness is subject to variations based upon the sample history, there is disagreement in the available literature. Nevertheless, certain limiting values can be presumed with reasonably good reliability and such limits can be used, in conjunction with the results shown in Fig. (5.13), to deduce a likely thickness scale for the data obtained in this study. The strategy used for the calibration will be explained below.

The data for Sample A and Sample B shown in Fig. (5.7) appear to be mutually consistent so that the data has been combined into a single set for the succeeding figures and for conclusions, such as Eqs. (5.1) and (5.2) based upon those figures. The fact that the histories of the

two samples was quite different will now be used to determine the thickness scale. Such a procedure can only be justified by the mutual consistency evidenced in Fig. (5.7): a single smooth trajectory can be passed through the data.

Although Sample A and Sample B were prepared similarly, Sample A had been exposed to the air for well over a year, whereas Sample B was measured within four hours of removal of the collodion. Thus it is reasonable to expect that the layer on Sample A had reached the asymptotic thickness of 40 to 55Å. Although this asymptotic thickness cannot be stated with great precision, many workers have determined it to lie in this range.[6 and 7] The layer thickness on Sample B, on the other hand, should be much thinner and its value can be estimated from the results obtained by Fane and Neal[6] shown in Fig. (5.1).

The results shown in this figure allow estimation of $\delta\Delta$ as a function of growth time of the oxide layer, and show a value of $\delta\Delta \approx 100$ minutes of angle at four hours. The results of the various studies shown in Fig. (5.12) can then be used to relate $\delta\Delta$ to layer thickness. Using the theoretical thickness scales shown on the figure, variations in Δ can be read from the vertical axis corresponding to thickness values from 50Å to 100Å. The results for the six curves shown are (in Å/100 minutes of angle in Δ):

10.62, 10.55, 10.75, 10.82, 11.11, and 11.33.

The average of these results is

$$\frac{\delta t}{\delta \Delta} \quad 10.9 \text{ Å/100 minutes.}$$

Thus the thickness can be estimated for Sample B:

$$t \approx \left(\frac{\delta t}{\delta \Delta}\right)(\delta \Delta) \approx (10.9 \text{ \AA}/100 \text{ min})(100 \text{ min}) \quad 10.9 \text{ \AA}$$

at four hours of growth time.

In Fig. (5.14) the theoretical film thickness is shown versus Δ for the two extreme index values marked by circles on Curve B of Fig. (5.13):

$$\tilde{n}_s = 1.65(1 + j4.70) \quad \text{and}$$

$$\tilde{n}_s = 1.05(1 + j5.56) \quad .$$

These extreme values of the index encompass the wide variation found by previous workers in the field. One can see, directly in Fig. (5.14), the range of possible value of t corresponding to a given value of Δ . The two limiting cases discussed above for Samples A and B before heating are also marked on Fig. (5.14) as rectangular regions:

Sample A. age: over a year
thickness: asymptotic, 40 to 55 \AA
 Δ values: five, corresponding to Spots 1-5

Sample B. age: four hours
thickness: less than 12 \AA, approximately 10.9 \AA
 Δ values: two, corresponding to Spots a and b.

The rectangular regions shown in Fig. (5.14) barely intersect the band defined by the index extremes shown. The third curve in the figure, corresponding to

$$\tilde{n}_s = 1.08(1 + j5.555) \quad (5.3)$$

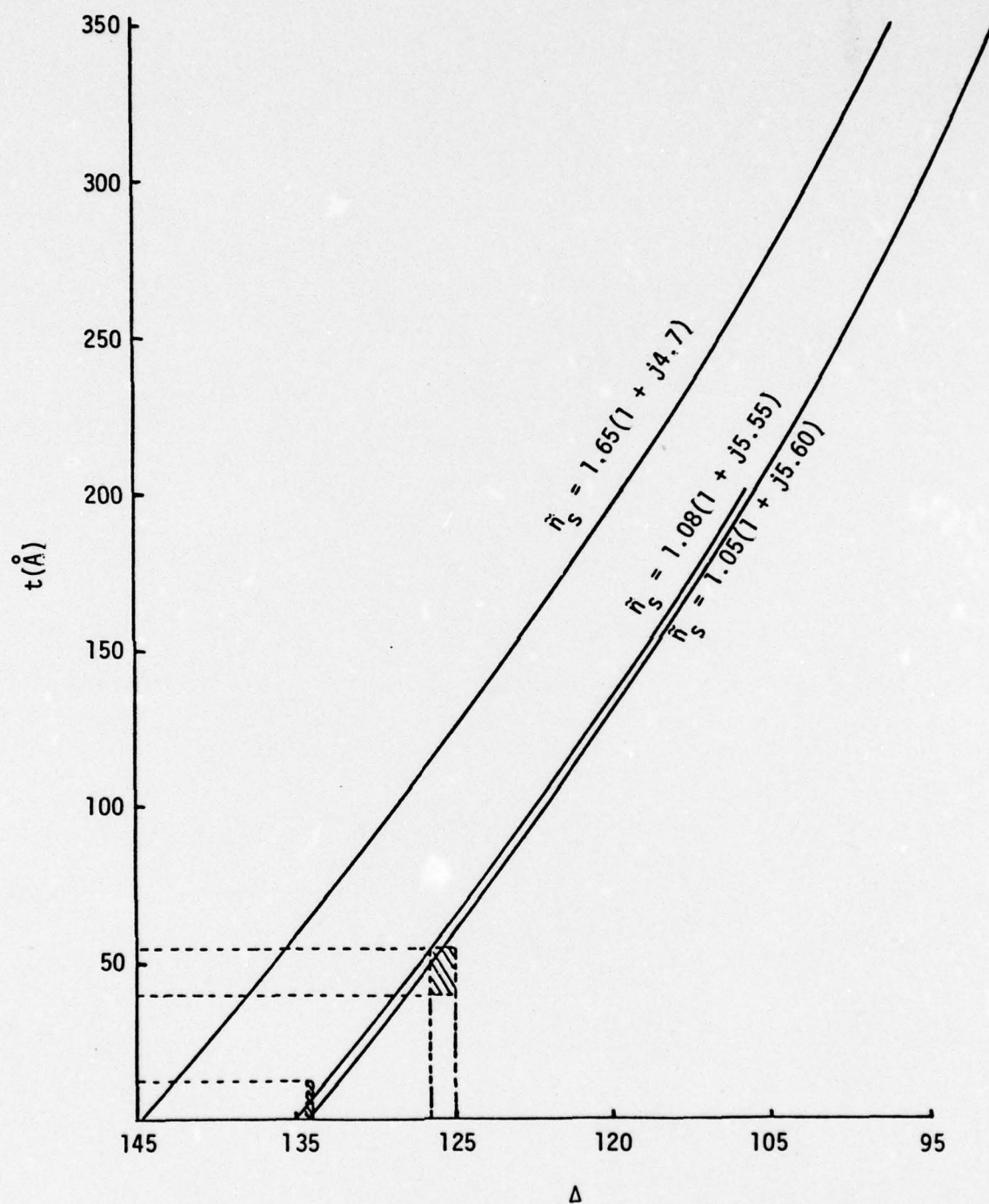


Fig. 5.14 Theoretical Film Thickness as a Function of Δ

was selected as a compromise between the index data found in this study (and by previous workers) and thickness data obtained from other workers. The point from Eq. (5.3) is shown as a square on Curve B in Fig. (5.13).

The full model for oxide layers on pure aluminum, developed in the present study, is summarized by Eqs. (5.1), (5.2), and (5.3). The thickness curve corresponding to this model is shown on the ψ, Δ plot of Fig. (5.15). All of the data obtained by heating Samples A and B is shown on this curve.

The justification given above for the model deduced for oxide layers on pure aluminum is certainly vulnerable to errors. Based upon the intersection of the rectangles shown in Fig. (5.14) with the index band, one might claim an uncertainty in t ranging from

$$t + 7.5\text{\AA} \quad \text{to} \quad t - 15\text{\AA} \quad . \quad (5.4)$$

On the other hand, one might wish to recognize the extremely conservative error estimates which result from the entire band of index uncertainty. Such an error bound would vary with Δ and would range from

$$t \begin{array}{c} +57.5\text{\AA} \\ - \quad 5\text{\AA} \end{array} \quad \text{at} \quad \Delta = 130^\circ \quad (5.5)$$

to

$$t \begin{array}{c} +65\text{\AA} \\ - \quad 5\text{\AA} \end{array} \quad \text{at} \quad \Delta = 110^\circ$$

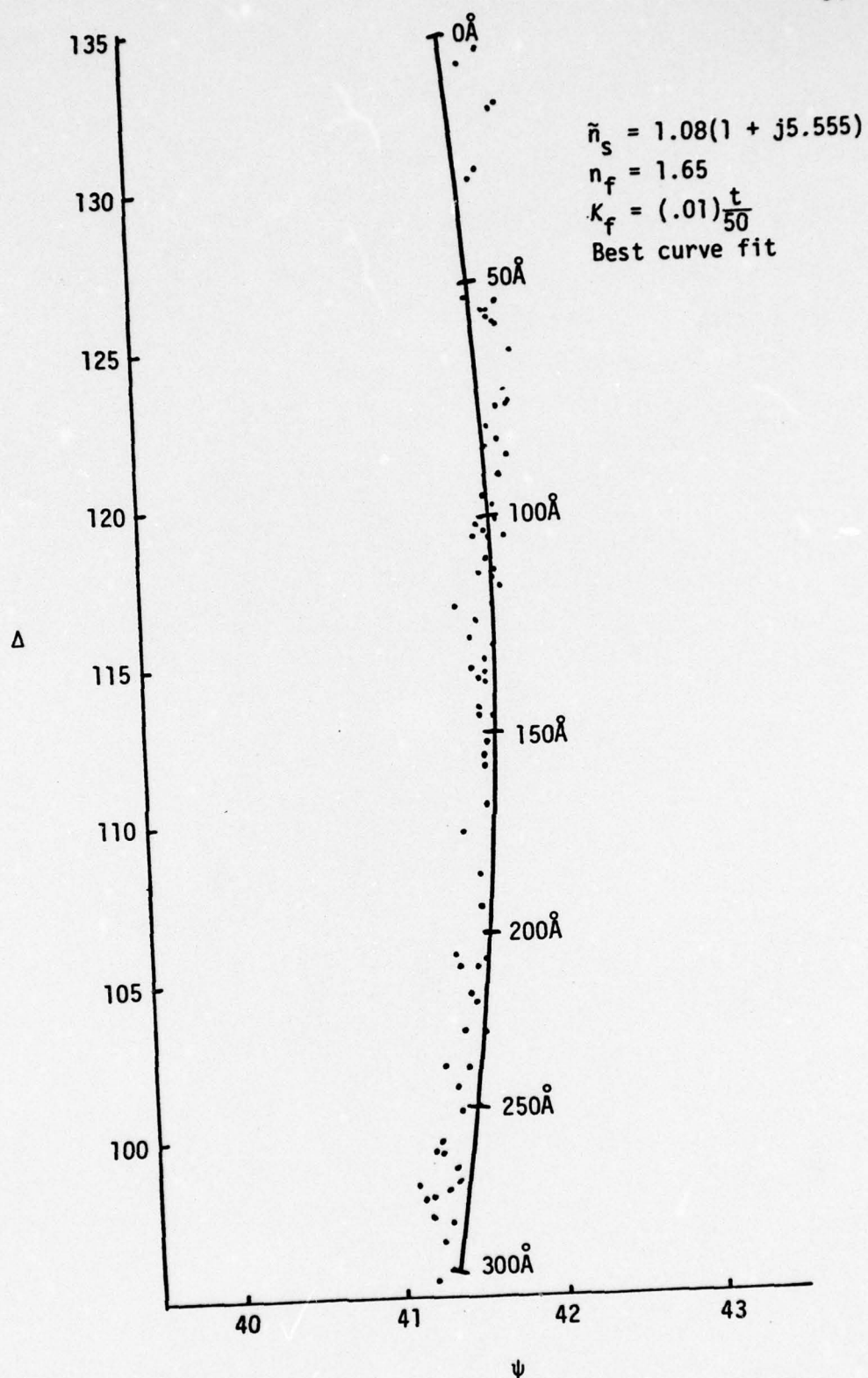


Fig. 5.15 Theoretical Curve with Best Fit for the Measured Data

Granted the possibility of absolute error in the construction of the model of this study, it is also of some interest to apply some significance test to the theory. This is, after all, a rather presumptive theory, presuming that a single parameter t , defining an effective thickness according to the single curve shown in Fig. (5.15) can usefully characterize the ψ , Δ results of the somewhat rough oxide films grown on pure aluminum substrates.

In order to make a crude significance test of the model, the following procedure was followed, leading to the definition of a statistical parameter: δt_{model} . Referring to Fig. (5.15) presume that some origin is selected on the ψ , Δ plot at ψ_0 around 41° or 42° and Δ_0 larger than the value of the 0\AA point of the thickness curve. Call the origin selected 0. The exact location of 0 will not matter to this test in first order.

Now, any point on the theory curve can be located by its distance

$$r_c(t_c)$$

from 0, where t_c is the value of the thickness scale reading at the selected point on the curve. The distance r_c can be measured in any units, say inches, because its only relevant property is that $r_c(t_c)$ is a monotonically increasing function of t_c . Because of the monotonicity, one may speak instead of the function $t_c(r_c)$. Similarly, the i th data point on Fig. (5.15) can be measured at a distance r_i from 0. A perpendicular projection of the data point onto the closest point of the theory curve then defines a thickness reading t_i which can be

associated with r_i to give the parametrization

$$r_i(t_i) \text{ or } t_i(r_i)$$

for each data point.

The curve in Fig. (5.16) shows $t_c(r_c)$ with r_c in inches, measured from an origin, 0, located at $(\psi_0, \Delta_0) = (41.5^\circ, 155^\circ)$. Also shown in the figure are all of the points $t_i(r_i)$ obtained from the data shown in Fig. (5.15). The data points in Fig. (5.16) are then bounded by drawing two curves $t_u(r_c)$ and $t_\ell(r_c)$, upper and lower data bounds, respectively. In order now to measure the significance of the theory with respect to the data, the parameter r_c can be eliminated graphically and one can obtain t_u and t_ℓ as functions of t_c . Then the difference

$$\delta t_{\text{theory}}(t_c) \equiv t_u(t_c) - t_\ell(t_c) \quad (5.6)$$

may be obtained as a function of t_c . This difference is shown in Fig. (5.17), expressed in \AA . It must be stressed that the quantity defined in Eq. (5.6) is not an error in the usual sense of error analysis, but is, rather, a measure of the relevance of the theory to the data supporting it. This theory significance measure is expressed in \AA simply to offer some perspective to the measure. The results shown in Fig. (5.17) have only the qualitative interpretation that the theory is reasonably well matched to the data. Another theory curve tested in the same way against the same data might have revealed considerably larger values of δt_{theory} and, therefore, might be judged

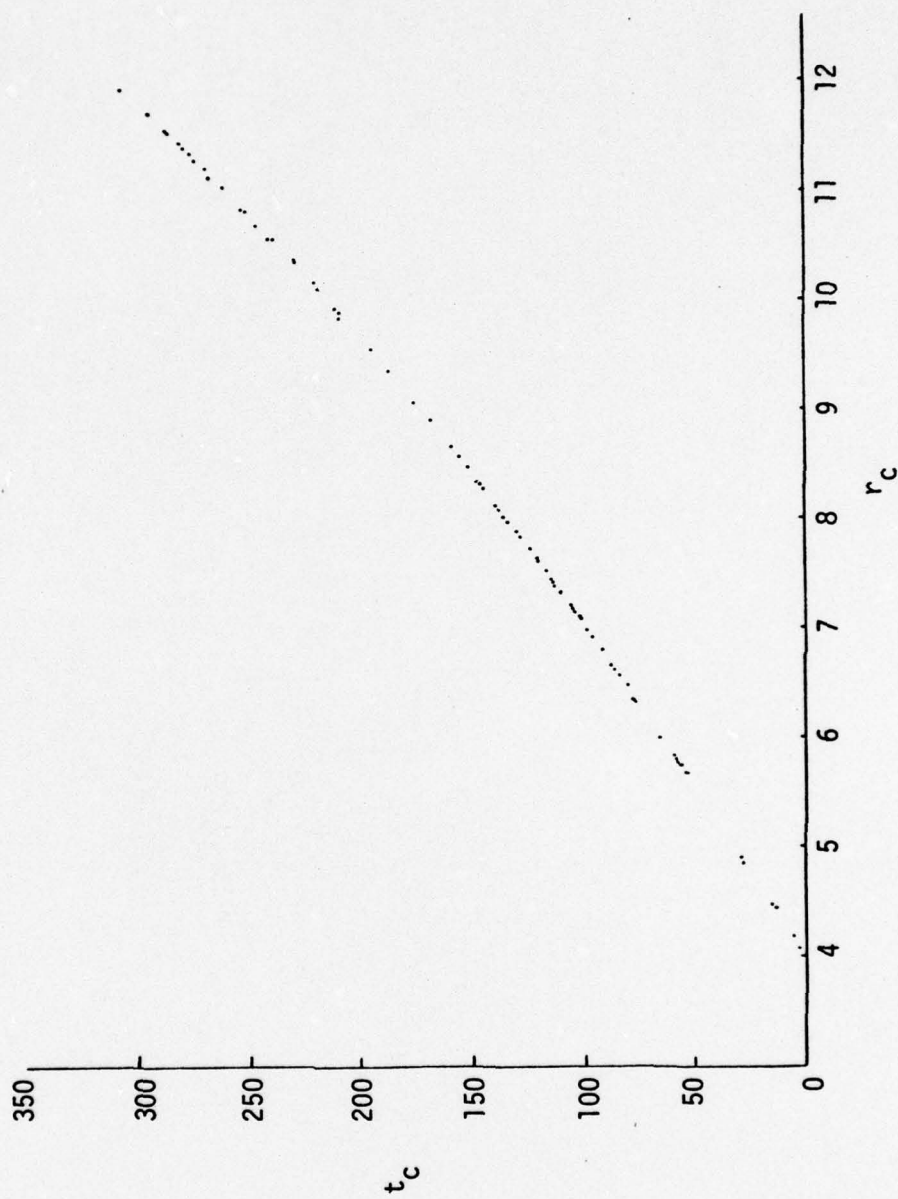


Fig. 5.16 A Monotonic Function of t_c Used in the Theory Analysis

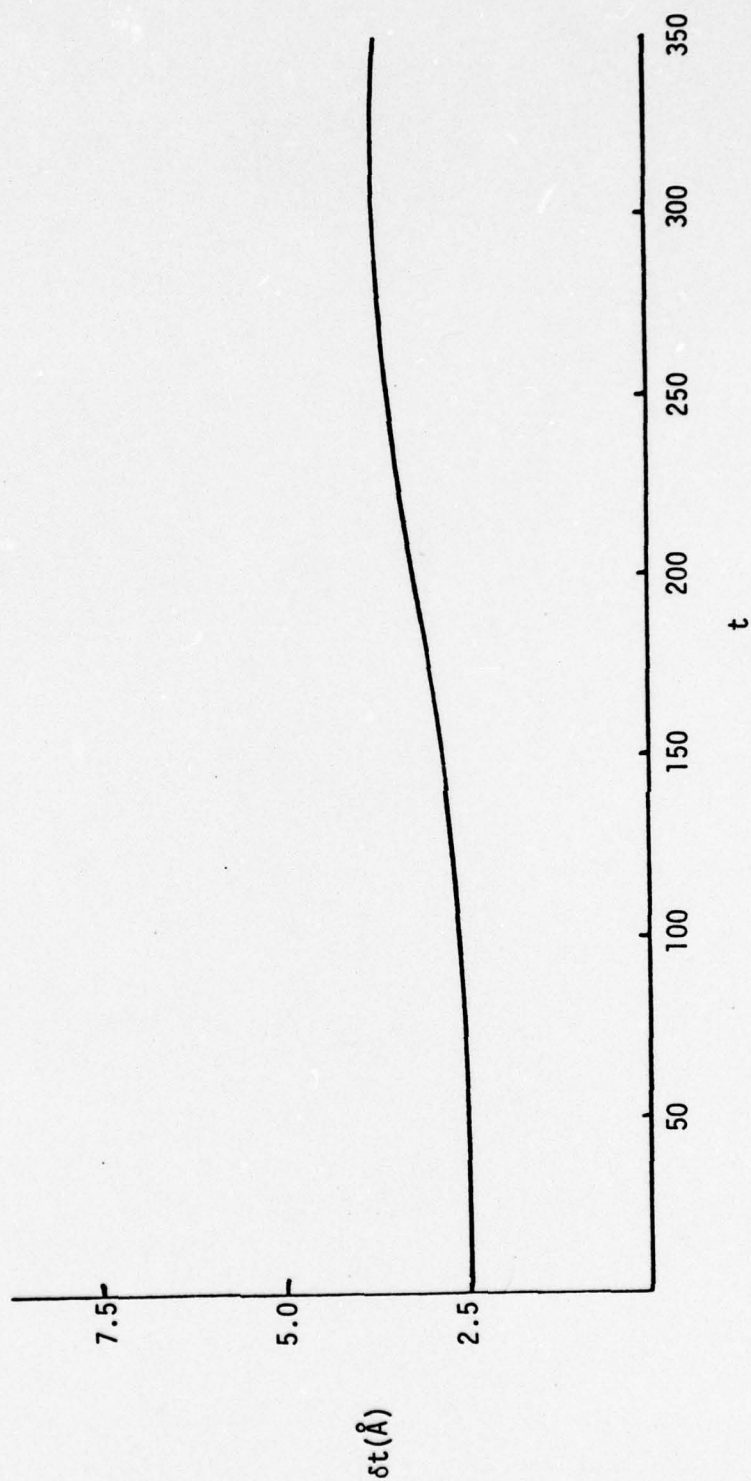


Fig. 5.17 Error Analysis for Theory Relevance

to be a less significant theory. Also, the width of the "theory error band" shown in Fig. (5.17) might indicate a systematic increase as, say, t_c increased. Such behavior would offer the qualitative suggestion that the theory begins to fail for large t_c .

As one examines Fig. (5.15), it may be noticed that there is a systematic error in the fit to the data: for large Δ the data tends to be to the right of the curve; for small Δ the data tends to be to the left of the curve. It is obvious, therefore, that a better curve fit could be achieved. The δt_{theory} test proposed above would, however, give about the same results for a better curve fit. Goodness of data fit is measured by quantities such as RMS deviation of the data from the curve. The δt_{theory} test is intended to try to measure another feature of the theory: is it a useful way to parametrize the data? Although a better curve fit is obviously possible, there is not a large enough data base in the present study to justify additional tuning. It does appear, however, that the strategy of the theory is meaningful.

Because of the reasonably complex method used to determine the various effective parameters which characterize the media, it is useful to note the sensitivity of the thickness parameter to the various parameters. In Figs. (5.18), (5.19), and (5.20) the model curve, corresponding to Eqs. (5.1) to (5.3), is shown together with nearby curves that would result if one of the media parameters were to be charged slightly. In Fig. (5.18) variations in K_f are illustrated by modifying Eq. (5.1) to:

$$K_f = (0.01) \frac{t}{50} \pm 0.01$$

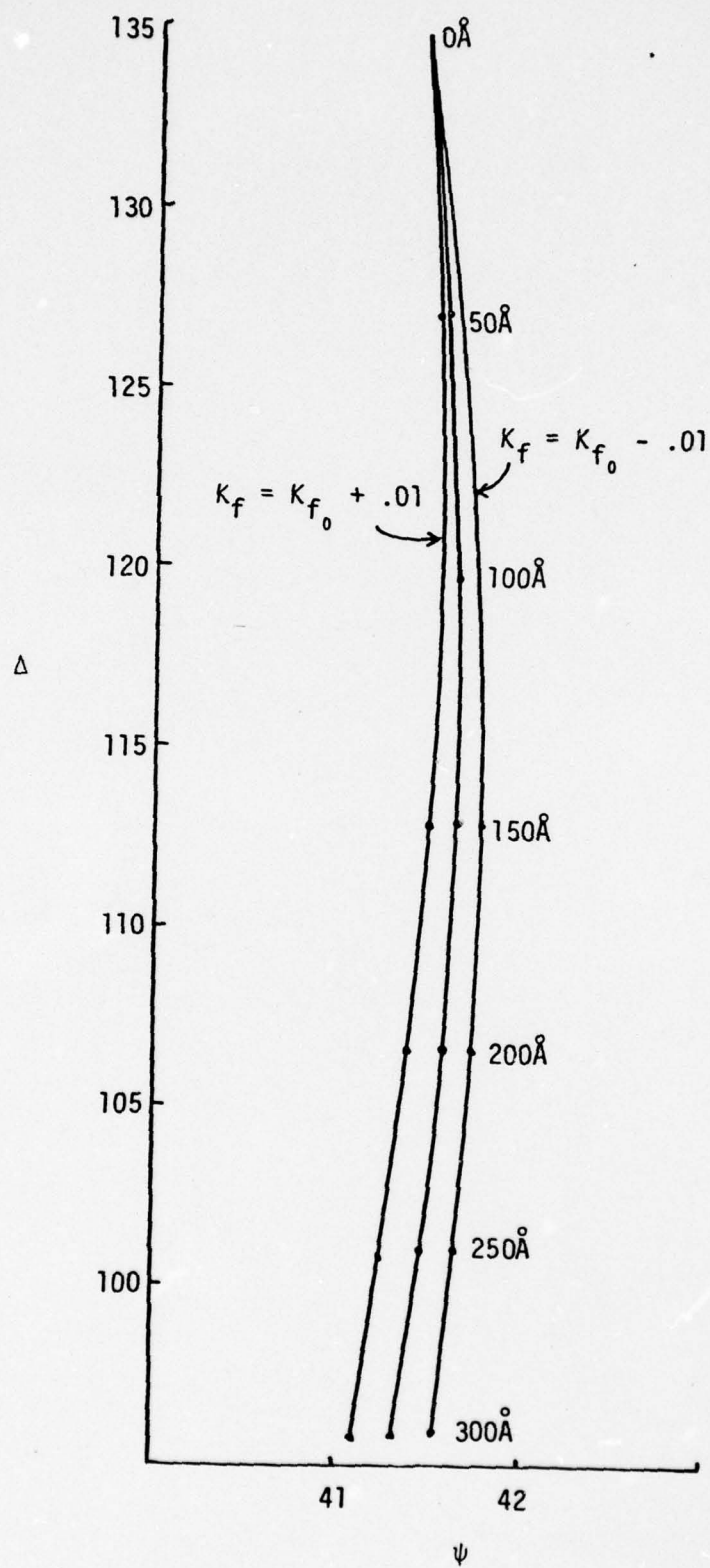


Fig. 5.18 Sensitivity of Theory Curve to Changes in K_f

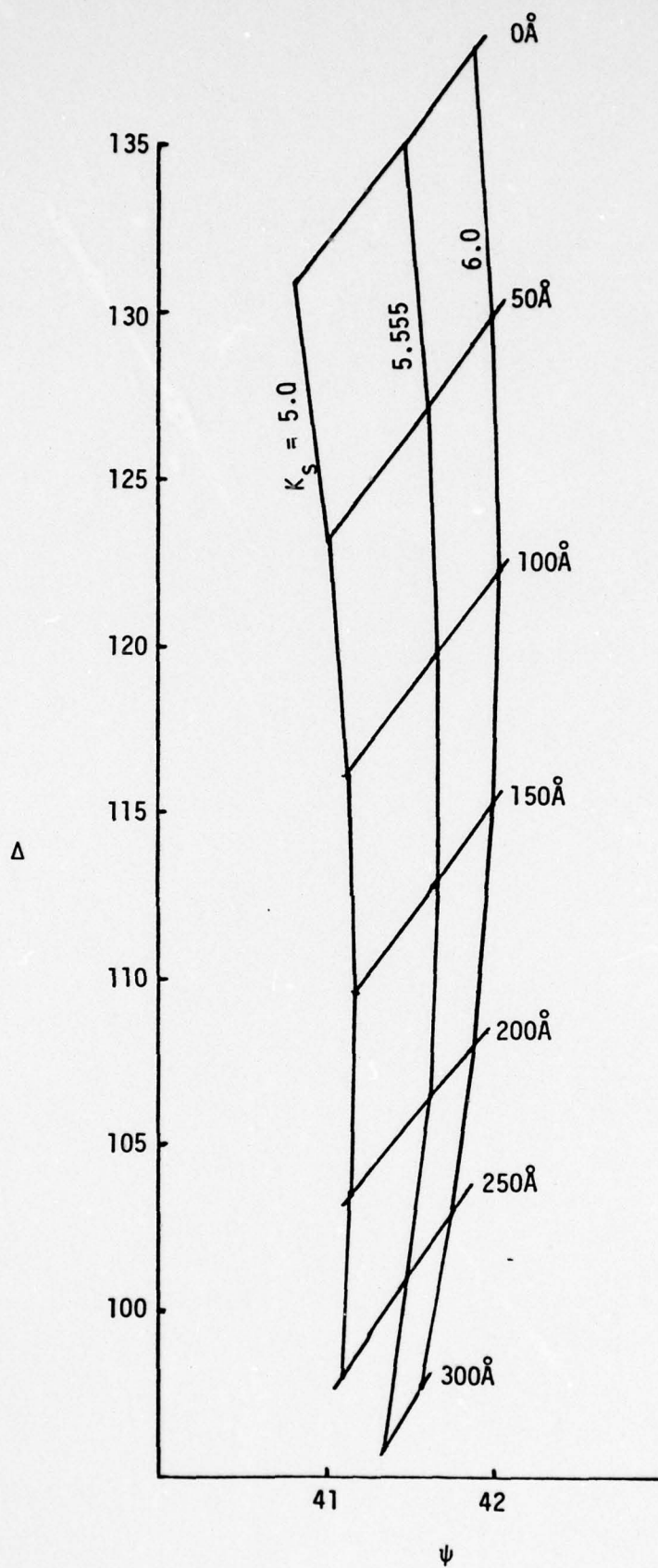


Fig. 5.19 Sensitivity of Theory Curve to Changes in K_s

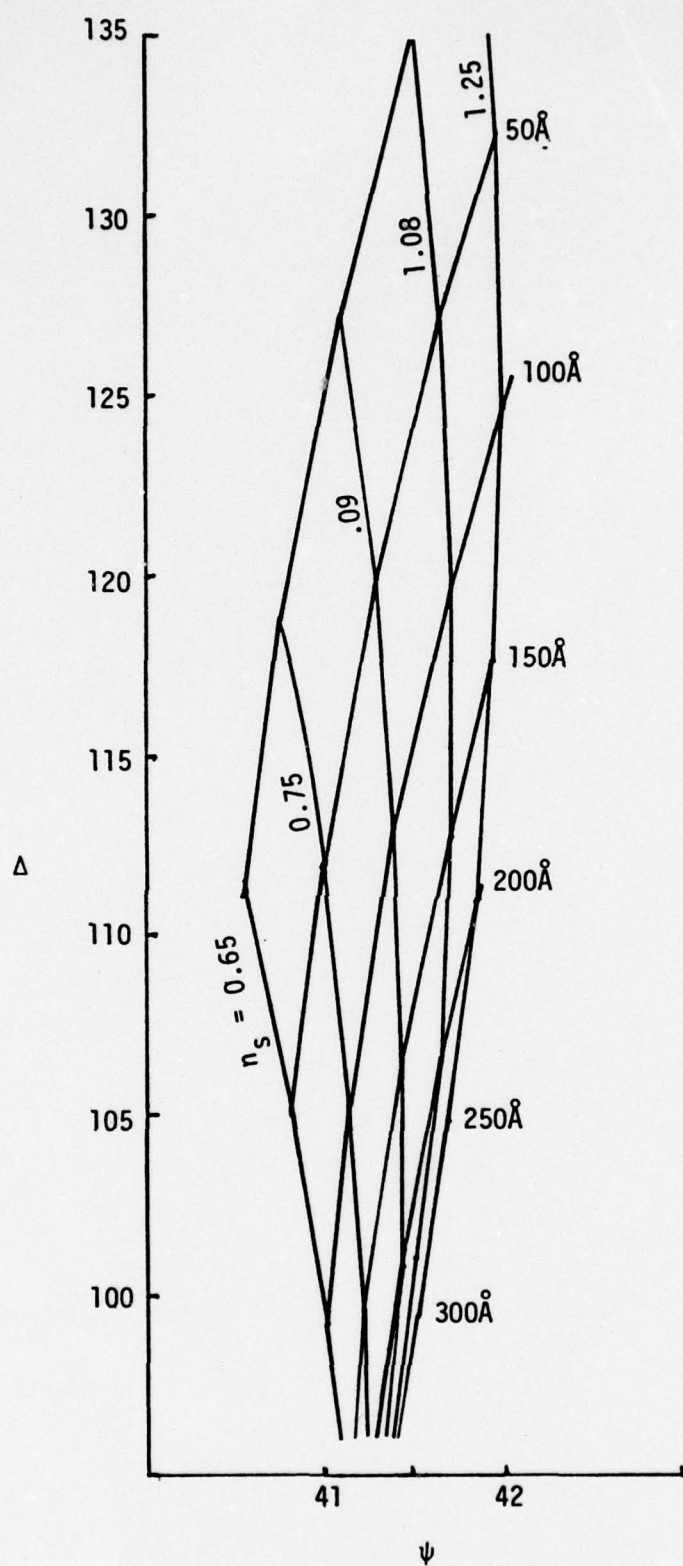


Fig. 5.20 Sensitivity of Theory Curve to Changes in n_s

to obtain the two additional curves.

In Fig. (5.19) the nominal value of 5.555 for K_s is varied to 6.0 and 5.0 for comparison. Fig. (5.20) shows four additional values for n_s along with the nominal value of 1.08. The parameter n_f is not illustrated here, because it was arbitrarily locked at 1.65 for the present study. Although Δ is slightly sensitive to n_f , the parameter n_f enters in such a way that the conclusions of this study are relatively insensitive to this parameter.

The sensitivity results illustrated in Figs. (5.18) to (5.20) may be summarized in terms of the partial derivatives of Δ , ψ , and t listed in Tables (5.2), (5.3), and (5.4). Variation of the incidence angle θ_i , about the nominal value of 70° , is illustrated in Fig. (5.21) by nominal media parameter curves of

$$\theta_i = 70^\circ \pm 0.2^\circ \quad .$$

Partial derivatives of Δ and ψ with respect to θ_i , evaluated from these results, are listed in Table (5.5). Corresponding partial derivatives of t with respect to θ_i may be obtained by combining results from Table (5.3) and Table (5.6):

$$\frac{\delta t}{\delta \theta_i} = \frac{\delta t}{\delta \psi} \frac{\delta \psi}{\delta \theta_i} + \frac{\delta t}{\delta \Delta} \frac{\delta \Delta}{\delta \theta_i} \quad .$$

To use the model shown in Fig. (5.15) a data point is projected in a perpendicular fashion to the closest point on the theory curve and the corresponding value of t is then obtained from the scale on the theory curve. In a sense, errors due to media parameters, alignment

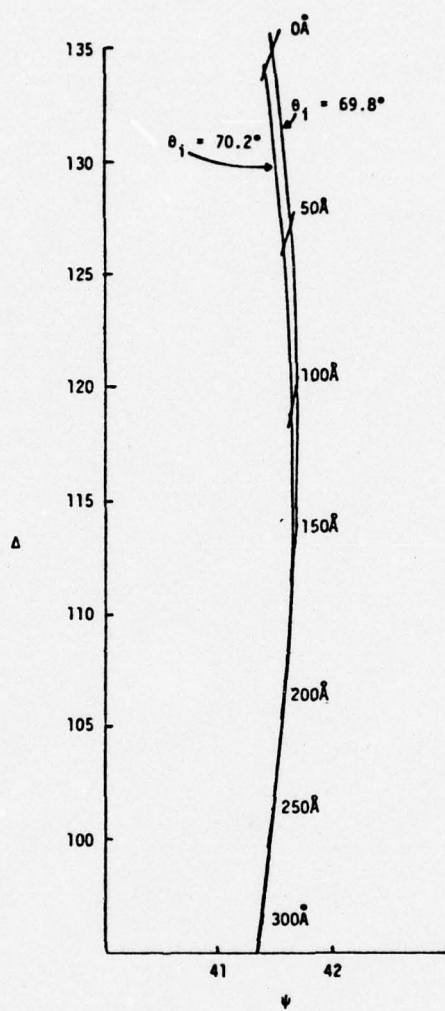


Fig. 5.21 Sensitivity of Theory Curve to Changes in θ_i

TABLE 5.3
SENSITIVITY OF THICKNESS TO Δ AND ψ

Range of t (\AA)	$\frac{\delta t}{\delta \psi} \left(\frac{\text{\AA}}{1^\circ} \right)$	$\frac{\delta t}{\delta \Delta} \left(\frac{\text{\AA}}{1^\circ} \right)$
0 - 50	3.02	6.35
50 - 100	1.43	6.78
100 - 150	0	7.27
150 - 200	1.96	7.84
200 - 250	5.55	8.89
250 - 300	6.83	9.76
300 - 350	9.72	11.11

TABLE 5.4
SENSITIVITY OF Δ TO K_s , n_s AND K_f

Value of t (Å)	$\frac{\delta\Delta}{\delta K_s}$	$\frac{\delta\Delta}{\delta n_s}$	$\frac{\delta\Delta}{\delta K_f}$	$\frac{\delta t}{\delta\Delta}$
0	6.84	37.32	0	6.35
50	6.48	35.34	.4	6.57
100	6.10	33.18	1.2	7.03
150	5.69	30.94	2.3	7.56
200	5.28	28.66	3.75	8.37
250	4.87	26.38	5.3	9.33
300	4.46		7.05	10.44
350	4.06		9.25	

TABLE 5.5
SENSITIVITY OF ψ TO K_s , n_s AND K_f

Value of t (Å)	$\frac{\delta\psi}{\delta K_s}$	$\frac{\delta\psi}{\delta n_s}$	$\frac{\delta\psi}{\delta K_f}$	$\frac{\delta}{\delta\psi}$
0	1.03	2.12	0	3.02
50	.95	1.90	5.05	2.23
100	.87	1.68	9.6	.715
150	.79	1.46	13.75	.98
200	.71	1.24	17.25	3.76
250	.64	1.02	20.2	6.19
300	.54		22.45	8.28
350	.45		24.0	

TABLE 5.6
SENSITIVITY OF THICKNESS TO θ_i

Value of $t(\text{\AA})$	$\frac{\delta\psi}{\delta\theta_i}$	$\frac{\delta\Delta}{\delta\theta_i}$
0	.15	2.47
50	.12	2.78
100	.10	3.03
150	.078	3.21
200	.055	3.34
250	.0375	3.42
300	.0175	3.47
350	.0025	3.49

errors, and the random errors arising in the taking of the data have already been incorporated into the model developed in Eqs. (5.1) to (5.3). Thus, it is not possible to untangle expected errors more accurately than the large and small error estimates made in Eqs. (5.5) and (5.4), respectively.

SECTION VI

A STUDY OF OXIDE FILMS ON ALCLAD ALLOY

Once the procedure for the ideal, pure aluminum surfaces, described in Section V, was developed, measurements were attempted for the more difficult case of alclad aluminum alloy. The intention was to attempt to develop a method for using ellipsometric measurements to characterize such rough surfaces. It is of considerable interest to determine the impact of surface roughness on the values of \tilde{n}_s and \tilde{n}_f as determined by ellipsometry and to attempt to determine the effective thickness of the oxide layer.

Alclad 2024, the best known and most widely used aircraft alloy, was used for the ellipsometric measurements. This alclad has a core of alloy 2024 with copper as the principal alloying element. The elements in this alloy are:

- .50% Silicon
- .5% Iron
- 3.8 - 4.9% Copper
- .30 - .9% Manganese
- .1% Chromium
- .25% Zinc
- .15% Titanium
- .15% Other
- remainder Aluminum

The core is covered on both sides with a cladding of alloy 1230. The minimum thickness of the cladding is 2% of the total thickness per side.

The cladding is composed of a minimum of 99.3% aluminum with other elements being

- .7% Silicon and Iron
- .10% Copper
- .05% Manganese
- .1% Zinc
- .05% Other elements

The thickness of the alclad used was approximately .04 inches. The alclad is solution heat-treated at 493°C and then worked cold to improve strength.

As had been done with the pure aluminum samples, it was decided to heat the alclad samples over and over, determining the parameters ψ and Δ after each heating. In this way a data trajectory can be established on a ψ , Δ plot and selection of effective parameters to fit the data can be attempted. The melting range of alclad is between 502° and 638°C so that a heating temperature of 350°C was again selected. After initial warmup, the samples were held at 350°C for two hours and then allowed to cool.

On the first sample, Sample 1, four spots, a, b, c, and d, were marked. The measurements for ψ and Δ were made at these points, then the sample was heated four times with measurements made after each heating. Data points for spots a, b, c, and d are given subscripts 0, 1, 2, 3, 4, denoting the number of times the sample had been heated before the measurement. After the first heating, the measured value for Δ increased for three of the points. Further heating did decrease

the measured Δ as expected from experience with the optically flat aluminum samples. As shown in Fig. (6.1) the data from the measurements are scattered over a much wider range than was found for aluminum samples in the previous section, although, as the samples are heated more times, they tend to develop parallel trajectories of successively decreasing Δ .

Careful examination of the alclad shows very shallow grooves in the surface: rolling grain marks left from the rollers used in manufacturing. Measurements made with these lines vertical, designated as a 90° sample angle, result in the light shining across these grooves and the surface, perhaps, appears to the light to be rougher. Measurements made with these grooves horizontal, designated as 0° sample angle, effectively appear to be a smoother surface. In a sense, the grooves generate a family of parallel smoother surfaces. Measurements were taken from two different samples to find if, indeed, the sample angle has any effect on the values of ψ and Δ . The measurements from Sample 2, Fig. (6.2) were taken at two spots, a and b. Measurements at each spot were taken at both 0° and 90° sample angles before heating and after three successive heatings. Again, subscripts are used to indicate the number of heating cycles. The data for the smoother surface, 0° sample angle, has larger values of ψ , although the trajectory for a given point on the sample follows a similar path for both the 0° and 90° angles.

Measurements from a third piece of alclad, Sample 3, gave results similar to those for Sample 2. These data are shown in Fig. (6.3). A

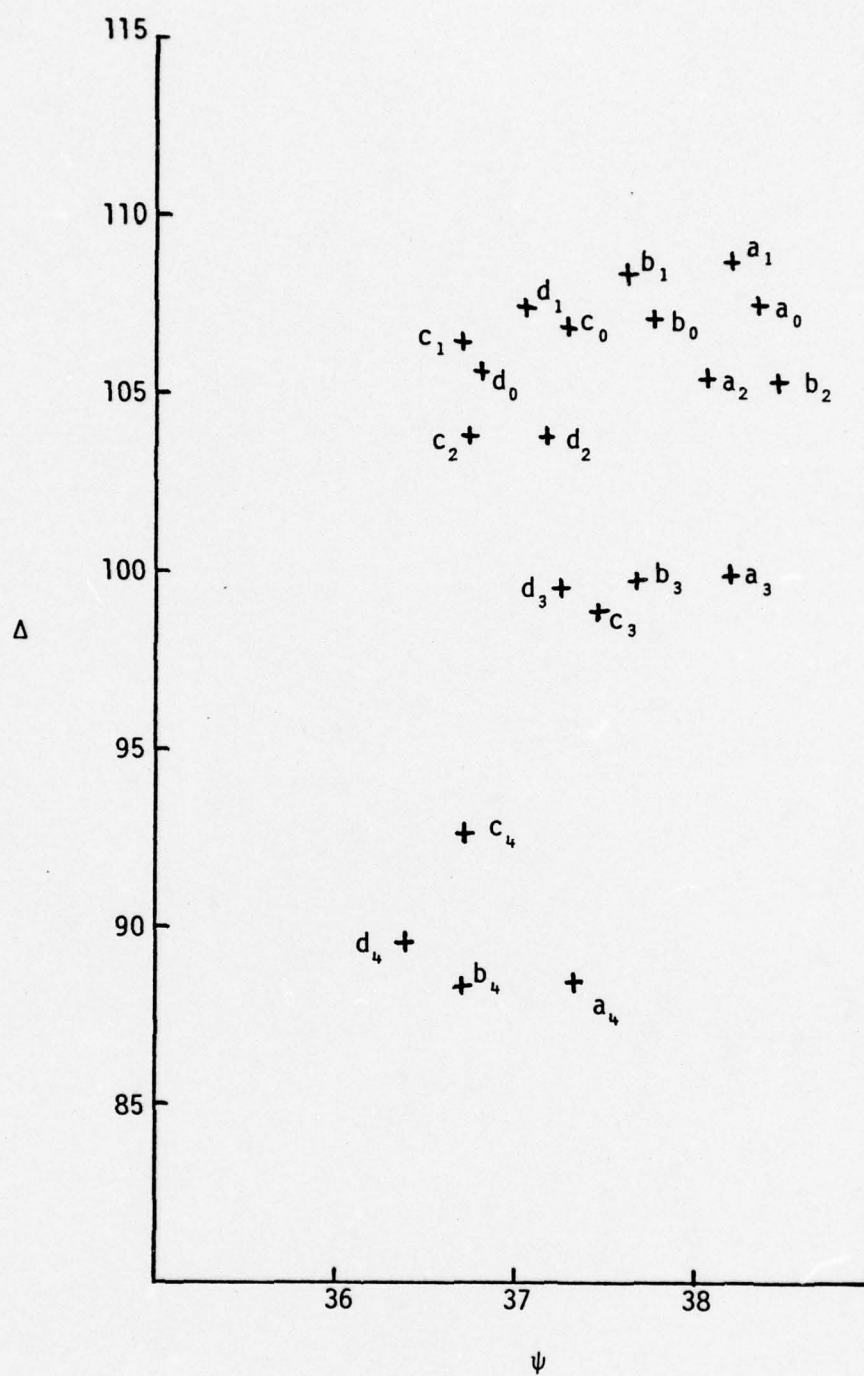


Fig. 6.1 Data from Alclad Sample 1

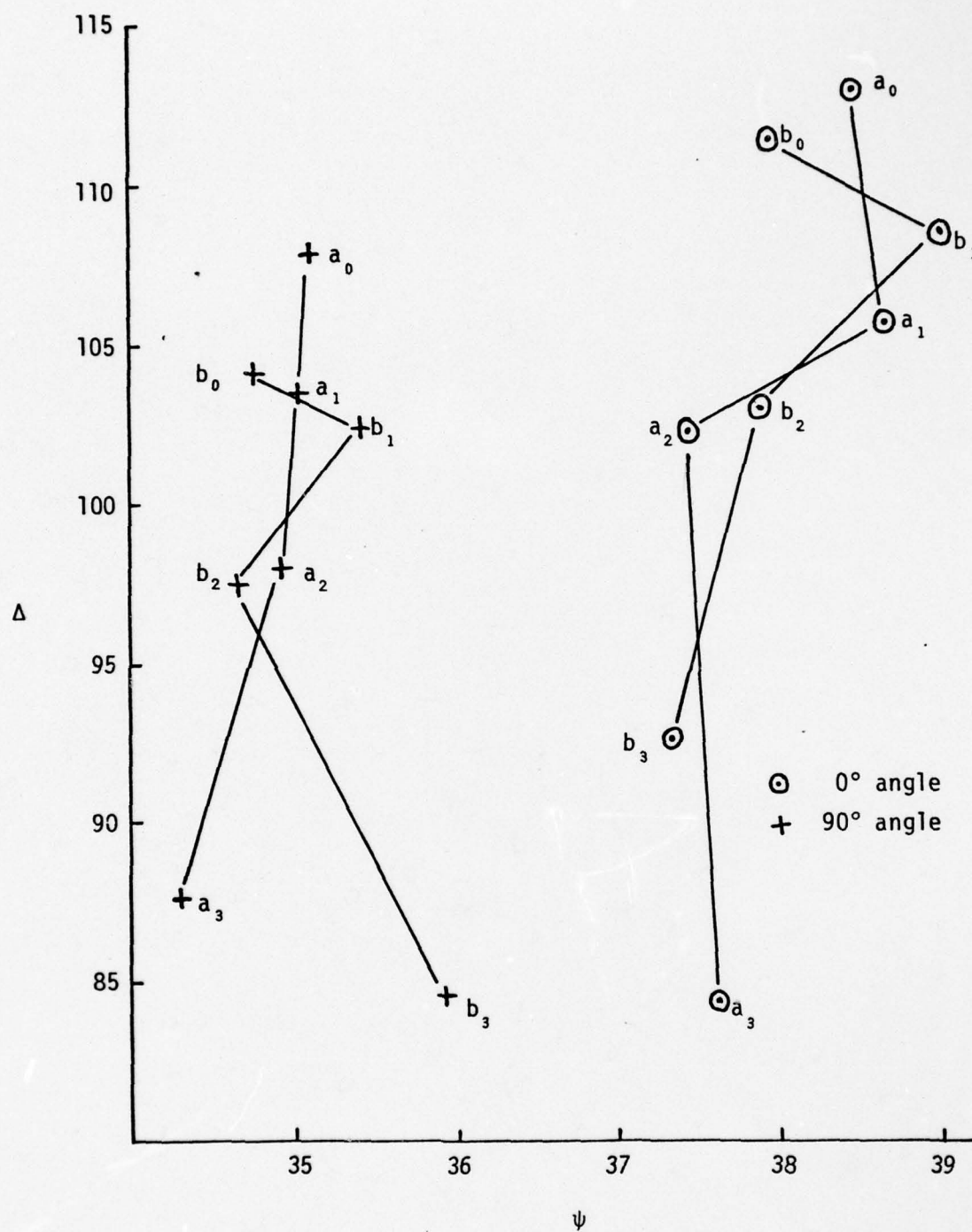


Fig. 6.2 Data from Alclad Sample 2 Taken at Sample Angles of Both 0° and 90° with Trajectories of Increasing Thickness

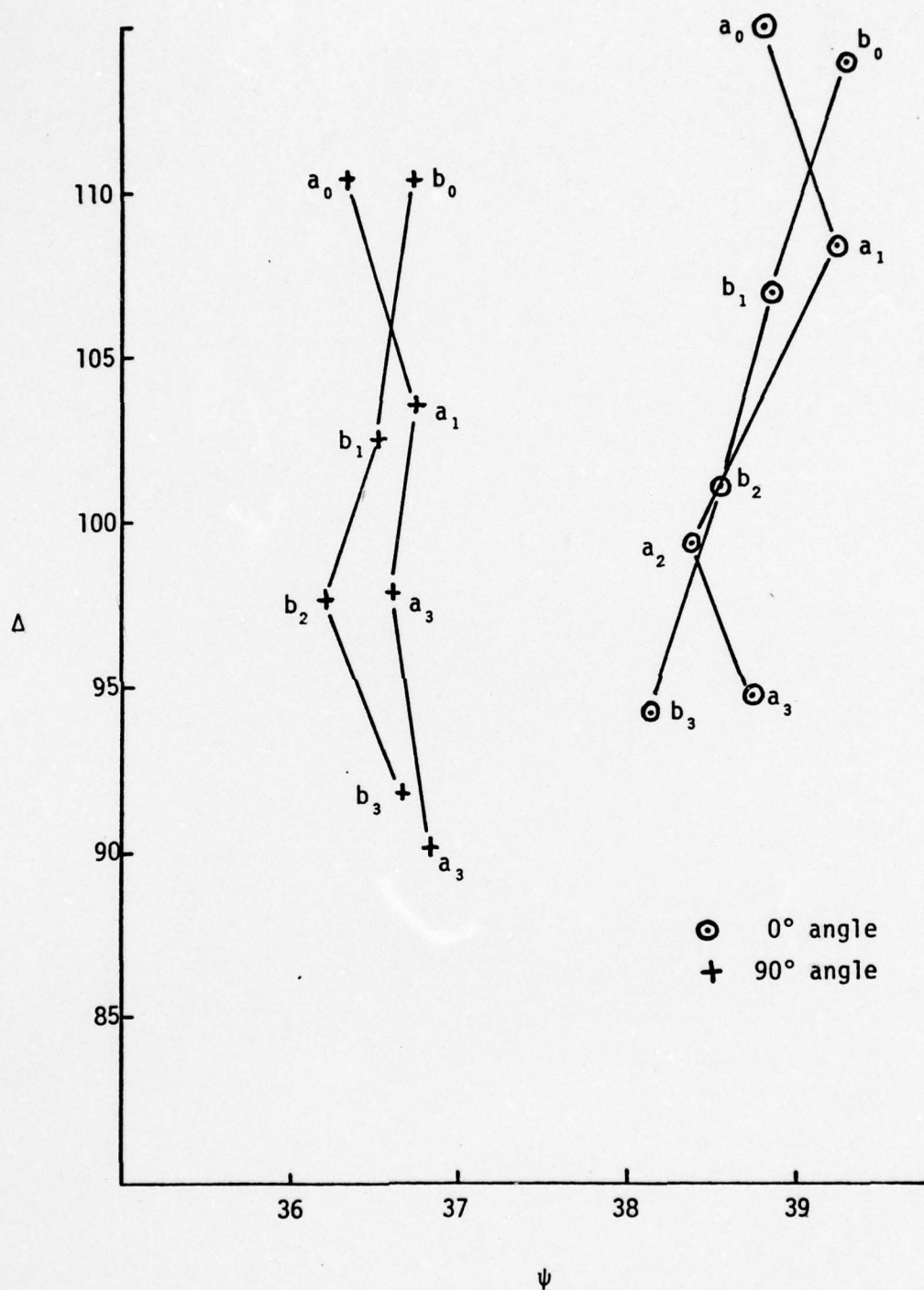


Fig. 6.3 Data from Alclad Sample 3 Taken at Sample Angles of both 0° and 90° with Trajectories of Increasing Thickness

shift of both the 90° sample angle trajectory and the 0° sample angle trajectory to the right (larger values of ψ) for Sample 3 with respect to Sample 2 can be observed by comparing Figs. (6.2) and (6.3). From the work of Section V, the shift to larger ψ is known to be correlated with a smaller effective roughness. As a matter of fact, the surface of Sample 3 looked smoother and shinier than the surface of Sample 2.

At a single point on a sample the thickness is obviously the same whether measured at a sample angle of 0° or at a sample angle of 90° . Using the measurements taken at angles of 0 and 90° for each point on the two samples, lines of constant thickness can be drawn. The results are shown in Figs. (6.4) and (6.5). Using the trajectories formed from the data taken after consecutive heatings, shown in Figs. (6.2) and (6.3), and the lines of constant thickness, from Figs. (6.4) and (6.5), an attempt was made to fit a theory curve to the measured data.

The first attempts in fitting a curve to the alclad data involved the variation of only one parameter from the set used for the optically flat samples of aluminum. The first parameter varied was n_s while $K_s = 5.555$, $n_f = 1.65$ and $K_f = (.01)\frac{t}{50}$ were kept fixed. The value of n_s was varied from 0.6 to 1.08 and the curves of constant thickness for this variation of n_s are shown in Fig. (6.6). Also shown in Fig. (6.6) are data measured at spot a of alclad Sample 3. Comparison of the calculated curves with the measured data from Sample 3 shows that the slope of the calculated constant thickness lines are much steeper than the constant thickness lines for the measured data.

Next, the parameter K_s was varied while n_s was returned to 1.08.

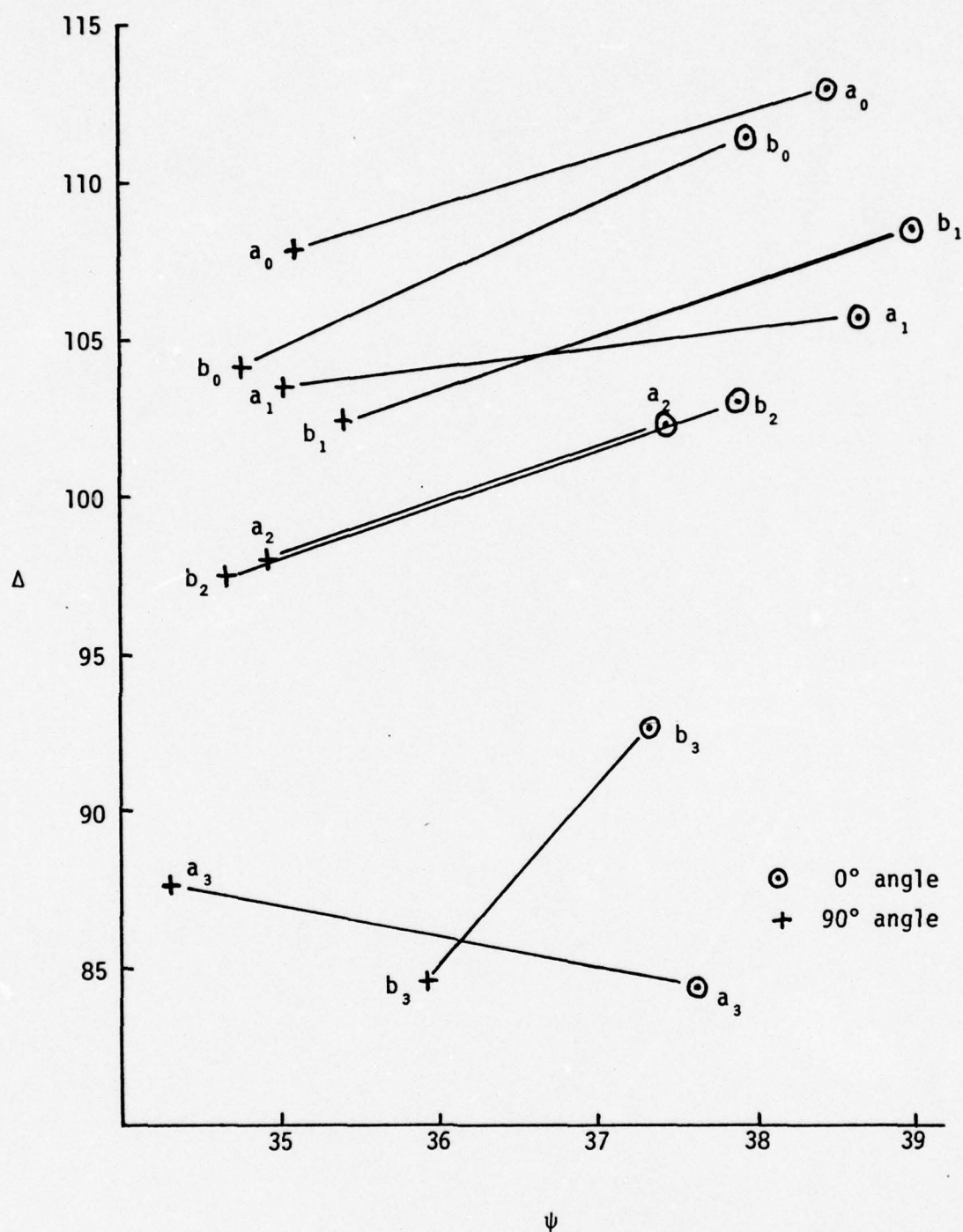


Fig. 6.4 Data from Alclad Sample 2 with Lines of Constant Thickness

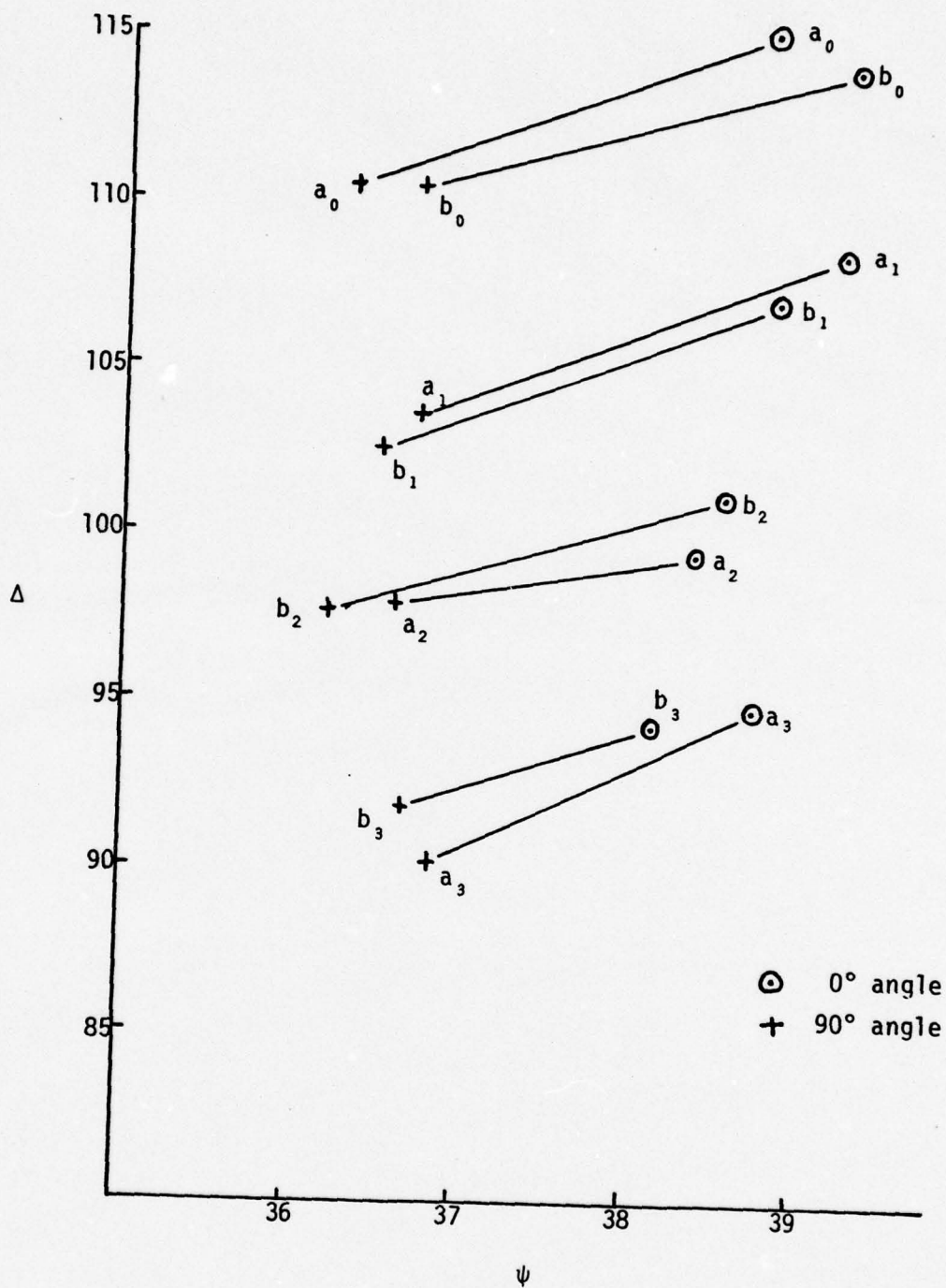


Fig. 6.5 Data from Alclad Sample 3 with Lines of Constant Thickness

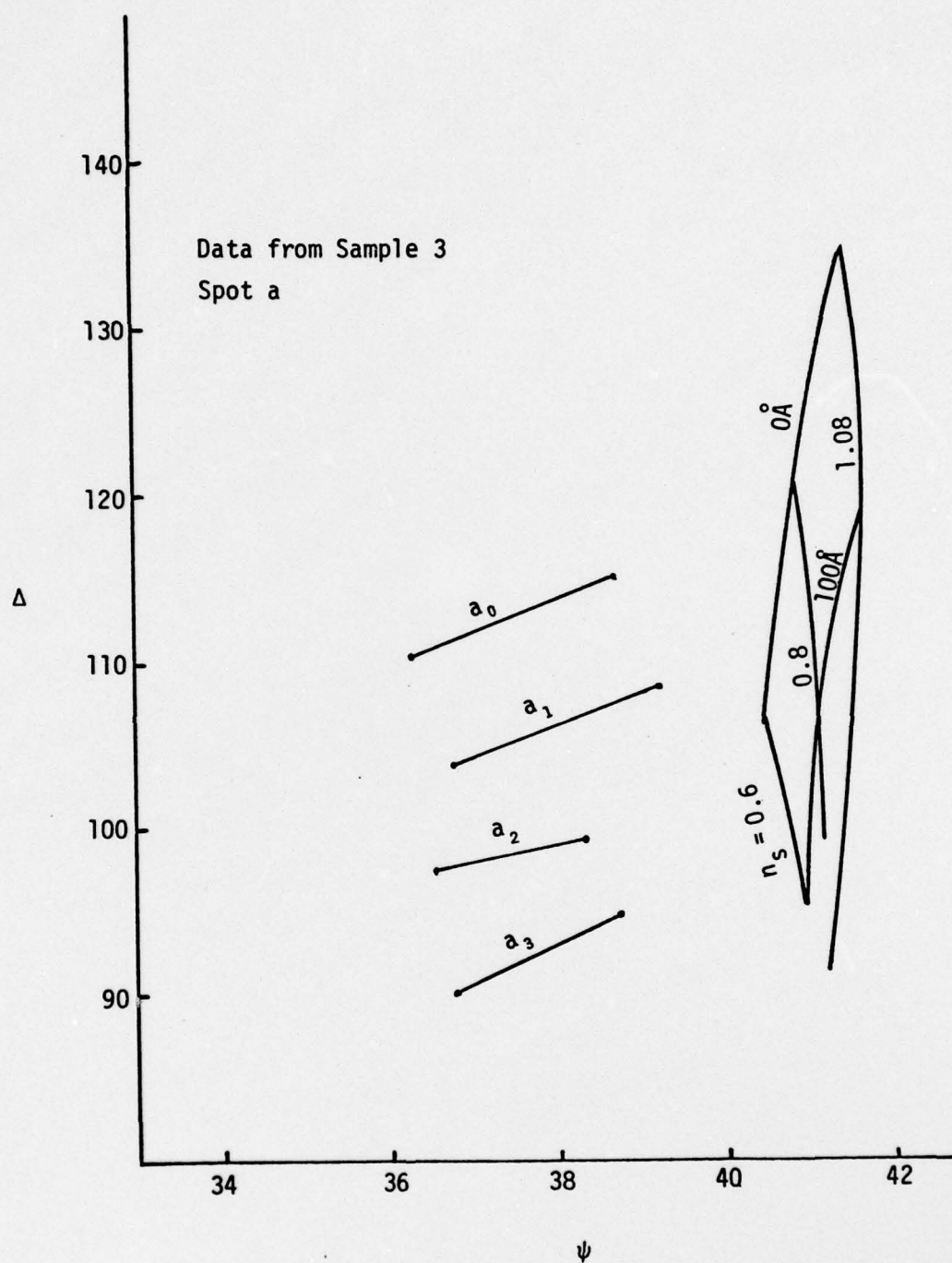


Fig. 6.6 Lines of Constant Thickness Derived from Variations in n_s Compared with Data from Sample 3 Spot a

The range for which K_s varied was from 1.45 to 1.60. The curves produced from this variation are shown in Fig. (6.7) along with the data from spot a of Sample 3. Comparison with the data of the constant thickness lines produced from variations of K_s shows that these theoretical curves are also too steep to fit the data.

A combination using both K_s and n_s was then tried. By judging the behavior of the curves in Figs. (6.6) and (6.7) and by experimenting with the parameter dependence of the curves, the following model was devised:

$$K_s = 9.75 - 4.77n_s + 0.505n_s^2 \quad . \quad (6.1)$$

Curves based upon this relationship are shown in Fig. (6.8). Again comparison can be made to the data taken from spot a of Sample 3. The slope of the constant thickness lines for the theory curves and the data do agree, but the trajectories of increasing oxide thickness do not follow the lines of constant n_s .

In Section V, a change in K_f was used to correct for variation between the theory and the data. The change was made to correct for surface roughness and K_f was varied as a function of thickness:

$$K_f = (0.01)\frac{t}{50} \quad . \quad (6.2)$$

This same form of K_f as a function of t was used for the curves in Fig. (6.8).

It might be assumed that the roughness of the oxide layer growth responds to increases in the substrate roughness. A way, therefore,

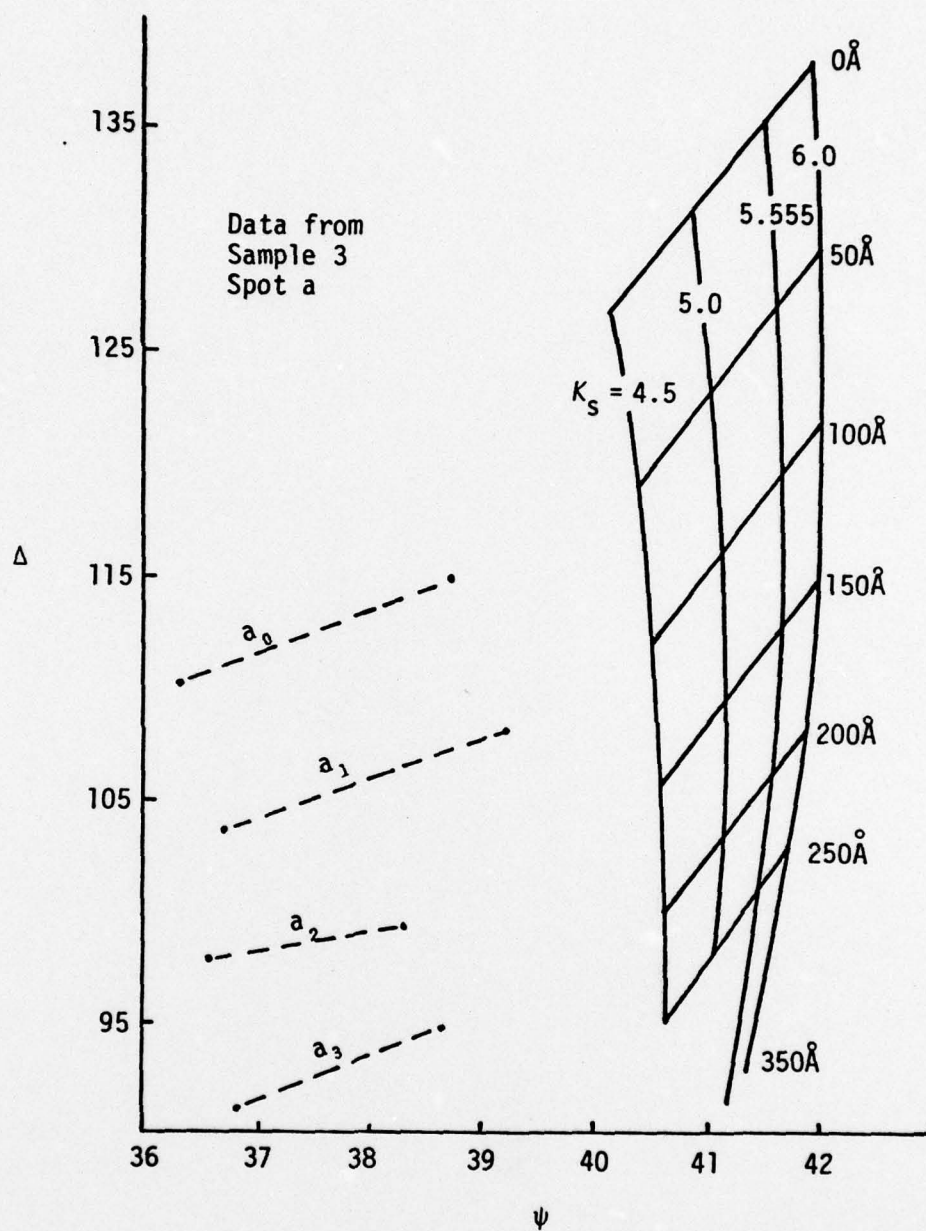


Fig. 6.7 Lines of Constant Thickness Derived from Variations in K_s Compared with Data from Sample 3, Spot a

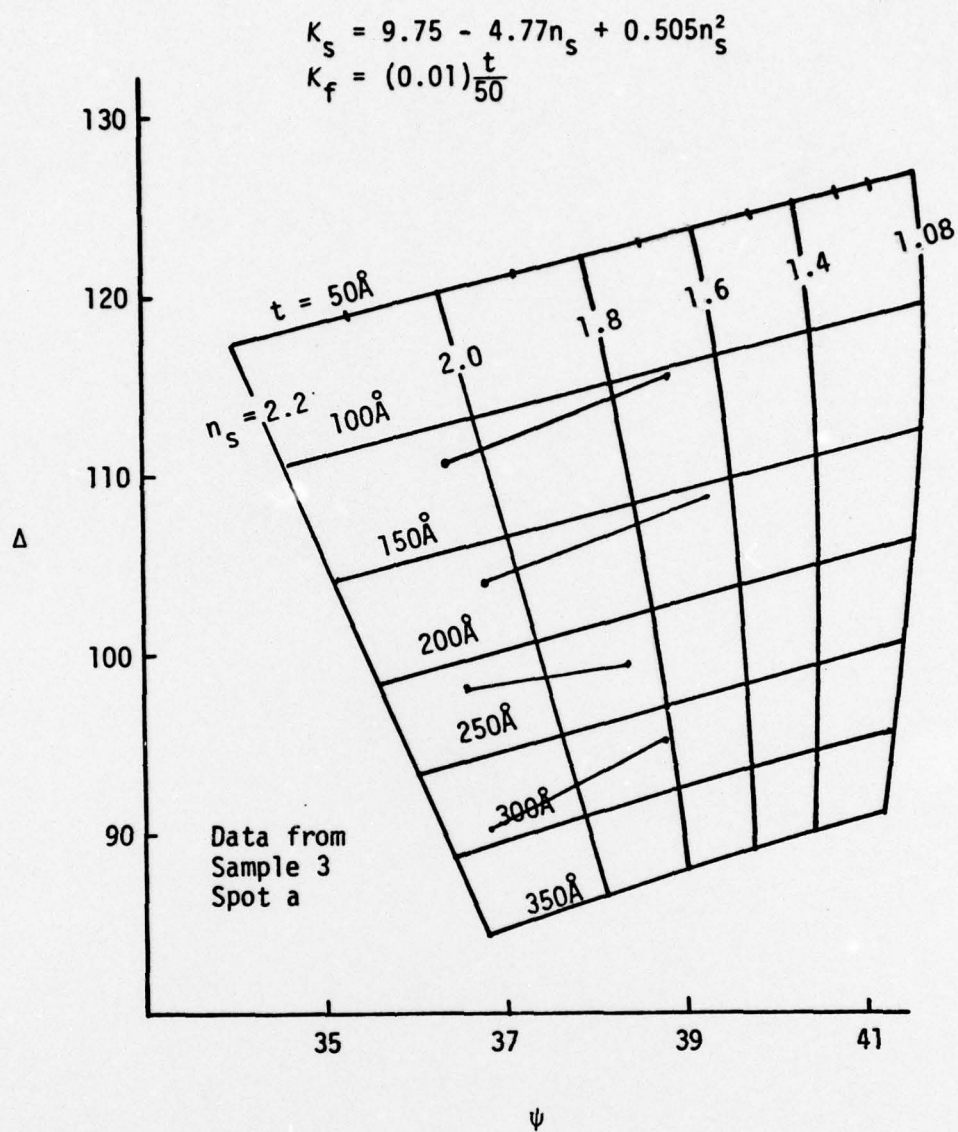


Fig. 6.8 Lines of Constant Thickness Derived from Variations of Both n_s and K_s Compared to Data from Sample 3 Spot a

to improve the curve fit might be to increase K_f in response, not only to t , but, also, in response to substrate roughness as measured by K_s . However, since Eq. (6.1) models K_s as a function of n_s , it is equivalent to assign K_f a dependence on n_s as well as t . In this spirit, the following model was tried:

$$K_f = (0.01) \frac{t}{50} n_s \quad . \quad (6.3)$$

The curves displayed in Fig. (6.9) correspond to the same case shown in Fig. (6.8) except that Eq. (6.3) is used to describe K_f . The data from both spots on Sample 3 are shown for comparison. The data measured from Sample 2 are shown with the same theory curves in Fig. (6.10). The curves shown in Figs. (6.9) and (6.10) are obtained by letting n_s vary from 1.08 to 2.2 while K_s and K_f vary as functions of n_s according to Eqs. (6.1) and (6.3). Fig. (6.11) shows the functions K_s and K_f defined by Eqs. (6.1) and (6.3).

Again reference is made to the work of Fenstermaker and McCracken[9] showing the theoretical change of n_s and K_s as a surface of gold or silver increases in roughness. Their results, reproduced in Fig. (6.12) shows an increase in n_s and a decrease in K_s as the surface roughness increased. As evidenced in Fig. (6.11), this is the type and direction of the variations used in fitting the present data of alclad.

Now that a model for the parameter behavior for oxide films on alclad has been selected to fit the data trajectories, certain observations can be made. First, it does appear that the thickness of oxide layers on aluminum can be measured with ellipsometry, provided that

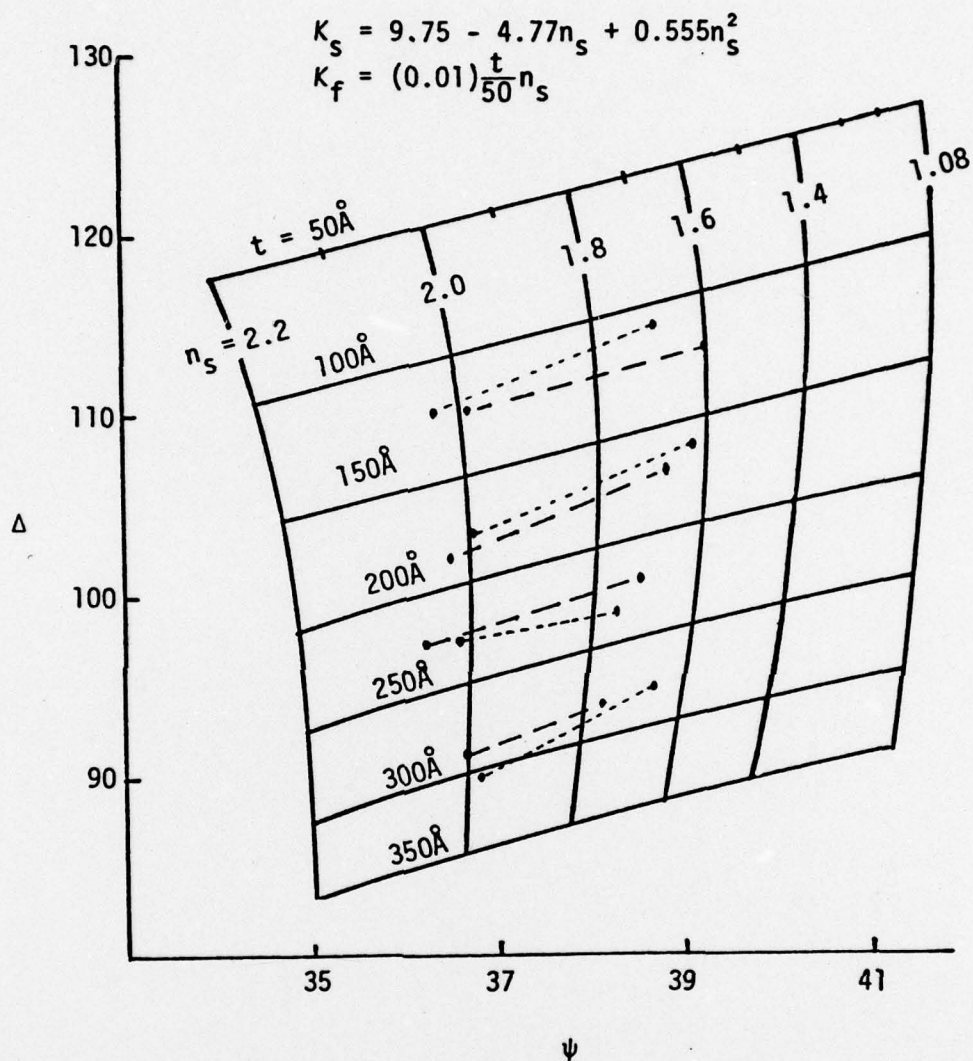


Fig. 6.9 Lines of Constant Thickness Derived from Variations in n_s where K_s and K_f are Functions of n_s Compared with Data from Sample 3

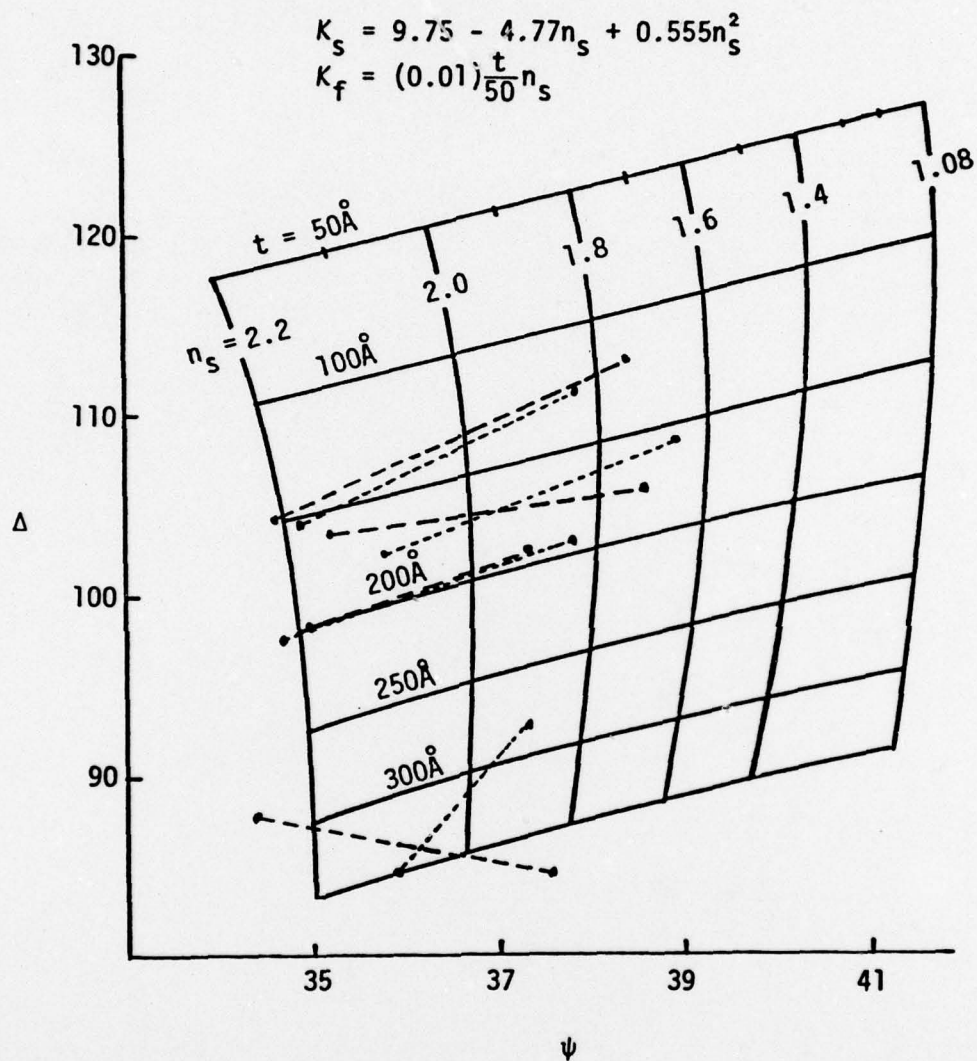


Fig. 6.10 Lines of Constant Thickness Derived from Variations in n_s where K_s and K_f are Functions of n_s Compared with Data from Sample 2

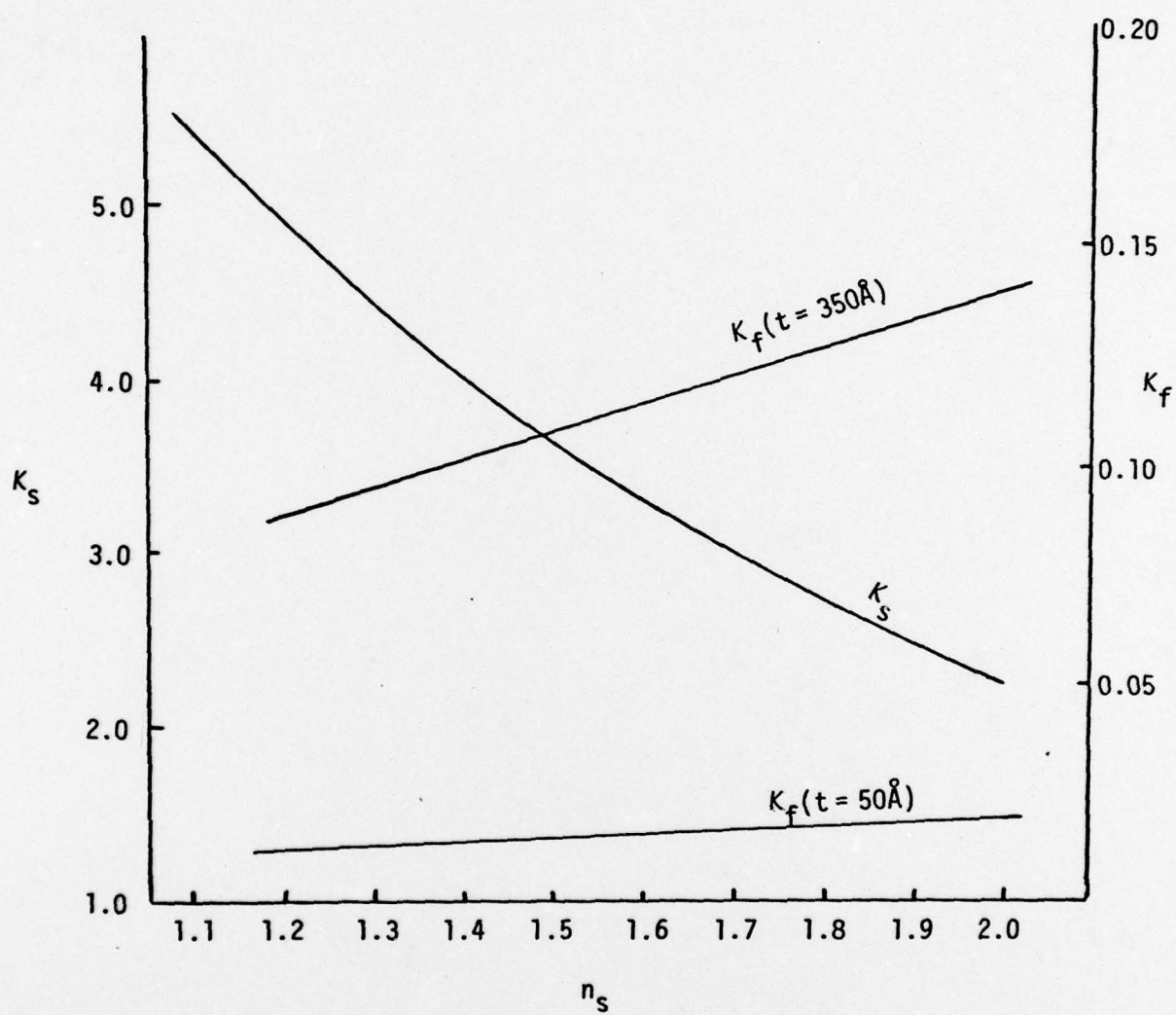


Fig. 6.11 Comparison of K_s and K_f with n_s

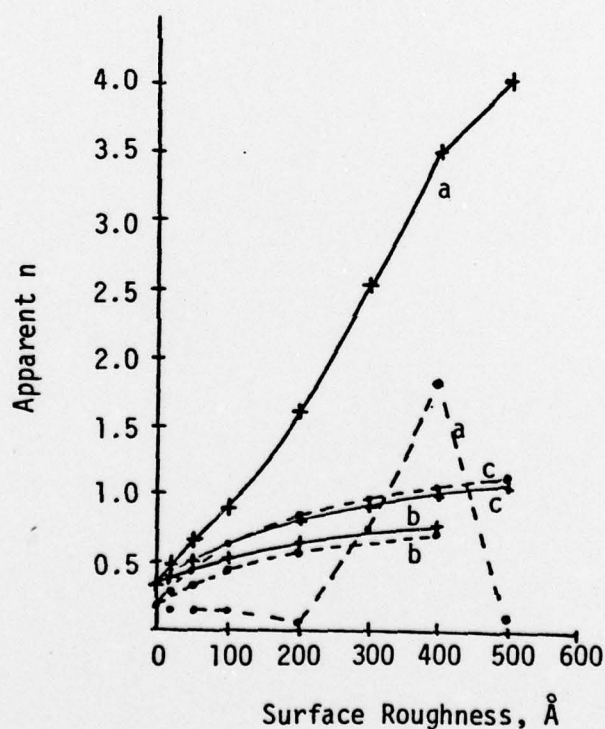
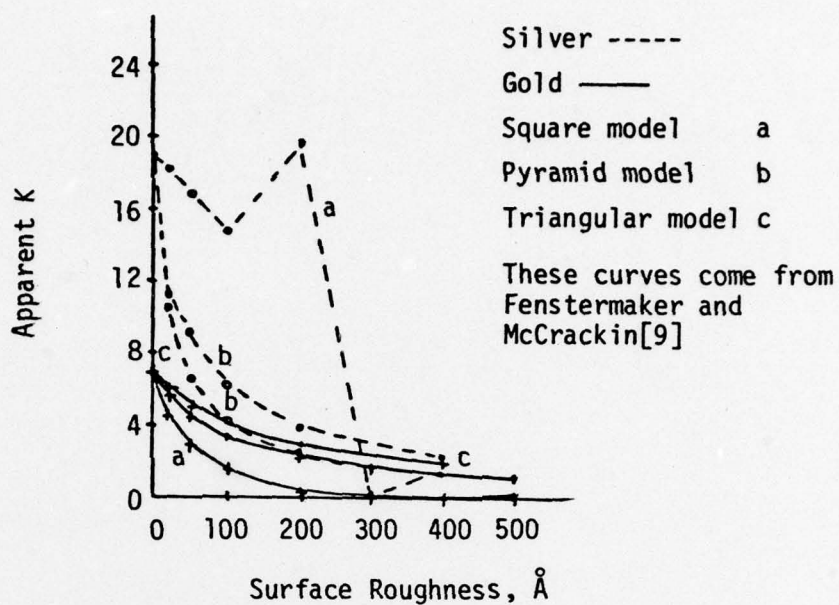


Fig. 6.12 Apparent Values of n and K for Rough Surfaces Derived using Triangular, Square and Pyramid Models

attention is given to the sample angle. As is evident in Fig. (6.9), for Sample 2 the effective n_s for a 90° sample angle differs from the effective n_s for a 0° sample angle by about 0.4. A similar difference is found for Sample 3 in Fig. (6.10). One notices a larger average value of n_s for Sample 2, the one appearing rougher to the eye.

As originally anticipated, the sample angle of 90° is shown, by Figs. (6.9) and (6.10), to correspond to a greater roughness assignment (larger value of n_s) than the sample angle of 0° . This conclusion was tested at intermediate sample angles for both Samples 2 and 3. The results, shown in Fig. (6.13), indicate that one can almost use the ellipsometrically determined value of n_s to detect the sample orientation angle, if the average value of n_s is known for the sample.

The results in Fig. (6.13) were taken after Samples 2 and 3 had been heated three times for a total of six hours. The same effect was examined on a fresh, unheated, sample of alclad and the results are shown for two points on the sample in Fig. (6.14).

In conclusion, it appears that the method employed in this study, using data trajectories obtained by repeatedly heating samples to deduce parameter interrelationships, shows great promise for ellipsometric work for rough films on both smooth and rough substrates. The measurements do indicate that index parameters change in an orderly way that can be predicted as functions of thickness and surface roughness. Additional work will be required to test the specific parameter relationships found in this work.

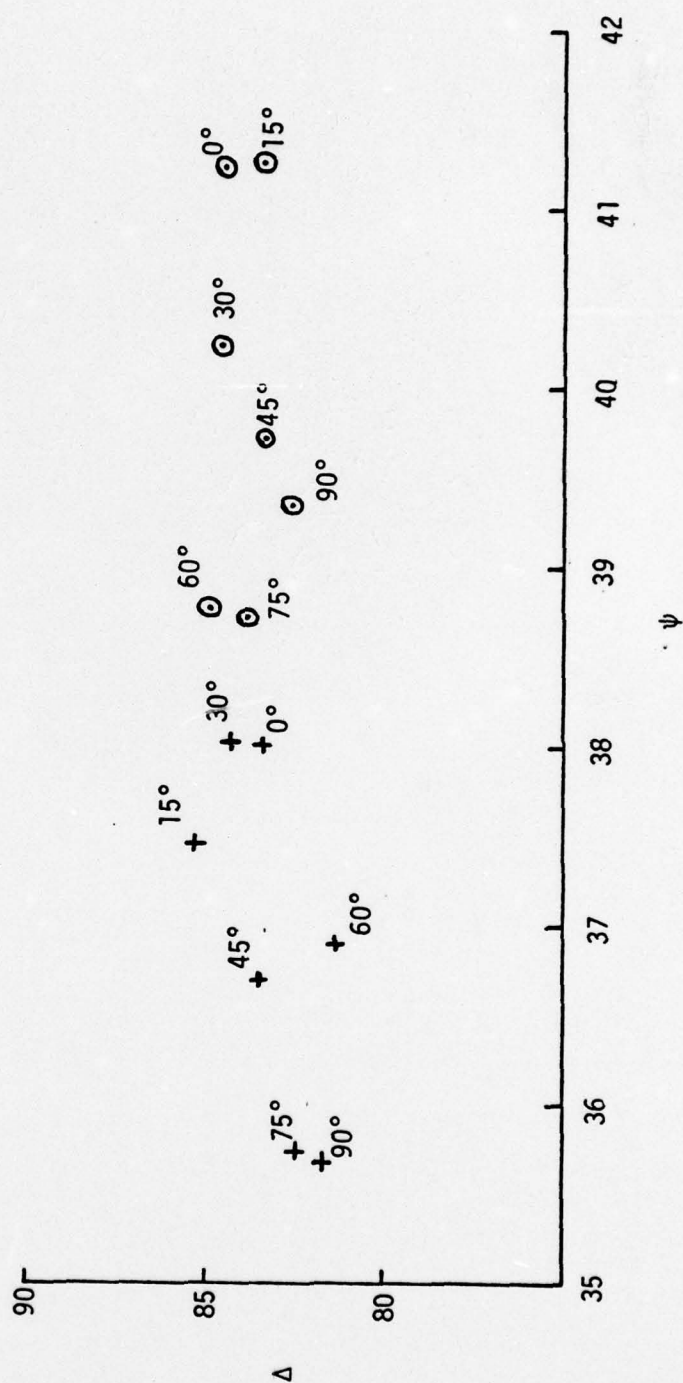


Fig. 6.13 The Changes in Samples 2 and 3 Due to Changes in the Sample Angle

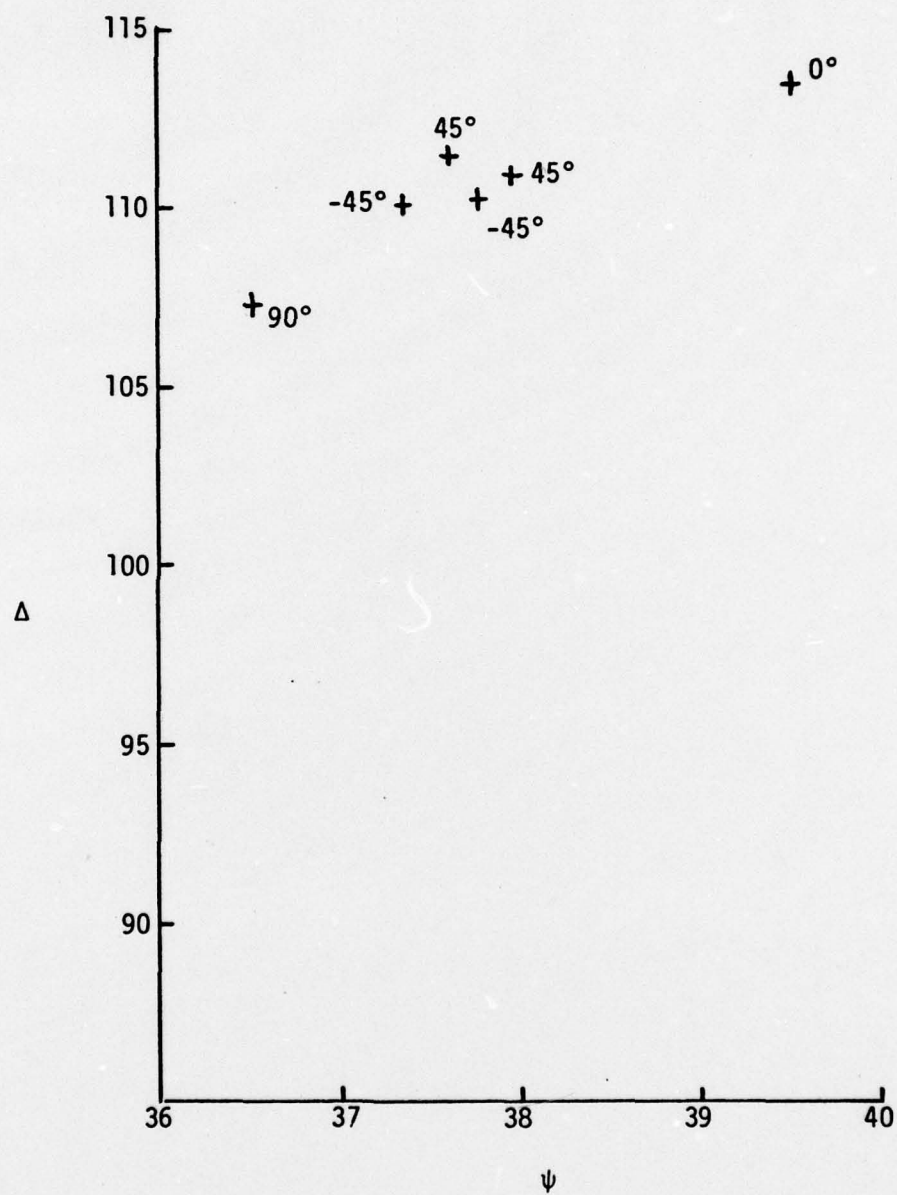


Fig. 6.14 Data from Sample 4 at Various Sample Angles

LIST OF REFERENCES

1. Lydon, Malcolm W. "Ellipsometric Techniques for Determining Oxide Layer Thickness on Aluminum." Masters Thesis, Texas Tech University, May 1, 1975.
2. Jenkins, F. A., and White, Harvey E. Fundamentals of Optics. New York: McGraw-Hill, 1957.
3. Zaininger, K. H., and Revesz, A. G. "Ellipsometry - A Valuable Tool in Surface Research." RCA Review, March 1964, pp. 85-111.
4. Born, M., and Wolf, E. Principles of Optics. New York: Pergamon Press, 1965, pp. 613-618.
5. McCrackin, Frank L. A Fortran Program for Analysis of Ellipsometer Measurements, Technical Note 479 National Bureau of Standards, U. S. Government Printing Office, April 1969.
6. Fane, R. W., Neal, W. E. J. "Optical Constants of Aluminum Films Related to the Vacuum Environment." Journal of the Optical Society of America, Vol. 60, No. 6, June 1970, pp. 790-793.
7. Halford, J. H., Chin, F. K., Norman, J. E. "Effects of Vacuum Deposition Conditions on Ellipsometric Parameters, Optical Constants, and Reflectance of Ultrapure Aluminum Films." Journal of the Optical Society of America, Vol. 63, No. 7, July 1973, pp. 786-792.
8. Dignam, M. J. "Oxide Films of Aluminum, Kinetics of Formation in Oxygen." Journal of the Electrochemical Society, Vol. 109, No. 3, March 1962, pp. 192-198.
9. Fenstermaker, Carl A., McCrackin, Frank L. "Errors Arising from Surface Roughness in Ellipsometric Measurement of the Refractive Index of a Surface." Surface Science, 16, 1969, pp. 85-96.
10. Nyce, A. C., Skolnick, L. P. "Optical Constants of Bulk and Thin-film Aluminum at 6328Å." Journal of the Optical Society of America, Vol. 65, No. 7, July 1975, pp. 792-795.
11. Wolf, E. "Optical Constants of Absorbing Thin Films." Progress in Optics, Vol. IV, pp. 172-173.

BIBLIOGRAPHY

- Archer, R. J. "Determination of the Properties of Films on Silicon by the Method of Ellipsometry." Journal of the Optical Society of America, 52, No. 9 (1962), 970-974.
- Archer, R. J. Manual on Ellipsometry. Chicago: Gaertner Scientific Corporation, 1966.
- Born, M., and E. Wolf. Principles of Optics. Elmsford, N.Y.: Pergamon Press, 1959.
- Brusic, V., M. A. Genshaw, and J. Bockris. "On the Possible Influence of Surface Roughening on Ellipsometric Data in Electrochemical Studies." Surface Science, 29 (1972), 653-662.
- Corson, D., and P. Lorrain. Introduction to Electromagnetic Fields and Waves. San Francisco: W. H. Freeman and Company, 1962.
- Drude, P., and Weid. "Bestimmung der Optischen Konstanten der Metalle." Annalen der Physik, 39, No. 481 (1890).
- Fane, R. W., and W. E. J. Neal. "Optical Constants of Aluminum Films Related to the Vacuum Environment." Journal of the Optical Society of America, 60, No. 6 (1970), 790-793.
- Fenstermaker, Carl A., and Frank L. McCrackin. "Errors Arising from Surface Roughness in Ellipsometric Measurement of the Refractive Index of a Surface." Surface Science, 16 (1969), 85-96.
- Ghezze, Mario. "Thickness Calculations for a Transparent Film from Ellipsometric Measurements." Journal of the Optical Society of America, 58, No. 3 (1968), 368-372.
- Halford, J. H., and F. K. Chin. "Effects of Vacuum Deposition Conditions on Ellipsometric Parameters, Optical Constants and Reflectance of Ultrapure Aluminum Films." Journal of the Optical Society of America, 63, No. 7 (1973), 786-792.
- Holmes, D. A., and D. L. Frucht. "Formulas for Using Wave Plates in Ellipsometry." Journal of the Optical Society of America, 57, No. 4 (1967), 446-472.
- Lewis, Winifred. Thin Films and Surfaces. Brooklyn, N.Y.: Chemical Publishing Company, Inc., 1950.

- McCrackin, Frank L., and J. P. Colson. Ellipsometry in the Measurement of Surfaces and Thin Films. National Bureau of Standards Miscellaneous Publication 256. Washington, D.C.: U. S. Government Printing Office, 1961.
- McCrackin, Frank L., Elio Passaglia, Robert R. Stromberg, and Harold Steinberg. "Measurement of the Thickness and Refractive Index of Very Thin Films and the Optical Properties of Surfaces by Ellipsometry." Journal of Research of the National Bureau of Standards - A. Physics and Chemistry, 67A, No. 4 (1963), 363-377.
- McCrackin, Frank L. Technical Note 479. National Bureau of Standards Washington, D.C.: U. S. Government Printing Office, April, 1969.
- Neal, W. E. J., R. W. Fane, and N. W. Grimes, "The Correlation of Structural with Optical Measurements on Thin Aluminum Films Evaporated in Ultra High Vacuum." The Philosophical Magazine, 21, No. 169 (1970), 167-175.
- Vedam, K., and Samuel S. So. "Characterizations of Real Surfaces by Ellipsometry." Surface Science, 29 (1972), 379-395.
- Weid. "Über Oberflächenschichten, I and II." Annalen der Physik, 30, No. 532 (1899), 865.
- Winterbottom, A. B., "Optical Methods of Studying Films on Reflecting Bases Depending on Polarization and Interference Phenomena." Transactions of the Faraday Society, 42 (1946), 487-495.